HARMONIC SUPPRESSED RECONFIGURABLE DUAL-BAND, MULTI-MODE ULTRA-WIDEBAND, AND COMPACT HIGH SELECTIVE MICROSTRIP BANDPASS FILTERS

A Dissertation

by

JI HYOUNG YU

Submitted to the Office of Graduate and Professional Studies of
Texas A&M University
in partial fulfillment of the requirements for the degree of

DOCTOR OF PHILOSOPHY

Chair of Committee,	Kai Chang
Committee Members,	Cam Nguyen
	Laszlo B. Kish
	Hae-Kwon Jeong
Head of Department,	Miroslav M. Begovic

December 2017

Major Subject: Electrical Engineering

ABSTRACT

As an indispensable component, microwave bandpass filters play a very important role in many modern wireless systems. They are used to carry out the selection of only the wanted frequencies from RF signals with various spurious frequencies. The reconfigurable filter with multi-band has attracted much attention for both research and industry because of the increasing importance in making RF components that have multi-function with compact size. Wide or Ultra-wideband (UWB) bandpass filters are becoming more and more in demand in many wireless applications due to the high data transmission rate. This dissertation focuses on the study of microwave filters with many applications in various wireless systems. Firstly, bandpass filters using stepped impedance stubs are presented. The resonant frequencies and transmission zeros are analyzed, and harmonic suppression by novel S-shaped coupled feed lines is presented. A resonator with a dual-band characteristic is introduced, and it is analytically shown that each passband can be independently controlled by the parameters of the resonator. PIN diodes are used to introduce an electrically controlled dual-band bandpass filter. Secondly, symmetric stepped impedance resonators with asymmetric stepped impedance stubs are also presented to develop Ultra-wide band (UWB) bandpass filters with and without a notched band. The resonant frequencies and transmission zeros of the resonator are effectively located to achieve a very wide passband and a high attenuation rate in rejection bands. The interdigital coupled feed lines with rectangular slots are designed for a better passband characteristic. A notched characteristic is introduced by using modified feed lines to avoid

the interferences with other existing signals. UWB bandpass filter performances in time-domain and frequency-domain are analyzed and discussed. Thirdly, UWB bandpass filters with a different configuration are developed. Similarly, the analyzed resonant frequencies are used to achieve a passband for UWB applications. A different technique is used to introduce a very narrow notched band within the passband. Time-domain analysis is made to verify the frequency-domain performance. Lastly, a very high selective wideband bandpass filter is presented using an inverted T-shaped resonator. The characteristic of the resonator is analyzed to design a bandpass filter with specified bandwidth. The short stubs are introduced to achieve a very high attenuation rate at both sides of the passband and a wide stopband characteristic. In summary, various microwave filters to meet the requirements of specific applications are studied and designed. Analysis and design methodology of the proposed microwave filters in this dissertation can be applied in many applications in wireless systems.

DEDICATION

To my parents

and

my wife, Eun Hye (Grace)

ACKNOWLEDGEMENTS

Thanks to the Lord for your immeasurable grace and love you have given to me. Thank you for your faithfulness and goodness that you always provide me a strength to face challenges in my life. I am grateful to the Lord for everything you have done for me.

I would like to thank my advisor, Dr. Kai Chang, for his guidance, patience and support with regards to my graduate studies and research. I deeply appreciate his dedication to the electromagnetic and microwave lab at Texas A&M University. It is an honor to have been his advisee. I will never forget his tremendous support and encouragement. Many thanks go to my committee members, Dr. Nguyen, Dr. Kish, and Dr. Jeong for their support and guidance throughout this dissertation.

I owe my deepest gratitude to my parents and parents-in-law for their dedication, boundless love, and ceaseless prayers in my life, and to my sisters for their patience and encouragement. Special thanks to my wonderful wife, Eun Hye (Grace), for her sincere support, encouragement, and incredible devotion during the long period of my graduate studies.

I would like to thank Pastor Lee and his wife for their wonderful support and prayer, and to my church brothers and sisters in U. S. and South Korea for their great encouragement.

Finally, thanks go to my friends and colleagues and the department faculty and staff for making my time at Texas A&M University a great experience.

CONTRIBUTORS AND FUNDING SOURCES

This work was supervised by a dissertation committee consisting of Professor Dr. Kai Chang and Professors Dr. Cam Nguyen and Dr. Laszlo B. Kish of the Department of Electrical Engineering and Professor Hae-Kwon Jeong of the Department of Chemical Engineering.

All work for the dissertation was completed by the student, under the advisement of Dr. Kai Chang of the Department of Electrical Engineering.

There are no outside funding contributions to acknowledge related to the research and compilation of this document.

TABLE OF CONTENTS

Page

Page

LIST OF FIGURES

Page

Page

Page

Page

Page

LIST OF TABLES

Page

CHAPTER I

INTRODUCTION

Recently, requirements for the performances of bandpass filters are becoming more and more rigorous. In particular, microwave bandpass filters with features such as compactness, low loss, harmonic suppression, wide stopband, and high selectivity have been widely used to enhance the performances of wireless systems. As wireless communication systems are required to employ various services with different frequencies, multi-band bandpass filters with reconfigurable capability play a crucial role in wireless multi-function systems, contributing to the realization of the compact-size systems.

As more communication services are supported in a wireless system, spurious harmonic responses can cause severe problems in wireless systems, such as radio frequency (RF) signal interferences and distortion. Generally speaking, the additional microwave filters are used to suppress the spurious harmonic responses, which cause increased circuit size and circuit loss. Thus, to prevent these problems and obtain a high-quality radio frequency (RF) signal, microwave filters with harmonic suppression are becoming more important for improved RF system performances

Over the last decade, reconfigurable microwave bandpass filters have attracted great attention because modern wireless systems are receiving a high demand for multi-band and multi-function operation. The microwave filters with controllable multi-band operation are essential for the realization of compact wireless systems. The capabilities of the reconfigurable microwave filters with independent control of each passband plays

more important roles to provide multi-service applications in next generation wireless systems.

As numerous radio frequency (RF) signals become more and more easily interfered in an increasingly crowded frequency spectrum environment, Ultra-wideband (UWB) technology has received a lot of attention as one of the solutions. Many advantages of UWB technology have enabled remarkable advances in UWB applications such as high-speed data transmission, secure communications, high-resolution ground-penetrating radar, through-wall imaging, and long-range applications [1], [2]. In particular, UWB bandpass filters are one of the most important components in UWB systems. The time-domain performance of UWB bandpass filters is as important as frequency-domain because UWB systems utilize very short pulses with a very low level of power spectral density (PSD) so that the energy of the pulses is spread over a wide range of frequencies. A notch band operation within the UWB frequency spectrum is becoming necessary to ensure avoidance of signal interferences.

As the frequency spectrum is becoming crowded, a high selectivity of microwave filters is necessary to improve the performances of radio frequency (RF) systems and reduce interferences with other existing signals. In general, high selectivity can be achieved by using a higher order of filters, causing bigger circuit size and higher insertion loss. Thus, a compact bandpass filter with a low loss and a high selectivity is preferable for enhanced performances in overall wireless systems. To meet these requirements, BPF design with parallel coupled lines employing short stubs is introduced in this work.

This dissertation consists of six chapters. Chapter II presents harmonic suppressed single- and dual-band bandpass filters, in which resonators with stepped impedance stubs and novel S-shaped coupled feed lines are used. The design formulas of the resonators with stepped impedance stubs are derived from the analysis of the resonant frequencies and transmission zeros. The characteristics of the S-shaped coupled feed lines are studied and compared to the characteristics of conventional parallel coupled and interdigital coupled feed lines. Based on the analysis of frequency characteristics of the dual-band resonator, it is presented that each band is independently controlled. Then, a dual-band bandpass filter with the capability to independently shift each band is developed. Chapter III introduces a novel UWB bandpass filter using a symmetric stepped impedance resonator with an asymmetric stepped impedance stub. The resonator is designed based on the analysis of resonant frequencies and transmission zeros. The characteristics of the interdigital coupled feed lines used to excite the resonator are studied in this chapter. The modified feed lines are introduced to achieve a notched band. The time-domain analysis of the proposed UWB bandpass filter is made for verification of the performance in time-domain. Chapter IV proposes a different type of UWB bandpass filter using a symmetric stepped impedance resonator and short stubs. The design formulas of this resonator are derived based on analysis of resonant frequencies. The characteristics of the interdigital coupled feed lines with short stubs are studied. A notch characteristic is introduced by modifying the feed lines. The time-domain performances of the proposed UWB bandpass filters are discussed. Chapter V presents a wideband bandpass filter with very high selectivity using an inverted T-shaped resonator. The analysis of the even and odd resonant

frequencies is used to design the resonator. The parallel coupled feed lines with short stubs are studied to achieve very high selectivity at both sides of the passband, comparing to the feed lines without short stubs. Chapter VI summarizes all the findings of the studies in this dissertation.

CHAPTER II

HARMONIC SUPPRESSED BANDPASS FILTER WITH INDEPENDENTLY CONTROLLABLE DUAL-BAND USING STEPPED IMPEDANCE STUBS

II.1. Introduction

The microwave filter is one of the most important components in diverse wireless communication and radar systems and to select or reject the RF/microwave signals. As the wireless communication and radar technology are developed rapidly, the characteristics of a low insertion loss within a passband, a wide stopband, and a sharp rejection at cutoff regions are becoming in high demand in designing bandpass filters (BPFs). For these BPFs, various structures such as stepped impedance resonators (SIR), ring resonators, defected ground structure(DGS), and left-handed materials (LHM) have been intensively studied. In particular, SIRs have been widely used due to their advantages, one of which is that the resonant frequencies of SIRs can be easily adjusted by the dimension of the resonator [3]. Wideband BPFs using a ring resonator with stepped impedance stubs have been proposed [4], and an ultra-wideband (UWB) BPF has been developed using a SIR [5]. Multi-mode SIRs were used to implement quasi-Chebyshev BPFs with 9 resonant frequencies [6], and dual-mode BPFs using a periodic stepped impedance ring resonator (PSIRR) were proposed for a miniaturized area and wide upper stopband characteristics [7].

Moreover, a demand for secure signal transmission without interference from other signals led to the development of the wide-stopband BPFs. Remarkable advanced

techniques for the wide-stopband have been obtained by suppressing the spurious responses. For example, a capacitive compensation technique was proposed [8], and corrugated coupled microstrip lines were used to suppress the spurious response at twice the center frequency [9]. In addition, open stubs and interdigital capacitors [10], a microstrip coupled-line hairpin [11], and a triple-mode stub-loaded resonator [12] were used for an extended upper stopband.

Furthermore, the filters with multi-band can make a system more compact, making it possible to use multi-communication services in a system. There have been many studies on these multi-band BPFs. For example, dual-band BPFs were developed based on resonant characteristics of a stepped impedance resonator [13], and asymmetric stepped impedance resonators were utilized to achieve controllable dual-band [14]. Dual mode ring resonators [15], pseudo-interdigital stepped impedance resonators [16], and stacked-loops [17] were used for implementation of dual-band BPFs.

Recently, reconfigurable filters are gaining great attention because of improved performance and increased functionality in wireless communication and radar systems. There have been vibrant studies on various types of reconfigurable filters. To obtain a reconfigurable filter, tuning components such as PIN diodes, varactors, PET, and MEMS are required to be integrated within a passive filter. The center frequency or bandwidth can be controlled by creating discrete states using tuning components. Tunable open-loop resonator filters using varactors was proposed to control the resonant frequencies [18], and a tunable bandpass filter with simultaneous frequency and bandwidth control was proposed using a combination of ferroelectric (BST) capacitors and cantilever MEMS

switches [19]. A ring resonator with multiple open stubs was used to control the passband bandwidth [20], and a piezoelectric transducer (PET) was used to tune the operating frequency of microwave circuits [21]. In addition, PIN diodes were used to switch the resonance conditions of the stepped impedance resonators [22]. MEMS tunable capacitors were used for both frequency and bandwidth tuning [23] by controlling the electric coupling of planar resonators and their resonant frequencies.

In this chapter, a dual-mode BPF with suppressed spurious responses is proposed using S-shaped coupled feed lines. The even and odd resonant frequencies for a dual-mode resonator with a stepped impedance stub are analyzed by the even and odd mode equivalent circuits, respectively. The ABCD matrix of the resonator is converted to obtain Y parameter to calculate the transmission zeros. Based on the calculated resonant frequencies and transmission zeros, the lengths and widths of each section of the stepped impedance stub are determined according to a desired 3-dB bandwidth of a bandpass filter. The frequency response of the S-shaped coupled feed lines is compared to those of conventional coupled and interdigital coupled feed lines to look into how to suppress harmonic responses by introducing multiple transmission zeros near the locations of spurious responses. After that, an independently controllable dual-band filter with suppressed spurious responses is developed for wireless local area network (WLAN) application operating in 2.4/5.2 GHz bands authorized by the Federal Communications Committee (FCC) for unlicensed use. To obtain dual-band operation, a dual-mode resonator is modified to have a strip line between two open circuited stepped impedance stubs. The parameters of the resonator are approximately calculated from the analyzed

even and odd resonant frequencies. In order to validate the spurious suppression of S-shaped coupled feed lines, the resonator is excited by S-shaped coupled feed lines. The result of the dual-band BPF excited by S-shaped coupled feed lines is compared to that of the dual-band BPF excited by conventional parallel coupled feed lines. The independent controllability of two passbands by the width variations of two stepped impedance stubs and the strip line between two stubs is demonstrated. Based on the analyzed results, a reconfigurable dual-band BPF with independently switchable passband is developed using PIN diodes. The proposed BPFs are designed on an RT/Duroid 6006 substrate with a thickness of 0.635 mm and a relative dielectric constant of 6.15. Electromagnetic (EM) simulations and circuit simulations are performed by Zeland IE3D based on method of moments and by ADS, respectively.

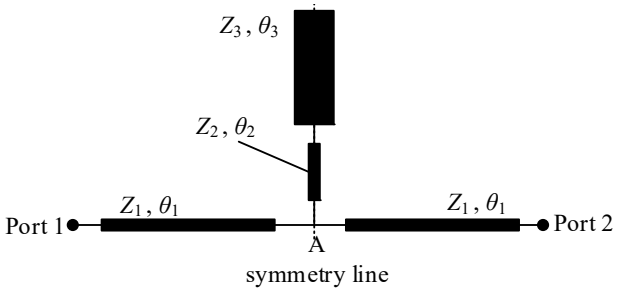

Fig. 1. A resonator with an open stepped impedance stub.

II.2. Analysis of a resonator with a stepped impedance stub

II.2.A. Resonant frequencies and transmission zeros

Fig. 1 shows the configuration of a resonator with an open stepped impedance stub. The open stepped impedance stub consists of two strip lines with different impedances.

The open stub is placed at the symmetry line to perturb the resonator. In Fig. 1, θ_1 and Z_1 are the electrical length and characteristic impedance for a half of the strip line in the resonator, respectively. Z_2 and Z_3 denote the characteristic impedances of each section of the stepped impedance stub, while θ_2 and θ_3 are the electrical lengths of the stub. Each electrical length and characteristic impedance correspond to the physical length and width of each line section, respectively.

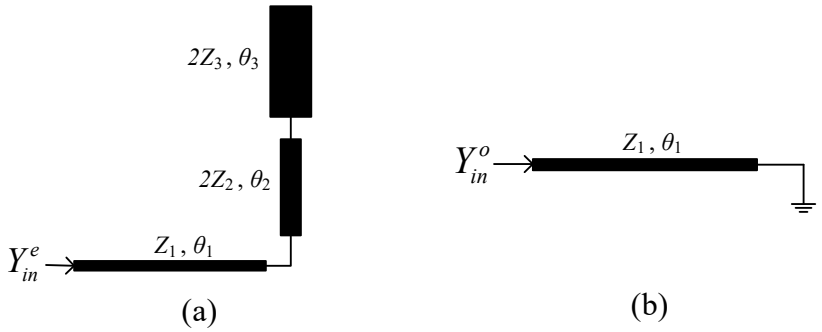

Fig. 2. Equivalent circuits of the resonator in Fig. 1. (a) even mode. (b) odd mode.

The even and odd mode distributed equivalent circuits are used to analyze the frequency responses of the resonator. The even and odd mode resonant frequencies do not interfere with each other, and the combination of the resonant frequencies represents the whole frequency response of a resonator because the even and odd mode resonant frequencies are orthogonal to each other and collectively exclusive. Fig. 2(a) and (b) show the equivalent circuits for the even and odd mode resonant frequencies, respectively. In Fig. 2(a), the characteristic impedances of the stepped impedance stub (Z_2 and Z_3) become double because the stub is cut in half with respect to the symmetry line in Fig. 1. In Fig.

2(b), the odd mode equivalent circuit becomes a simple short-circuited strip line because the symmetry line is connected to ground. The even and odd mode resonance responses of the resonator in Fig. 1 can be derived under the condition of $Z_{in}=\infty$ (or $Y_{in}=0$), and are obtained as follows:

$$Y_{in}^{e} = \tan\theta_1 + \frac{K_2 \tan\theta_2 + K_1 \tan\theta_3}{2K_1(K_2 - K_1 \tan\theta_2 \tan\theta_3)} = 0 \qquad \text{for even modes (1)}$$

and

$$Y_{in}^{o} = \tan^{-1}\theta_1 = 0 \qquad \text{for odd modes (2)}$$

, where $K_1= Z_2/Z_1$ and $K_2= Z_3/Z_1$.

In addition, the transmission zero frequencies, at which the signals cannot pass by the resonator, can be calculated under the condition of $Z_{12}=\infty$ (or $Y_{12}=0$), where Z_{12} or Y_{12} is obtained from an impedance or admittance matrix. The impedance or admittance matrix can be calculated by the conversion of the ABCD matrix of the resonator in Fig. 1. The ABCD matrix consists of three cascaded parts, where the ABCD matrix of the stepped impedance stub can be easily obtained by calculating the shunt admittance, which is seen when looking into the stub at point A in Fig. 1. The transmission zeros of the resonator in Fig. 1 can be expressed by:

$$Y_{21} = \frac{\csc\theta_1}{2\cos\theta_1 - \frac{\sin\theta_1}{K_1} \cdot \frac{K_2 \tan\theta_2 + K_1 \tan\theta_3}{K_2 - K_1 \tan\theta_2 \tan\theta_3}} = 0 \qquad (3)$$

Fig.3(a) and (b) show the first two even and the first odd mode resonant frequencies (f_{E1}, f_{E2}, and f_{O1}) and the transmission zeros (f_{Z1},f_{Z2}) normalized by the first odd mode resonant frequency (f_{O1}) against θ_2/θ_1 and θ_3/θ_1, respectively. In Fig. 3(a), θ_3/θ_1

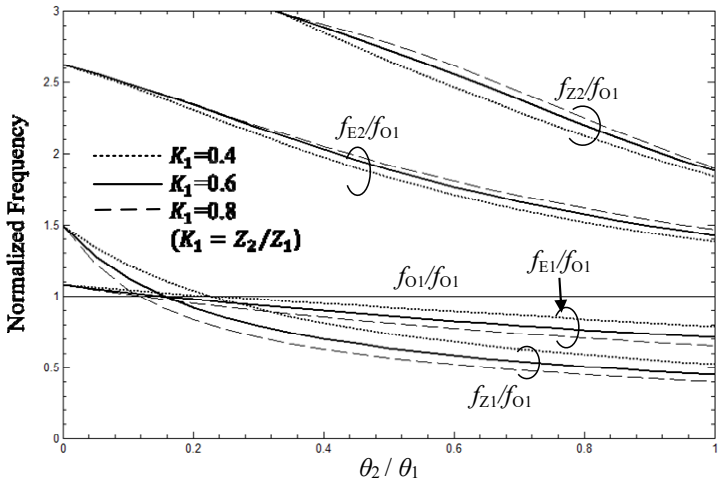

(a)

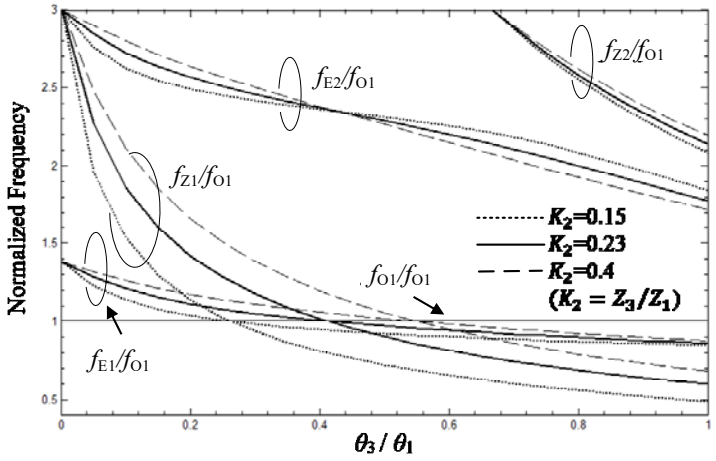

(b)

Fig. 3. Resonant frequencies (f_E: even mode, f_O: odd mode) and transmission zeros (f_Z) normalized by the first odd mode resonant frequency (f_{O1}) for the resonator in Fig. 1 with respect to (a) θ_2/θ_1 when K_2=0.23, θ_3/θ_1=0.53 and (b) θ_3/θ_1 when K_1=0.6, θ_2/θ_1=0.28.

and Z_3/Z_1 are set to be 0.53 and 0.23, respectively, while θ_2/θ_1 and Z_2/Z_1 are fixed at 0.28 and 0.6, respectively, as shown in Fig. 3(b). The first even and odd mode resonant frequencies (f_{E1} and f_{O1}) are used to make a passband. The passband bandwidth can be estimated by the difference between f_{E1} and f_{O1}. In Fig. 3(a) and (b), it is found that the mid-lower passband bandwidth increases as θ_2/θ_1 or θ_3/θ_1 moves to the higher values,

while the mid-upper passband bandwidth is hardly changed. In addition, K_1 and K_2 can also affect the passband bandwidth at a certain θ_2/θ_1 and θ_3/θ_1, respectively. The mid-lower passband bandwidth gradually increases when K_1 increases or K_2 decreases, as shown in Fig. 3(a) and (b), respectively. The characteristics exhibit the passband tunability of the resonator in Fig. 1. On the other hand, if the first transmission zero (f_{Z1}) is placed near the lower edge of the passband, f_{Z1} can be used to improve the skirt characteristic at the lower passband edge. Thus, θ_2/θ_1 and θ_3/θ_1 should be greater than the intersection point between f_{Z1}/f_{O1} and f_{O1}/f_{O1}, as in Fig.3 (a) and (b), respectively. It is also noticeable that the second even mode resonant frequency (f_{E2}) appears as the first spurious harmonic response, which need to be suppressed.

The physical length of l_1 is easily designed to be a quarter wavelength at the desired center frequency, while the parameters of the stepped impedance stub (θ_2/θ_1, θ_3/θ_1, Z_2/Z_1, and Z_3/Z_1) are determined according to the desired passband bandwidth. If a BPF with a fractional bandwidth (FBW) of 10% at the center frequency of 5 GHz is designed, the parameters of the resonator are as follows: $\theta_1=\pi/2$, $\theta_2/\theta_1=0.28$, $\theta_3/\theta_1=0.53$, $K_1=0.6$, and $K_2=0.23$, which correspond to $l_1=7.5$ mm, $l_2=2$ mm, $l_3=4$ mm, $w_1=0.2$ mm, $w_2=0.7$ mm, and $w_3=3.2$ mm.

II.2.B. Susceptance slope parameter of the resonator with the stepped impedance stub

As a basis establishing for the resonance properties of resonators regardless of their form, it is convenient to specify the resonant frequency and their slope parameter of the

resonators [24]. For any resonator with a shunt-type resonator, the susceptance slope parameter can be expressed as follows:

$$b = \frac{\omega_0}{2} \cdot \left. \frac{dB}{d\omega} \right|_{\omega=\omega_0} \tag{4}$$

where B is the susceptance of the resonator and ω_0 is angular frequency at the resonant frequency. For the resonator with a stepped impedance stub, (4) is not adequate to obtain the susceptance slope parameter, so the modified definition is used, which can be expressed by:

$$b = \frac{\theta_0}{2} \cdot \left. \frac{dB}{d\theta} \right|_{\theta=\theta_0} \tag{5}$$

The input admittance of the resonator in Fig. 1 can be given by:

$$Y_{in} = -jY_1 \cdot \frac{Y'\left(Y'\tan\theta_2 + Y''\tan\theta_3\right) + 2\tan\theta_1\left(Y' - Y''\tan\theta_2\tan\theta_3\right)}{Y'\tan\theta_1(Y'\tan\theta_2 + Y''\tan\theta_3) - \left(1-\tan^2\theta_1\right)\left(Y' - Y''\tan\theta_2\tan\theta_3\right)} \tag{6}$$

where $Y' = Y_2/Y_1$ and $Y'' = Y_3/Y_1$.

Based on (5), the susceptance slope parameter of the resonator in Fig. 1 can be obtained by the sum of partial derivatives with respect to each electrical length at the resonance condition, which is expressed as follows:

$$b = \frac{\theta_1}{2} \cdot \left. \frac{\partial B}{\partial \theta_1} \right|_{\substack{\theta_1=\theta_{10} \\ \theta_2=\theta_{20} \\ \theta_3=\theta_{30}}} + \frac{\theta_2}{2} \cdot \left. \frac{\partial B}{\partial \theta_2} \right|_{\substack{\theta_1=\theta_{10} \\ \theta_2=\theta_{20} \\ \theta_3=\theta_{30}}} + \frac{\theta_3}{2} \cdot \left. \frac{\partial B}{\partial \theta_3} \right|_{\substack{\theta_1=\theta_{10} \\ \theta_2=\theta_{20} \\ \theta_3=\theta_{30}}} \tag{7}$$

where θ_{10}, θ_{20}, and θ_{30} are the electrical lengths for θ_1, θ_2, and θ_3 at the resonance, respectively. By substituting (6) into (7), the susceptance slope parameter of the resonator in Fig. 1 can be derived as follows:

$$b = Y_1\left(\theta_{10} + \theta_{20} + \theta_{30}\right) \tag{8}$$

The susceptance slope parameter for a conventional half-wavelength resonator can be obtained by substituting $\theta_{10} = \pi/2$, $\theta_{20} = \theta_{30} = 0$, and $Y_1 = Y_0$ into (8), which is calculated as the following well-known equation:

$$b = \frac{\pi}{2} \cdot Y_0 \tag{9}$$

II.3. Design of BPF with parallel coupled feed lines

Fig.4 shows the configuration of a BPF with a stepped impedance stub excited by conventional parallel coupled feed lines. l_c denotes the length of the parallel coupled sections of the BPF, and w_c is set to be w_1 for a symmetric coupling. g_1 and g_2 denote the slot widths of the parallel coupled lines of the BPF. 50 Ω lines are used at the input and output ports, and the impedance transition sections between the ports and w_c are used to improve an impedance matching as shown in Fig. 4.

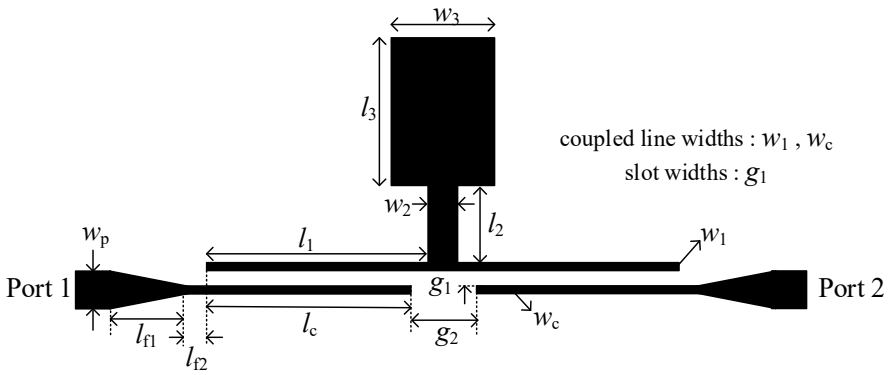

Fig. 4. The resonator with a stepped impedance stub fed by parallel coupled feed lines.

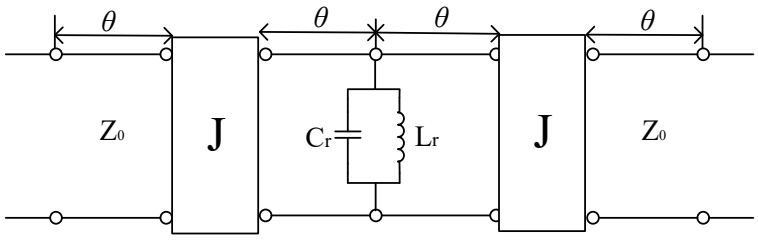

Fig. 5. Equivalent circuit of the BPF with parallel coupled feed lines in Fig. 4.

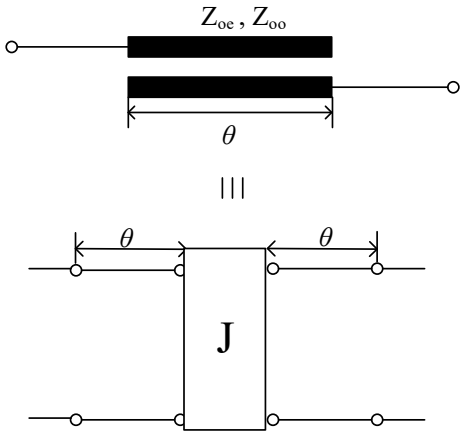

Fig. 6. Parallel coupled line and its equivalent circuit.

Fig. 5 shows the equivalent circuit of the BPF in Fig. 4. The stepped impedance stub is indicated by L_r and C_r, and J represents the admittance inverter parameter. To design the parallel coupled feed lines using the admittance inverter in Fig. 5, the equivalent circuit of the parallel coupled lines is used as shown in Fig. 6, where Z_{oe} and Z_{oo} denote the even and odd mode characteristic impedances, respectively. In Fig. 6, the admittance inverter is connected by two strip lines with the electrical length of θ and the characteristic impedance of Z_0 at the input and output ports. The even and odd mode analysis method is applied to figure out the relationship between the characteristic impedances and the

admittance inverter. By equating each ABCD matrix corresponding to two circuits in Fig. 6, the even and odd mode characteristic impedances are obtained as follows:

$$Z_{oe} = Z_0 \cdot \frac{1 + \left(J / Y_0\right)\csc\theta + \left(J / Y_0\right)^2}{1 - \left(J / Y_0\right)^2 \cot^2\theta} \tag{10}$$

and

$$Z_{oo} = Z_0 \cdot \frac{1 - \left(J / Y_0\right)\csc\theta + \left(J / Y_0\right)^2}{1 - \left(J / Y_0\right)^2 \cot^2\theta} \tag{11}$$

In the case where the electrical length (θ) is around $\pi/2$, which corresponds to a quarter-wavelength line, (10) and (11) can be simplified as follows:

$$Z_{oe} = Z_0 \cdot \left(1 + J/Y_0 + \left(J/Y_0\right)^2\right) \tag{12}$$

and

$$Z_{oo} = Z_0 \cdot \left(1 - J/Y_0 + \left(J/Y_0\right)^2\right) \tag{13}$$

Table 1. Design parameters of the BPF with conventional parallel coupled lines.

Design Parameters for the BPF in Fig. 4	Calculated results
Slope parameter	0.0295
FBW	10 %
Center frequency	5 GHz
Even mode impedance	128 Ω
Odd mode impedance	59 Ω
J inverter parameter	0.0056

Based on the above analysis, the design parameters of the BPF with parallel coupled feed lines in Fig. 4 are calculated and shown in Table 1.

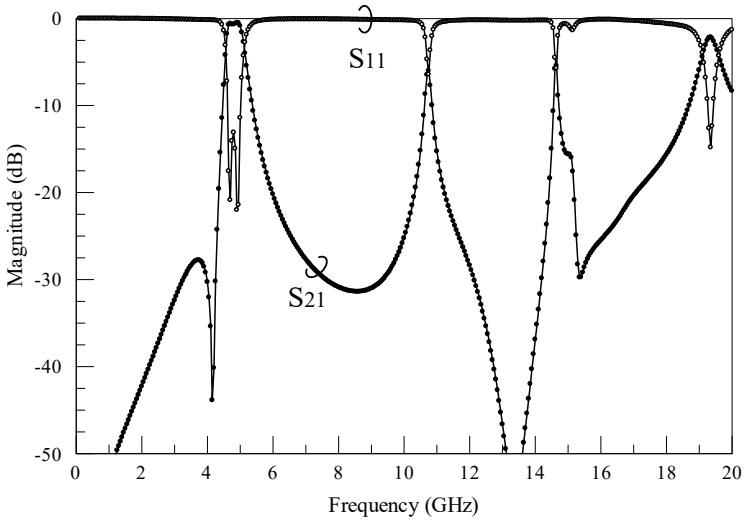

Fig. 7. Simulated frequency responses of the BPF with parallel coupled feed lines in Fig. 4 when l_1=7.5 mm, l_2=2 mm, l_3 =4 mm, l_c=6.55 mm, l_{f1}=3 mm, l_{f2}=1.2 mm, w_1=0.2 mm, w_2=0.7 mm, w_3=3.2 mm, w_c=0.2 mm, w_p=0.91 mm, g_1=0.2 mm, and g_2=1.9 mm.

Fig. 7 shows the simulated frequency responses of the BPF with the parallel coupled feed lines in Fig. 4. The dimensions of the resonator are as follows: l_1=7.5 mm, l_2=2 mm, l_3 =4 mm, w_1=0.2 mm, w_2=0.7 mm, and w_3=3.2 mm. The results in Table 1 are used to design the parallel coupled feed lines, which are calculated as follows: w_1=0.2 mm, w_c=0.2 mm and g_1=0.2 mm. The impedance transition section (l_{f1}, l_{f2}) of the ports is designed by EM simulations for a better return loss. In Fig. 7, it is found that there are two resonant frequencies within the passband, and a transmission zero near the lower edge of the passband improves the skirt characteristic of the lower passband edge, as analyzed in Fig. 3(a) and (b). In addition, it is noticeable that the first, second and third harmonic

responses are observed at 10.7 GHz, 14.6 GHz, and 19.4 GHz, sequentially. The harmonic responses can cause severe problems, such as interferences and distortions in wireless systems. In next section, a BPF is designed to suppress the undesired harmonic responses by using S-shaped coupled feed lines.

II.4. Characteristics of BPF with S-shaped coupled feed lines

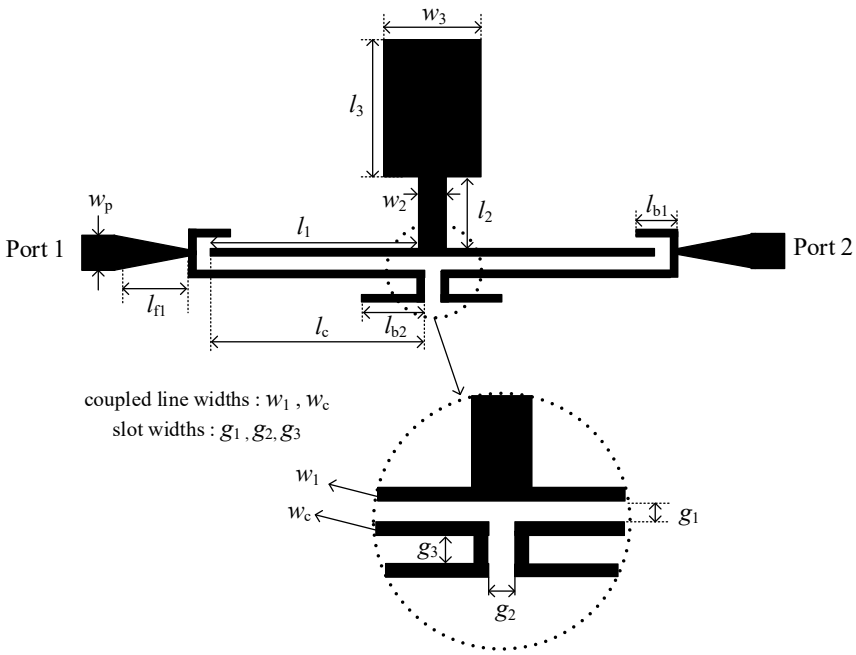

Fig. 8. The resonator with a stepped impedance stub fed by S-shaped coupled feed lines.

Fig. 8 shows the configuration of a BPF where the parallel coupled feed lines shown in Fig. 4 are replaced by S-shaped coupled feed lines, while the same resonator is used. The widths of the feed lines (w_c) are set to be the same as w_1 for a symmetric coupling, and the slot widths are denoted by g_1, g_2, and g_3. l_{b1} and l_{b2} are the lengths of the

upper and lower sections of the feed lines, respectively, as shown in Fig. 8. The line lengths (l_{b1}, l_{b2}) and slot widths (g_1, g_2, and g_3) of the feed lines are determined by EM simulations to achieve a wide stopband characteristic.

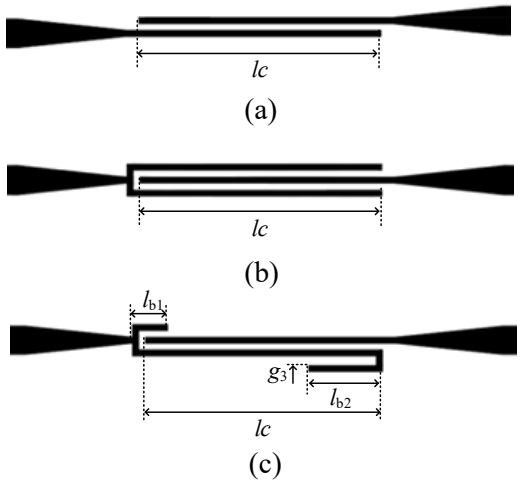

Fig. 9. Schematic diagrams of (a) a conventional parallel coupled feed line, (b) an interdigital coupled feed line, and (c) a S-shaped coupled feed line.

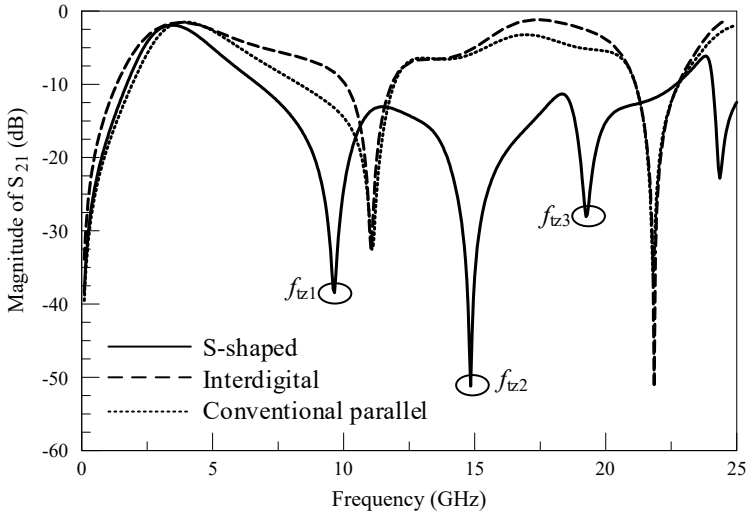

Fig. 10. Simulated frequency responses for three different feed lines in Fig. 9 when l_{b1}=1.1 mm, l_{b2}=2.3 mm, l_C=7.4 mm, and g_3=0.3 mm.

To examine the frequency characteristic, the S-shaped coupled feed lines in Fig. 9(c) are compared with conventional parallel coupled and interdigital coupled feed lines in Fig. 9 (a) and (b), respectively.

Fig. 10 shows the simulated frequency responses for three different feed lines in Fig. 9. The lengths of the coupled section (l_c) are set to be same in all cases of Fig. 9(a), (b), and (c). In Fig. 10, it is found that the conventional parallel coupled and interdigital coupled feed lines have the same transmission zeros at about 11 GHz and 22 GHz within the upper stopband, and the stopband characteristics near the transmission zeros are significantly similar to each other. On the other hand, the first three transmission zeros of the S-shaped coupled feed line within the upper stopband are produced at about 9.6 GHz, 14.8 GHz, and 19.3 GHz. It is also found that the upper stopband characteristic of the S-shaped coupled feed line is significantly improved over a wide range of frequencies compared to the parallel coupled and interdigital coupled feed line as shown in Fig. 10. The transmission zeros produced by the S-shaped coupled feed lines are used to suppress the harmonic responses.

The transmission zeros within the upper stopband for the S-shaped coupled feed line can be adjusted by the dimensions of the feed lines. Fig. 11 shows the effects of the feed line parameters (l_{b1}, l_{b2}, lc, and g_3) on the locations of the first three transmission zeros within the upper stopband. In Fig. 11(a), it is found that the first three transmission zeros decrease as l_{b1} increases. In Fig. 11(b) and (c), it is also found that the second transmission zero moves to the lower frequency with increased l_{b2} and g_3, while the first and third transmission zeros are hardly changed. In addition, in Fig. 11(d), the first and third trans-

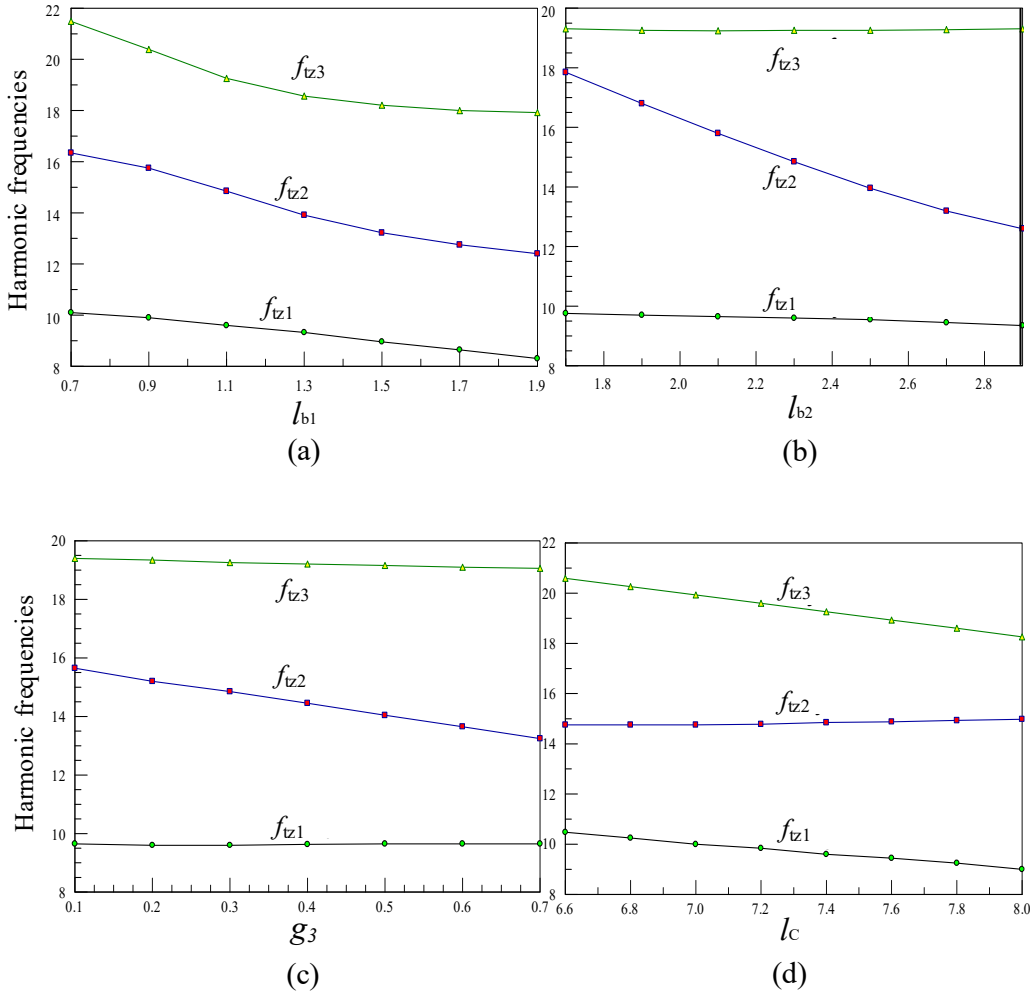

Fig. 11. Transmission zeros produced by the S-shaped coupled feed lines in Fig. 9(c) with regard to varying (a) l_{b1}, (b) l_{b2}, (c) lc, and (d) g_3.

mission zeros decrease at almost the same ratio as lc increases, while the second transmission zero frequency is hardly changed. Thus, the second transmission zero frequency (f_{tz2}) and a pair of the first and third transmission zero frequencies (f_{tz1}, f_{tz3}) can be independently adjusted to effectively suppress harmonic responses. Based on the frequency characteristics of the S-shaped coupled feed line in Fig. 11, the BPF with a wide

stopband characteristic is designed by locating transmission zeros at the spurious harmonic responses as shown in Fig. 8.

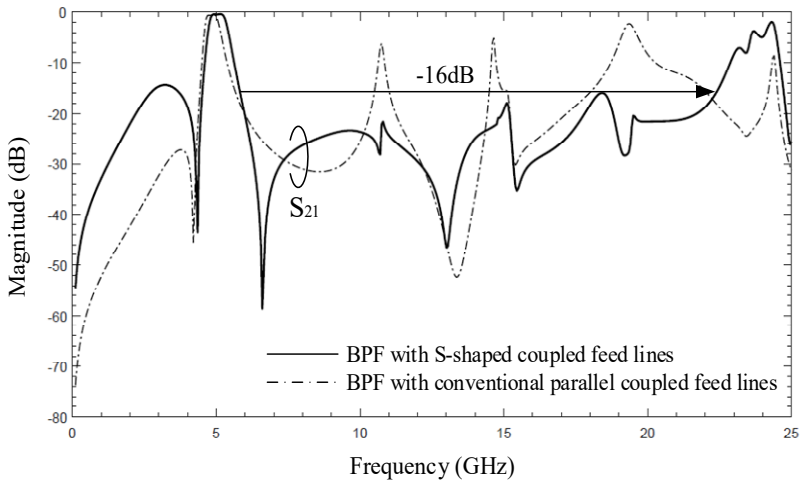

Fig. 12. Simulated frequency responses for the BPFs with the S-shaped coupled feed lines in Fig. 8 and with conventional parallel coupled feed lines in Fig. 4.

Fig. 12 shows the simulated frequency responses of the BPF fed by the S-shaped coupled feed lines as in Fig. 8, and the results of the BPF with conventional parallel coupled feed lines as in Fig. 4 are compared in the same figure. The dimensions of the BPF with the parallel coupled feed lines are the same as in Fig. 7. The dimensions of the S-shaped coupled feed lines are selected as follows: l_{b1}=1.1 mm, l_{b2}=2.3 mm, l_C=7.4 mm, and g_3=0.3 mm. In Fig. 12, for BPF with the S-shaped coupled feed lines, it is found that the transmission zero frequency close to the upper edge of the passband significantly improves the attenuation rate in the upper cutoff region and makes the passband symmetric. The additional transmission zeros caused by the S-shaped coupled feed lines within the upper stopband extend the upper stopband bandwidth up to 23 GHz at a

suppression level of 16 dB. It is also found that the passband of the BPF with S-shaped coupled feed lines is slightly shifted to the right, which is caused by the coupling changed by l_{b1} and l_{b2} of S-shaped coupled feed lines.

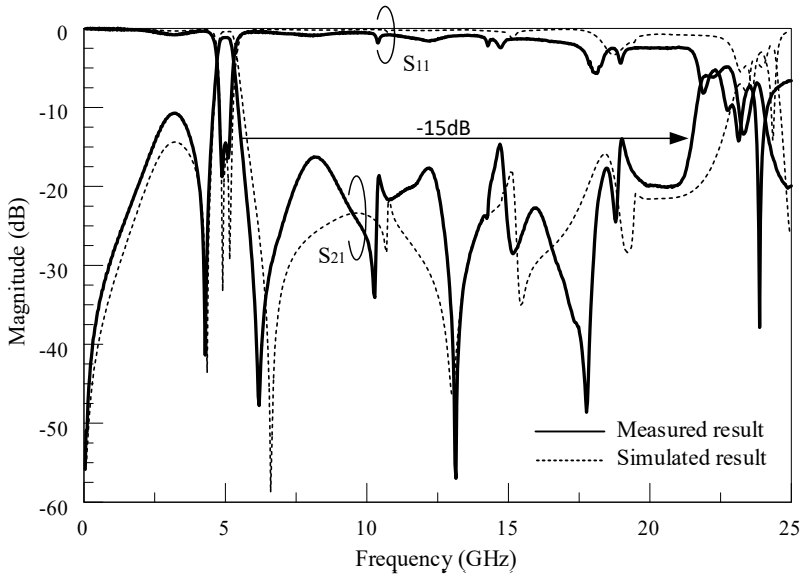

Fig. 13. Simulated and measured frequency responses of the BPF with S-shaped coupled feed lines in Fig. 8 when l_1=7.5 mm, l_2=2 mm, l_3 =4 mm, l_C=7.4 mm, l_{f1}=3 mm, l_{b1}=1.1 mm, l_{b2}=2.3 mm, w_1=0.2 mm, w_2=0.7 mm, w_3=3.2 mm, w_c=0.2 mm, w_p=0.91 mm, g_1=0.2 mm, g_2=0.2 mm, and g_3=0.3 mm.

Fig. 13 shows the simulated and measured results for the BPF with the S-shaped coupled feed lines in Fig. 8. As analyzed in Fig. 3, it is found that there are two resonant frequencies within the passband. The proposed BPF provides a 3-dB FBW of 10.5 %, a measured insertion loss of less than 1.1 dB, and a return loss of greater than 15 dB within the passband. The attenuation slopes of the BPF are 95 dB/GHz and 74 dB/GHz at the lower and upper passband edges, respectively. The measured upper stopband bandwidth is extended up to 22 GHz at a suppression level of 15 dB. The BPF has promising features

such as a symmetric passband, sharp cutoff characteristics, and a wide stopband. Comparing the simulated and measured results in Fig. 13 shows that the proposed BPF works very well.

II.5. Dual-band BPF with suppressed harmonic responses

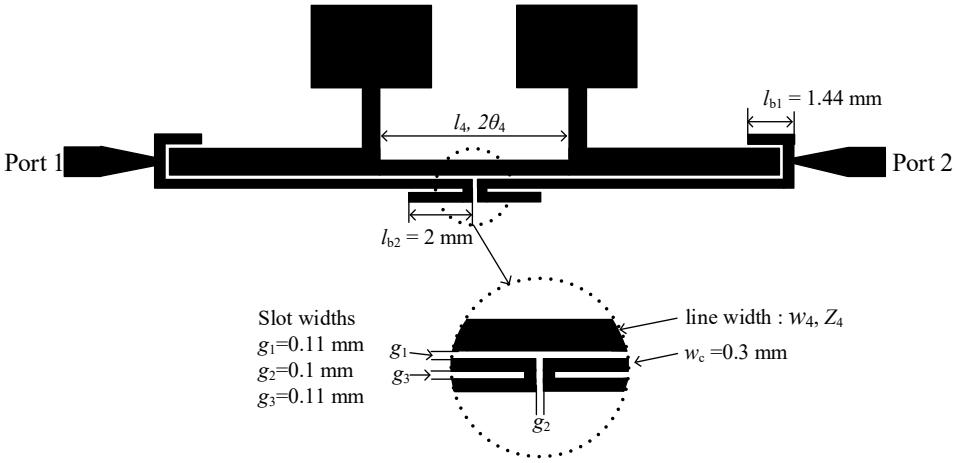

Fig. 14. Dual-band BPF with S-shaped coupled feed lines.

Fig. 14 shows the configuration of a dual-band BPF with S-shaped coupled feed lines where a strip line is connected between two stepped impedance stubs. θ_4 and Z_4 are the electrical length and characteristic impedance of the strip line between two stubs, respectively, which correspond to the physical length (l_4) and width (w_4) as shown in Fig. 14.

To examine the frequency characteristics of the dual-band resonator with two stepped impedance stubs, the even and odd mode resonant frequencies of the resonator are calculated as follows:

$$Y_{in}^{e} = \frac{K_3 \cdot X + K_1 \tan\theta_4 + K_1 K_3 \tan\theta_1}{K_1 K_3 - \tan\theta_1 (K_3 \cdot X + K_1 \tan\theta_4)} = 0 \qquad \text{for even modes (14)}$$

where

$$X = \frac{K_1 \tan\theta_3 + K_2 \tan\theta_2}{K_2 - K_1 \tan\theta_2 \tan\theta_3}$$

and

$$Y_{in}^{o} = \frac{K_3 \cdot X - K_1 \cot\theta_4 + K_1 K_3 \tan\theta_1}{K_1 K_3 - \tan\theta_1 (K_3 \cdot X - K_1 \cot\theta_4)} = 0 \qquad \text{for odd modes (15)}$$

where K_3 is defined as Z_4/Z_1.

The resonator is designed to operate in both 2.4 GHz and 5.2 GHz bands for WLAN applications. The design parameters of the resonator are calculated as follows: θ_2/θ_1=0.354, θ_3/θ_1=0.427, θ_4/θ_1=0.5, K_1=1.3, K_2=0.37, and K_3=1.18, that is, l_1=6.03 mm, l_2=1.86 mm, l_3=2.5 mm, l_4=5.86 mm, w_1=0.85 mm, w_2=0.5 mm, w_3=3.7 mm, and w_4=0.61 mm, sequentially.

Fig. 15(a) and (b) show the first three even mode resonant frequencies and the first three odd mode resonant frequencies normalized by π/2 against Z_1/Z_2 and Z_1/Z_4 under different values of θ_2/θ_1 and θ_4/θ_1, respectively. In Fig. 15(a), θ_4/θ_1 and Z_1/Z_4 are fixed at 0.5 and 0.85, respectively, while θ_2/θ_1 and Z_1/Z_2 are fixed at 0.35 and 0.77, respectively, in Fig.15 (b). In Fig. 15(a), it is observed that the first odd mode frequency (f_{O1}) approaches the second even mode frequency (f_{E2}) as Z_1/Z_2 increases. In addition, it is noticeable that as θ_2/θ_1 decreases, the value of Z_1/Z_2 at the intersection between f_{O1} and f_{E2} decreases. Moreover, it is found that the first, second, and third spurious harmonic responses are created at the locations of f_{O2}, f_{E3}, and f_{O3}, respectively.

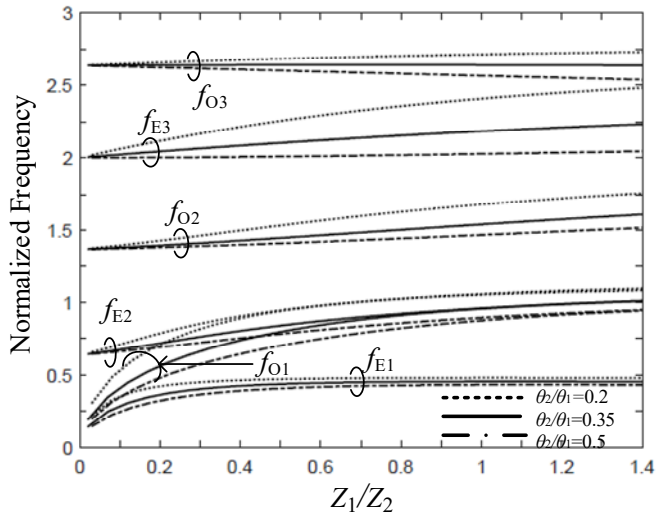

(a)

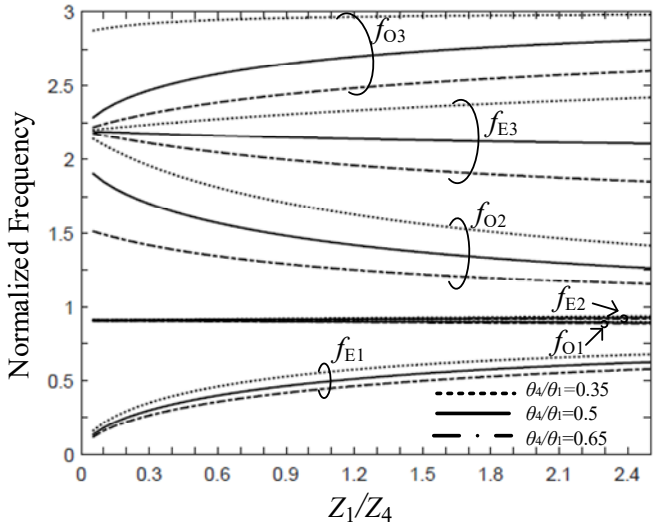

(b)

Fig. 15. Resonant frequencies (f_E: even mode, f_O: odd mode) normalized by the electrical length ($\pi/2$) for the resonator with two stepped impedance stubs in Fig. 14 with regard to (a) Z_1/Z_2 when θ_4/θ_1=0.5, Z_1/Z_4=0.85 and (b) Z_1/Z_4 when θ_2/θ_1 =0.35, Z_1/Z_2=0.77.

For a dual-band operation, the first even mode frequency (f_{E1}) is used for the first passband of 2.4 GHz, while the first odd mode and second even mode frequencies (f_{O1}, f_{E2}) are used for the second passband of 5.2 GHz. To design the dual-band resonator in

Fig. 14, the normalized resonant frequencies of f_{E1}, f_{O1}, and f_{E2} are selected by the following equation:

$$\frac{f_{O1}+f_{E2}}{f_{E1}}=\frac{13}{3} \tag{16}$$

After f_{E1}, f_{O1}, and f_{E2} are properly selected, the parameters of as θ_2/θ_1, θ_4/θ_1, Z_1/Z_2, and Z_1/Z_4 are found in Fig. 15 (a) and (b).

Furthermore, Fig. 15 shows the independent tunability of each passband of the dual-band BPF in Fig. 14. In Fig. 15(a), it is found that for a Z_1/Z_2 greater than 0.2, the values of f_{O1} and f_{E2} are changed, while f_{E1} is hardly changed. This characteristic is used to independently control the second passband. In Fig. 15(b), it is also found that f_{E1} gradually increases with increased Z_1/Z_4, while the values of f_{O1} and f_{E2} are almost constant. This characteristic is used to independently control the first passband.

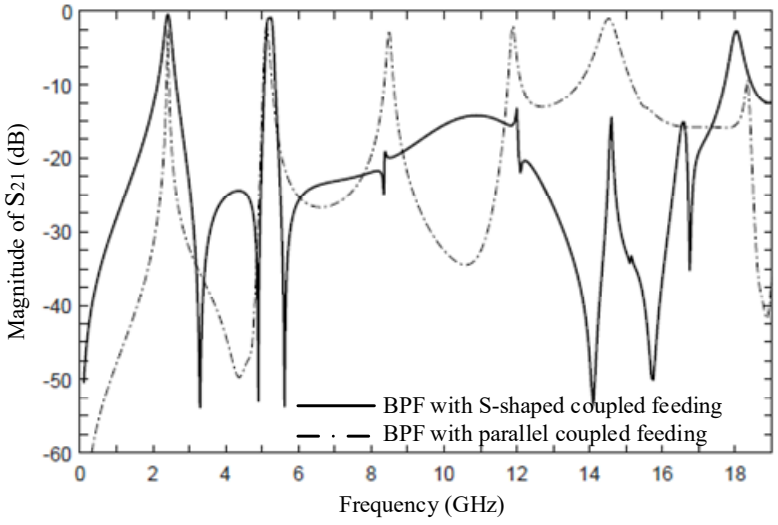

Fig. 16. Simulated frequency responses for the dual-band BPFs with S-shaped coupled and parallel coupled feed lines.

Fig. 16 shows the simulated frequency response of the dual-band BPF with the S-shaped coupled feed lines as in Fig. 14. The results of the dual-band BPF with conventional parallel coupled feed lines are compared in the same figure. As analyzed in Fig. 15(a) and (b), the first passband is created by the first even mode resonant frequency (f_{E1}), while the second passband is introduced by the first odd mode and second even mode resonant frequencies (f_{O1}, and f_{E2}).

In Fig. 16, for BPF with the parallel coupled feed lines, it is found that the first three harmonic responses appear at about 8.5 GHz, 12 GHz, 14.5 GHz. To suppress the harmonic responses, the transmission zeros need to be located near harmonic responses. In Fig. 16, for BPF with S-shaped coupled feed lines, it is observed that the first three harmonic responses are suppressed by the transmission zeros, resulting in a wide stopband characteristic. Therefore, it is verified that the S-shaped coupled feed lines can be used to achieve a wide stopband for a dual-band BPF as well as a single-band BPF.

Fig. 17(a) and (b) show the simulated frequency responses of the dual-band BPF in Fig. 14 with varying w_4 and w_2, respectively. In Fig. 17 (a), as w_4 increases, the first passband moves toward the higher frequency band, while the second passband is hardly changed. In addition, in Fig. 17(b), as w_2 increases, the second passband moves toward the higher frequency band, while the first passband is hardly changed. Moreover, it is noticeable that the transmission zero frequency close to the upper edge of the second passband is hardly changed although the second passband is changed as in Fig. 17(b). The transmission zero frequency limits the variation of the second passband, which is mainly affected by the gap (g_2) between two S-shaped coupled feed lines. As g_2 increases, the

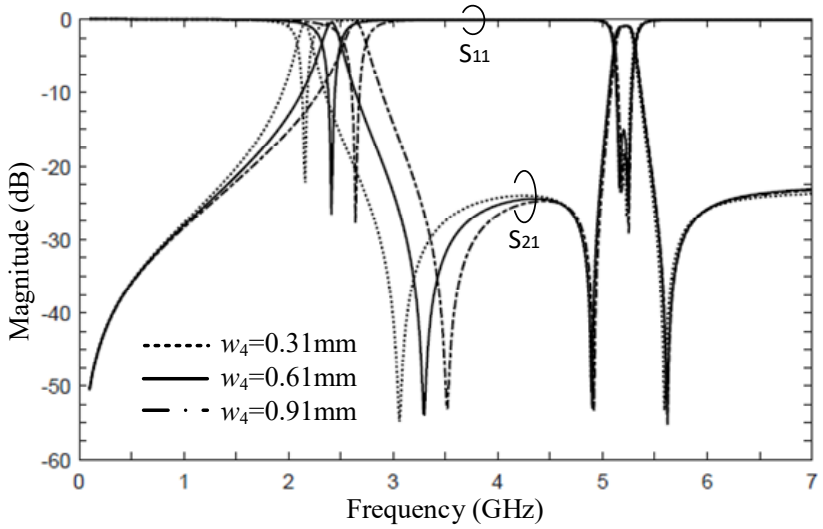

(a)

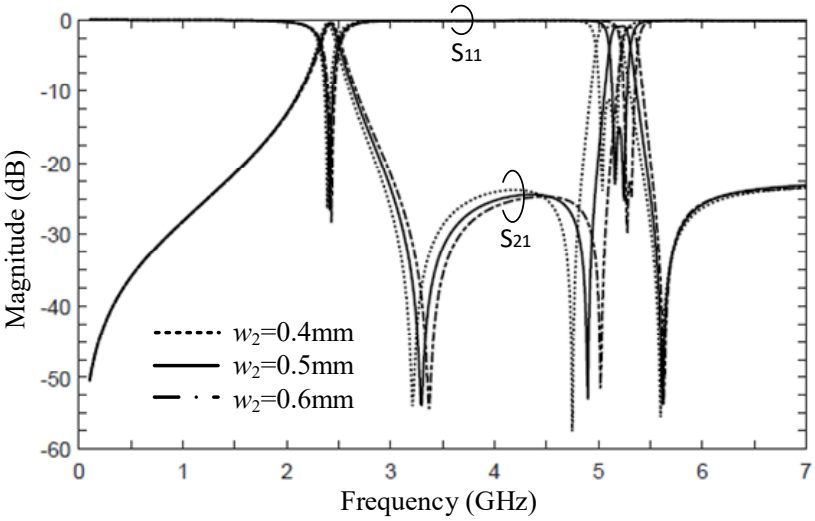

(b)

Fig. 17. Independently controllable dual-band characteristics of BPF in Fig. 14 with varying (a) w_4 and (b) w_2.

transmission zero frequency close to the upper edge of the second passband moves toward the higher frequency. The variation limitation of the second passband is increased, but the attenuation rate at the upper edge of the second passband can be decreased. Thus, g_2 is

determined by considering the variation limitation of the second passband and the attenuation rate at the upper edge of the second passband.

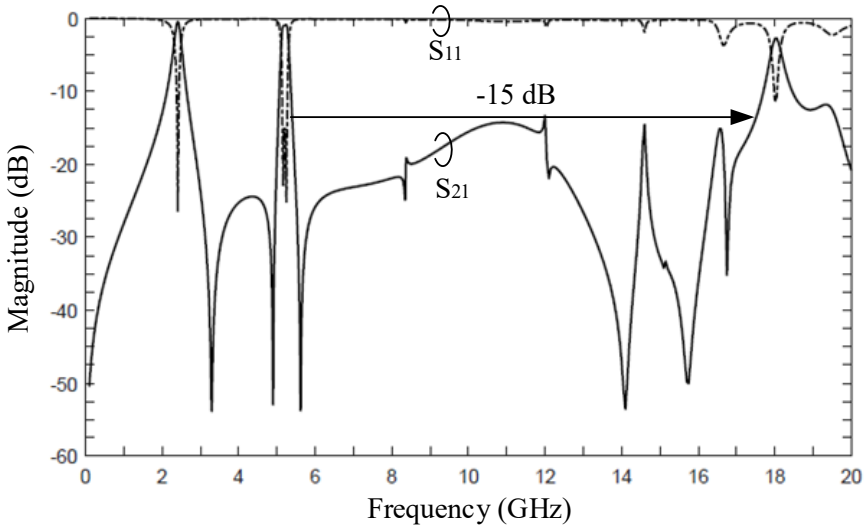

Fig. 18. Simulated frequency responses of the dual-band BPF in Fig. 14 when l_1=6.03 mm, l_2=1.86 mm, l_3=2.5 mm, l_4=5.86 mm, l_{b1}=1.44 mm, l_{b2}=2 mm, w_1=0.85 mm, w_2=0.5 mm, w_3=3.7 mm, w_4=0.61 mm, w_c=0.3 mm, g_1=0.11 mm, g_2=0.1 mm, and g_3=0.11 mm.

Fig. 18 shows the simulated frequency responses of S_{21} and S_{11} for the dual-band BPF in Fig. 14. All dimensions of the dual-band BPF are as follows: l_1=6.03 mm, l_2=1.86 mm, l_3=2.5 mm, l_4=5.86 mm, l_{b1}=1.44 mm, l_{b2}=2 mm, w_1=0.85 mm, w_2=0.5 mm, w_3=3.7 mm, w_4=0.61 mm, w_c=0.3 mm, g_1=0.11 mm, g_2=0.1 mm, and g_3=0.11 mm. The proposed dual-band BPF provides a 3-dB FBW of 7 % and 3.5 % for the first and the second passband, respectively. For the first passband, the insertion loss and the return loss are 0.45 dB and 27 dB at the center frequency, respectively. Also, for the second passband, the insertion loss is 0.9 dB at the center frequency and the return loss are better than 15

dB within the passband. The upper stopband is extended up to about 17.5 GHz with the suppression level 15dB, which is about 7.3 times the first operating passband.

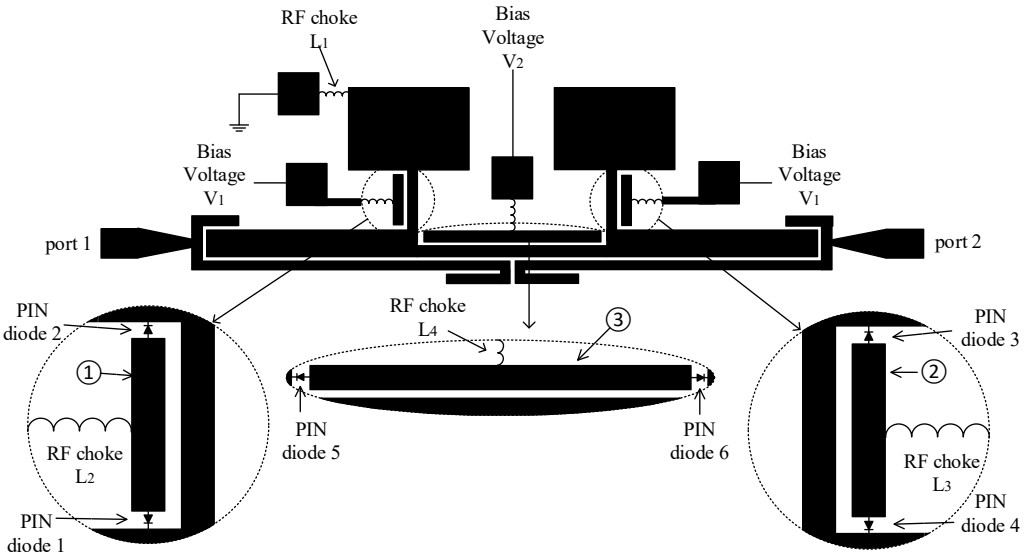

Fig. 19. Reconfigurable dual-band BPF.

II.6. Reconfigurable BPF with independently controllable dual-band

Fig. 19 shows the configuration of a reconfigurable dual-band BPF. The six PIN diodes are used as switches to make two discrete states of each passband, resulting in the capability of an independent control of the two passbands. Four inductors are used to choke RF signals, and one via hole is required as a ground for DC voltages. The PIN diodes are placed at gaps between the resonator and strip lines (1~3) as shown in Fig. 19. If the PIN diodes are turned either on or off by two bias voltages (V_1 and V_2), the resonator is either connected or disconnected to the strip lines, respectively. Each passband is independently controlled by controlling bias voltage of V_1 and V_2.

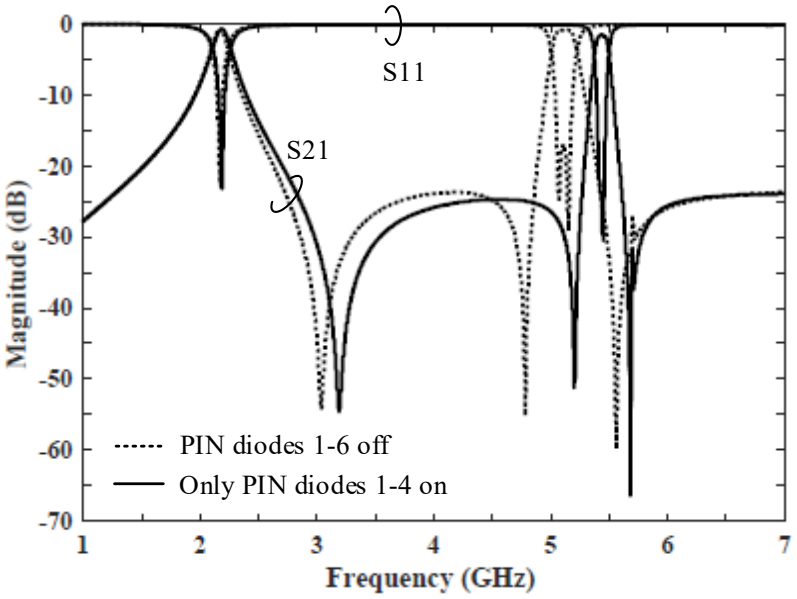

(a)

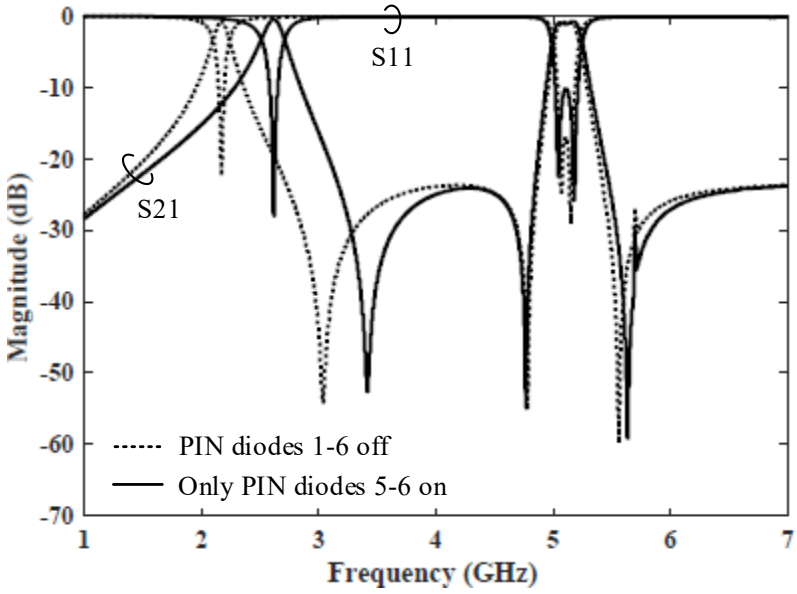

(b)

Fig. 20. Independently switchable dual-band BPF in Fig. 19 (l_1=6.03 mm, l_2=1.86 mm, l_3=2.5 mm, l_4=5.86 mm, l_{b1}=1.44 mm, l_{b2}=2 mm, w_1=0.85 mm, w_2=0.4 mm, w_3=3.7 mm, w_4=0.3 mm, w_c=0.3 mm, g_1=0.11 mm, g_2=0.1 mm, and g_3=0.11 mm) when (a) only PIN diodes (1-4) are turned ON, (b) PIN diodes (5-6) ON, and (c) all PIN diodes (1~6) ON.

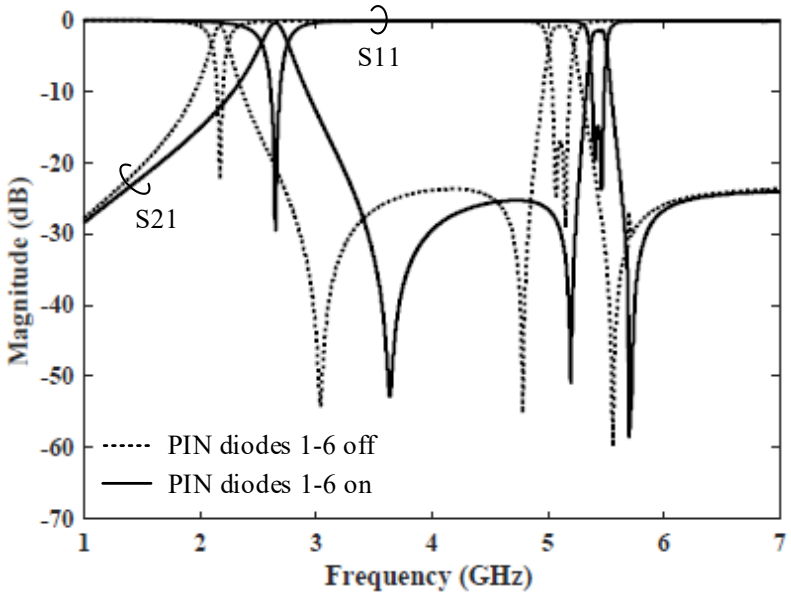

(c)

Fig. 20 Continued.

Fig. 20 shows the simulated results for four different states of the dual-band BPF in Fig. 19. The frequency response of the dual-band BPF when all PIN diodes are turned off is compared in Fig. 19(a), (b), and (c). All the dimensions for the dual-band BPF are the same as the results in Fig. 18 except w_2=0.4 mm and w_4 = 0.3 mm. The widths of line (1 and 2) are 0.2 mm, while the width of line (3) is 0.5 mm. By applying the bias voltage V_1, the PIN diodes (1~4) are turned on. Then, the resonator is connected with lines (1 and 2), resulting in increased w_2. As analyzed in Fig. 17(b), when w_2 increases, the second passband is shifted to the higher frequency band, while the first passband is hardly changed. The results of when the PIN diodes (1~4) are turned on are shown in Fig. 20(a). Similarly, if the bias voltage V_2 is applied, the PIN diodes (5~6) are turned on, and then the resonator is connected to line (3), resulting in increased w_4. As analyzed in Fig. 17(a),

when w_4 increases, the first passband moves toward the higher frequency band, while the second passband is hardly changed. The results of when the PIN diodes (5~6) are turned on are shown in Fig. 20(b). When V_1 and V_2 are applied, all PIN diodes are turned on, and then the resonator is connected to all the lines (1, 2, and 3), resulting in increased w_2 and w_4. As analyzed in Fig. 17(a) and (b), when w_2 and w_4 increase, both the first and second passbands move to the higher frequency band. The results of when all the PIN diodes (1~6) are turned on are shown in Fig. 20(c). As shown in Fig. 20, there is clearly an independent controllability of each passband of the dual-band BPF in Fig. 19.

Table 2. Performance of the reconfigurable dual-band BPF.

Results of the BPF in Fig. 19	PIN diodes (1~6) off		PIN diodes (1~4) on		PIN diodes (5~6) on		PIN diodes (1~6) on	
	1st Pass-band	2nd Pass-band	1st Pass-band	2nd Pass-band	1st Pass-band	2nd Pass-band	1st Pass-band	2nd Pass-band
3-dB FBW	5.8 %	3.8 %	6.3 %	1.9 %	7 %	4.7 %	8 %	2.2 %
Center freq.	2.17 GHz	5.11 GHz	2.18 GHz	5.43 GHz	2.61 GHz	5.12 GHz	2.64 GHz	5.43 GHz
Insertion loss	0.77 dB	0.85 dB	0.7 dB	1.48 dB	0.47 dB	1.08 dB	0.4 dB	1.45 dB
Return loss	22 dB	17 dB	22.99 dB	24.21 dB	27.64 dB	10.4 dB	29.5 dB	14.9 dB

Table 2 shows the performance of the proposed reconfigurable dual-band BPF. By comparing the case where all the PIN diodes are turned on and the case where all the PIN

diodes are turned off, the center frequency of the first passband is shifted from 2.17 GHz to 2.64 GHz, and the center frequency of the second passband is shifted from 5.11 GHz to 5.43 GHz. The frequency variation range of two passbands is determined by g_2, w_2, w_4, and the widths of lines (1, 2, and 3). Thus, two discrete states of each passband can be determined by properly selecting g_2, w_2, w_4, and the widths of lines (1, 2, and 3) according to the applications.

II.7. Conclusion

Novel single- and dual-band BPFs with suppressed harmonic responses have been developed by using stepped impedance stubs. The single-band BPF is designed by analyzing the even and odd mode resonant frequencies and transmission zeros. The S-shaped coupled feed lines are used to excite the resonator of the single-band BPF. The transmission zeros produced by the S-shaped feed lines are used to suppress the harmonic responses as well as to improve the attenuation characteristic of the upper passband edge. A dual-band operation is introduced by placing a strip line between two stepped impedance stubs. The frequency characteristic of the dual-band resonator is studied by the even and odd mode analysis method. The S-shaped feed lines are used to excite the dual-band resonator, and then the harmonic responses are suppressed, resulting in a wide stopband. It is verified that the S-shaped coupled feed lines can be used to achieve a wide stopband for a dual-band BPF as well as a single-band BPF. It is also shown that the dual-band BPF exhibits the independent tunability of two passbands by changing the parameters of the dual-band resonator. The reconfigurable dual-band BPF is designed by

using PIN diodes to make four discrete states of two passbands, and the frequency characteristics of each state are studied.

CHAPTER III

ULTRA-WIDEBAND (UWB) BANDPASS FILTER USING A SYMMETRIC STEPPED IMPEDANCE RESONATOR WITH AN ASYMMETRIC STEPPED IMPEDANCE STUB

III.1. Introduction

As high data rate communications become more and more important, the wideband and ultra-wideband (UWB) wireless communications technology has been gaining a lot of attention after the permission of the unlicensed use of the UWB frequency band (3.1 GHz to 10.6 GHz) by the Federal Communications Commission (FCC) [25]. In UWB technology, UWB bandpass filters (BPFs) are one of the most important components in UWB wireless communication systems. The UWB BPFs with a low insertion loss, a large return loss within a passband, and a sharp selectivity at both sides of a passband play a key part in realizing UWB technology. Recently, there have been many studies on various types of UWB BPFs to meet those essential demands. Since the concept of multiple mode resonator (MMR) was introduced in [26], many UWB BPFs using MMR have been proposed. A folded multiple-mode resonator [27] and a stub-loaded multiple-mode resonator [28] were used to design an UWB BPF. UWB BPFs using broadside coupling have been proposed. Five capacitive loaded transmission line resonators are alternatively etched on the top and middle layers of the UWB BPF [29], and two elliptical-shaped microstrip patches at the top and bottom layers are coupled via an elliptical slot at the mid layer of the structure [30].

Recently, the increasing demand to avoid interference with existing wireless networks, such as WLAN and Wi-Max led to develop UWB BPFs with a notched band. A notched band was introduced by embedding two open-circuited stubs in the UWB BPF consisting of five short-circuited stubs [31], and the UWB BPF with a notched band was presented by lengthening and folding one of two coupling arms [32]. An asymmetric structure of the interdigital-coupled feed lines [33] and ring defected ground structures (DGSs) [34] were used to create a notch-band.

In this chapter, UWB BPFs with and without a notched band are developed using a symmetric stepped impedance resonator with an asymmetric stepped impedance stub at the center of the resonator. The even and odd mode resonant frequencies for the resonator are analyzed from the equivalent circuits, and Y matrix converted from ABCD matrix is used to calculate the transmission zeros. The parameters of the resonator are determined by considering wide bandwidth and symmetry passband. The rectangular slots on the ground under the interdigital coupled feed lines are designed to achieve improved return loss over a wide range of operating frequency band. Asymmetric feed lines are used to introduce a notched band to avoid signal interferences at 6 GHz band. The performances in time-domain as well as frequency-domain are analyzed and discussed. A Gaussian modulated pulse is used to transmit through the proposed UWB BPFs. The proposed BPFs are designed on an RT/Duroid 6006 substrate with a thickness of 0.635 mm and a relative dielectric constant of 6.15. Electromagnetic (EM) simulations in this chapter are performed by Zeland IE3D based on method of moments.

III.2. Analysis of the symmetric stepped impedance resonator with an asymmetric stepped impedance stub

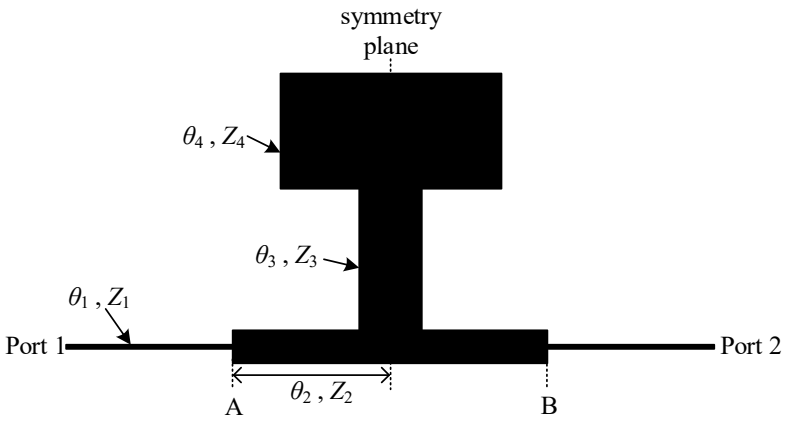

Fig. 21. Symmetric stepped impedance resonator with an asymmetric stepped impedance stub.

Fig. 21 shows the configuration of a symmetric stepped impedance resonator with an asymmetric stepped impedance stub at the center of the resonator. The open circuited stepped impedance resonator, which is either symmetric or asymmetric, consists of the two lines with different electrical lengths and characteristic impedances. Z_1 and Z_2 are the characteristic impedances of the symmetric stepped impedance line, while θ_1 and θ_2 are the electrical lengths as shown in Fig. 21. Z_3 and Z_4 are the characteristic impedances of the asymmetric stepped impedance stub of the resonator, while θ_3 and θ_4 are the electrical length. Because the resonator is symmetric with respect to the symmetry plane, the even and odd mode analysis method is applied in the resonator. The even and odd modes represent the whole frequency response of the resonator because the even and odd modes are orthogonal to each other and are collectively exclusive.

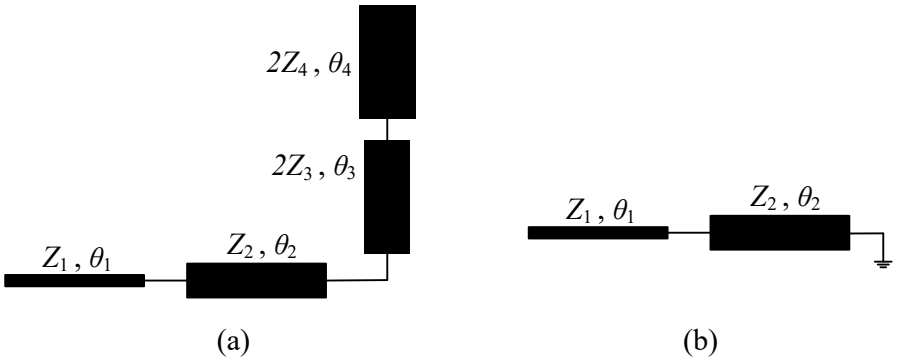

Fig. 22. Equivalent circuits for symmetric stepped impedance resonator with an asymmetric stepped impedance stub in Fig. 21. (a) even mode. (b) odd mode.

The even and odd mode distributed equivalent circuits in Fig. 22 are used to calculate the even and odd mode resonant frequencies, respectively. For the even mode, four strip lines with different electrical lengths and characteristic impedances are connected in cascade as shown in Fig. 22(a), where the characteristic impedances of the asymmetric stepped impedance stub are doubled because the stub is divided in half with respect to the symmetry plane. In Fig. 22(b), the odd mode equivalent circuit becomes a short-circuited strip line, which consists of two sections with different electrical lengths and characteristic impedances. The even and odd mode resonant frequencies of the resonator can be calculated under the condition of Y_{in}=0, and are derived as follows:

$$Y_{in}^{e} = \frac{\tan\theta_1 - K_1 \cdot M}{1 + K_1 \cdot M \cdot \tan\theta_1} = 0 \qquad \text{for even modes (17)}$$

where

$$M = \left\{ \frac{2K_2K_3 \tan\theta_2 + K_3 \tan\theta_3 + K_2 \tan\theta_4 - 2K_2^2 \tan\theta_2 \tan\theta_3 \tan\theta_4}{K_3 \tan\theta_2 \tan\theta_3 + K_2 \tan\theta_2 \tan\theta_4 + 2K_2^2 \tan\theta_3 \tan\theta_4 - 2K_2K_3} \right\}$$

and

$$Y_{in}^{o} = \frac{K_1 - \tan\theta_1 \tan\theta_2}{\tan\theta_2 + K_1 \tan\theta_1} = 0 \qquad \text{for odd modes (18)}$$

where $K_1=Z_1/Z_2$, $K_2= Z_3/Z_2$, and $K_3= Z_4/Z_2$

To investigate the transmission zeros of the resonator, the ABCD matrix of the resonator in Fig. 21 is calculated, and then the ABCD matrix is transformed to the admittance matrix. The transmission zeros of the resonator can be obtained under the condition of $Y_{21}=0$, which is calculated as follows:

$$Y_{21} = \left\{ \cos\theta_2 - \frac{\sin\theta_2 \left(K_2 \tan\theta_4 + K_3 \tan\theta_3 \right)}{2K_2 \left(K_3 - K_2 \tan\theta_3 \tan\theta_4 \right)} \right\}^{-1} = 0 \qquad (19)$$

It is noticeable that the transmission zeros have nothing to do with the electrical length of θ_1 and the characteristic impedance of Z_1. This is because the signal cannot pass through from port 1 to port 2 when the circuit between A and B in Fig. 21 is open-circuited at certain frequencies. In other words, the transmission zeros of the resonator in Fig. 21 are the same as the transmission zeros of the circuit between A and B.

Fig. 23(a) and (b) plot the first three even mode and the first two odd mode resonant frequencies and the first two transmission zeros normalized by π/2 against θ_1/θ_2 and K_1, respectively. In Fig. 23(a), K_1, K_2, and K_3 are fixed to be 2.86, 0.64, and 0.22, respectively, while θ_3/θ_2 and θ_4/θ_2 are set to be 1.05 and 0.8, respectively. In Fig. 23(b), θ_1/θ_2, θ_3/θ_2, and θ_4/θ_2 are set to be 0.92, 1.05, and 0.8, respectively, while K_2 and K_3 are fixed to be 0.64 and 0.22, respectively. The first three even mode and the first two odd mode resonant frequencies are used to make a passband, while the first two transmission zeros are placed on both sides of the passband to make sharp attenuation slopes. The passband bandwidth

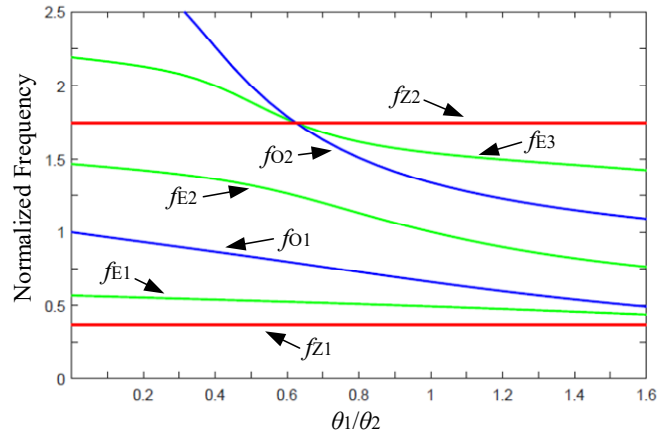

(a)

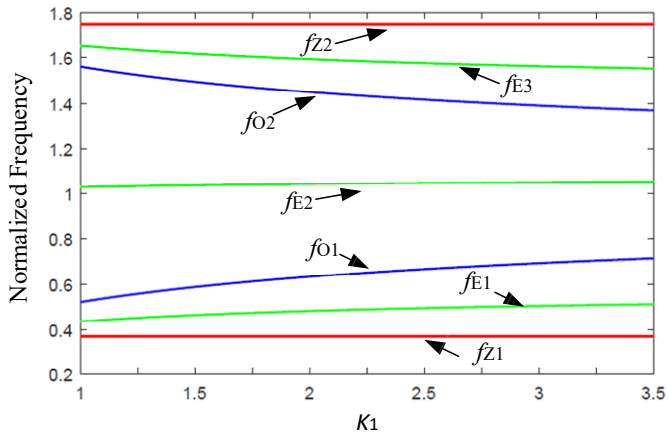

(b)

Fig. 23. Resonant frequencies (f_E: even mode, f_O: odd mode) and transmission zeros (f_Z) normalized by $\pi/2$ for the resonator in Fig. 21 with respect to (a) θ_1/θ_2 when θ_3/θ_2=1.05, θ_4/θ_2=0.8, K_1=2.86, K_2=0.64, K_3=0.22 and (b) K_1 when θ_1/θ_2=0.92, θ_3/θ_2=1.05, θ_4/θ_2=0.8, K_2=0.64, K_3=0.22.

can be estimated by the difference between the first and the third even mode resonant frequencies (f_{E3} - f_{E1}). θ_1/θ_2 should be greater than 0.62 in order to include the first three even mode and the first two odd mode resonant frequencies within the passband as shown in Fig. 23(a). In addition, the symmetric passband can be achieved when f_{E1} - f_{Z1} is the same as f_{Z2} - f_{E3}. As θ_1/θ_2 increases, the value of f_{Z2} - f_{E3} becomes bigger than the value of

f_{E1} - f_{Z1}, causing an asymmetric passband. Thus, θ_1/θ_2 is selected to be 0.92 so that the passband becomes symmetric as shown in Fig. 23(a). Besides, Z_1 is selected so that the first three even mode and the first two odd mode resonant frequencies are spread out within the passband as evenly as possible. As K_1 increases, the resonant frequencies are gradually spread out between two transmission zeros as shown in Fig. 23(b). However, the value of K_1 is limited by the circuit fabrication; therefore, K_1 is chosen to be 2.87.

Figs. 24 shows the first three even mode and the first two odd mode resonant frequencies and the first two transmission zeros normalized by π/2 against θ_3/θ_2 and θ_4/θ_2 for the left-hand figures and the right-hand figures, respectively, with different values of

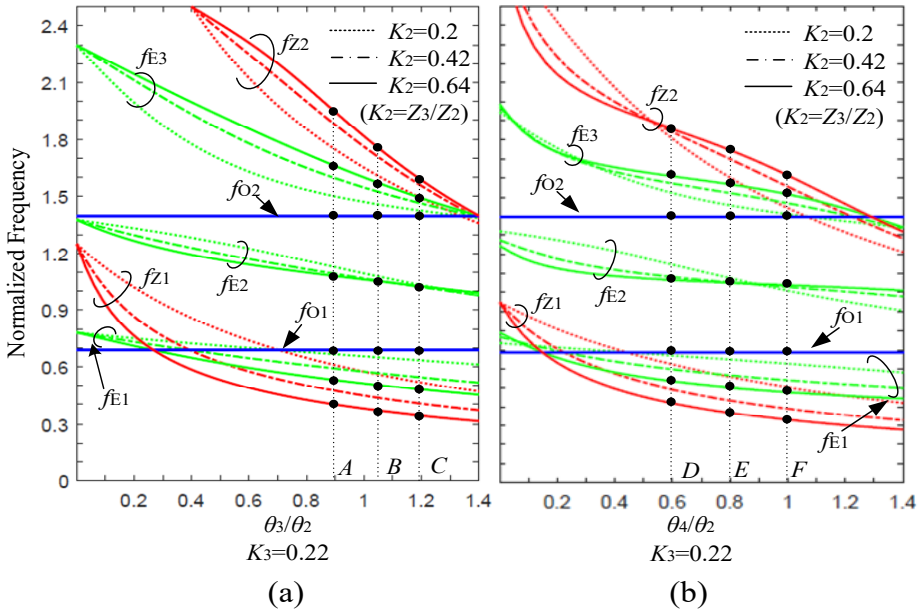

Fig. 24. Resonant frequencies (f_E: even mode, f_O: odd mode) and transmission zeros (f_Z) normalized by $\pi/2$ with respect to (a) θ_3/θ_2 (K_1=2.87, K_3=0.22, θ_1/θ_2=0.92, and θ_4/θ_2=0.8), (b) θ_4/θ_2 (K_1=2.87, K_3=0.22, θ_1/θ_2=0.92, and θ_3/θ_2=1.05), (c) θ_3/θ_2 (K_1=2.87, K_2=0.64, θ_1/θ_2=0.92, and θ_4/θ_2=0.8), and (d) θ_4/θ_2 when K_1=2.87, K_2=0.64, θ_1/θ_2=0.92, θ_3/θ_2=1.05.

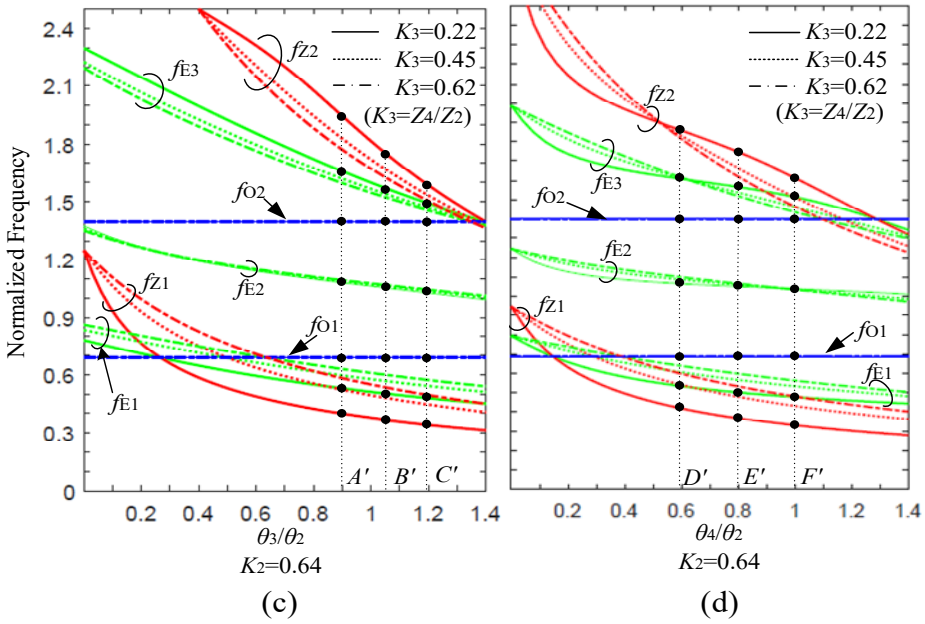

Fig. 24 Continued.

K_2 and K_3. For each figure in Fig. 24, θ_1/θ_2 and K_1 are fixed at 0.92 and 2.87, respectively, for the symmetric passband as analyzed in Figs. 23(a) and (b). Figs. 24(a) and (b) are for K_3 =0.22, and Figs. 24(c) and (d) are for K_2=0.64. Also, for the left-hand figures in Figs. 24, θ_4/θ_2 is fixed at 0.8, while θ_3/θ_2 is fixed at 1.05 for the right-hand figures. In Figs. 24, it is noticeable that the first two odd mode resonant frequencies of the resonator are constant regardless of K_2, K_3, $\theta_3/\theta_2$and θ_4/θ_2. This is because the asymmetric stepped impedance stub is unrelated to the odd mode resonant frequencies. In Figs. 24(a) and (b), for θ_4/θ_2 larger than 0.28 in Fig. 24(b), it is found that the passband bandwidth (f_{E3} - f_{E1}) broadens out as K_2 increases. In Figs. 24(c) and (d), for θ_4/θ_2 larger than about 0.64 in Fig. 24(d), it is also observed that the passband bandwidth (f_{E3} - f_{E1}) widens out as K_3 decreases. Therefore, the passband bandwidth of the resonator in Fig. 21 can be increased by using a

larger K_2 and a smaller K_3. Based on the analyzed results, K_2 and K_3 are selected to be 0.64 and 0.22 to realize the UWB passband bandwidth (3.1 GHz to 10.6 GHz).

To determine θ_3/θ_2 and θ_4/θ_2, the passband symmetry of the resonator needs to be considered. For θ_3/θ_2=0.9, 1.05, and 1.2, which are denoted by A, A', B, B', C, and C' in Figs. 24(a) and (c), the value of $f_{Z2} - f_{E3}$ at A or A' is bigger than the value of $f_{E1} - f_{Z1}$, causing an asymmetric passband. Also, the value of $f_{E1} - f_{Z1}$ at C or C' is bigger than the value of $f_{Z2} - f_{E3}$, causing an asymmetric passband. At B or B', the value of $f_{E1} - f_{Z1}$ is almost the same as the value of $f_{Z2} - f_{E3}$, causing a symmetric passband, thus B or B' is selected for the passband symmetry. Similarly, for θ_4/θ_2=0.6, 0.8, and 1.0, which are denoted by D, D', E, E', F, and F' in Figs. (b) and (d), the value of $f_{Z2} - f_{E3}$ at D or D' is bigger than the value of $f_{E1} - f_{Z1}$, causing an asymmetric passband. Also, the value of $f_{E1} - f_{Z1}$ at F or F' is bigger than the value of $f_{Z2} - f_{E3}$, causing an asymmetric passband. At E or E', the value of $f_{E1} - f_{Z1}$ is almost the same as the value of $f_{Z2} - f_{E3}$, causing a symmetric passband, thus E or E' is selected for the passband symmetry. Based on the analyzed results, θ_3/θ_2 and θ_4/θ_2 are selected to be 1.05 and 0.8, respectively.

III.3. Design of the UWB BPF with interdigital feed lines

Fig. 25 shows the configuration of the bandpass filter using a symmetric stepped impedance resonator with an asymmetric stepped impedance stub fed by interdigital coupled feed lines. The physical line widths (w_1, w_5) and the slot width (g_1) are determined by EM simulations for the better passband characteristics. The rectangular slots on the

ground plane are used to increase couplings between the resonator and the interdigital feed lines as shown in Fig 25.

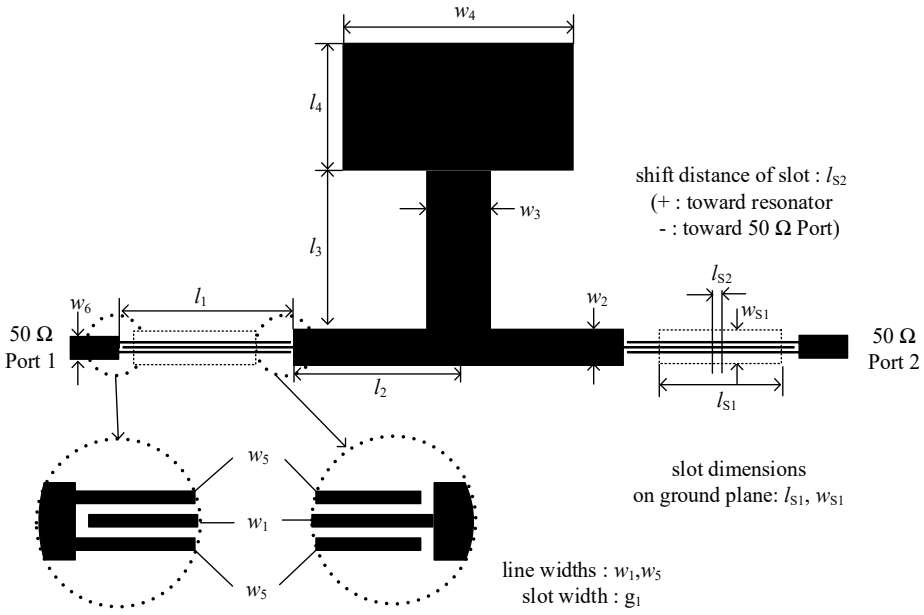

Fig. 25. Proposed UWB bandpass filter with the resonator in Fig. 21 fed by interdigital coupled feed lines with rectangular slots on the ground. (l_1=5.8 mm, l_2=5.39 mm, l_3=4.87 mm, l_4=3.9 mm, l_{S1}=5 mm, l_{S2}=−0.1 mm, w_1=0.1 mm, w_2=1.41 mm, w_3=2.1 mm, w_4=9.7 mm, w_5=0.1 mm, w_{S1}=1.15 mm, and g_1=0.1 mm)

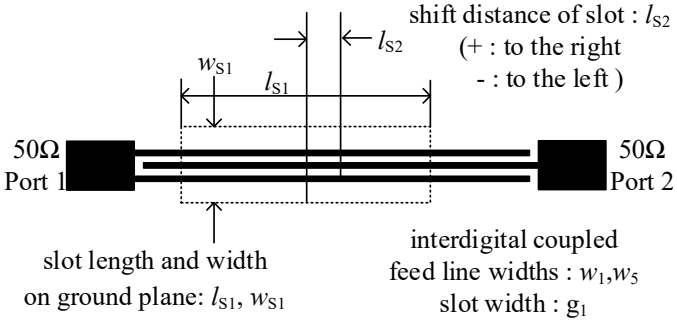

Fig. 26. Interdigital coupled feed line with rectangular slot on the ground.

To investigate the frequency characteristic of the interdigital coupled feed line with the rectangular slot on the ground, only the interdigital feed line is used to simulate as shown in Fig.26. In Fig. 26, the length and width of the rectangular slot are denoted by l_{S1} and w_{S1}, respectively. The magnitude of l_{S2} indicates the distance between the center of the feed line and the center of the rectangular slot. The sign of l_{S2} represents the shifted direction of the rectangular slot. The plus sign (+) indicates when the rectangular slot moves toward the port 2, while the minus sign (−) indicates when the rectangular slot moves toward the port 1.

Figs. 27 (a), (b), and (c) show the simulated frequency responses of the interdigital feed line with a rectangular slot in Fig. 26 according to the variations of $w_{S1,}$ l_{S1}, and l_{S2}, respectively. The simulated results of the UWB BPF without the rectangular slots in Fig.

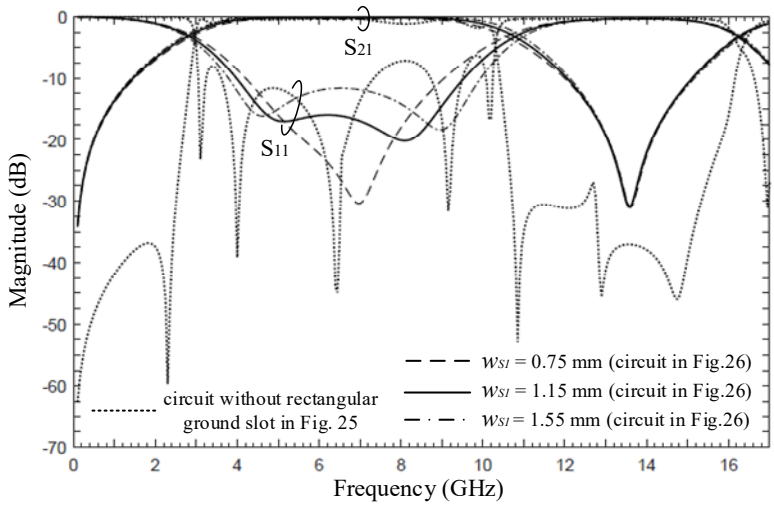

(a)

Fig. 27. Simulated frequency responses of interdigital coupled feed lines in Fig. 26 according to variations of (a) w_{S1}, (b) l_{S1}, and (c) l_{S2}. Dot line represents UWB BPF in Fig. 25 without rectangular slots on the ground for comparison.

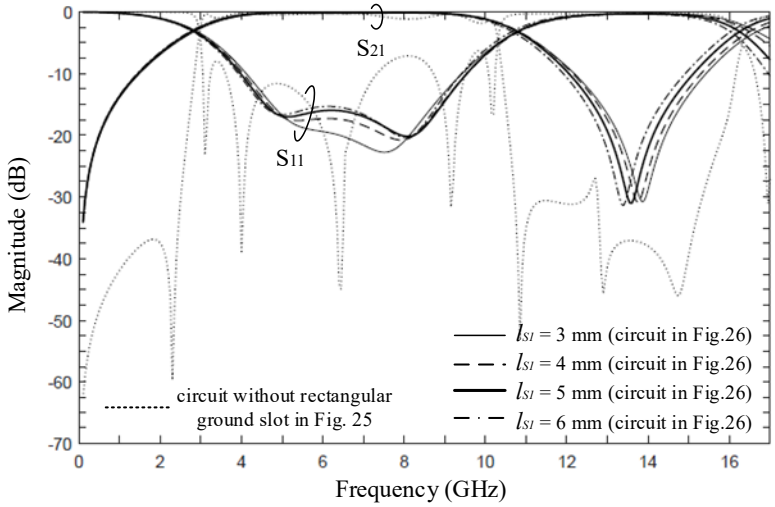

(b)

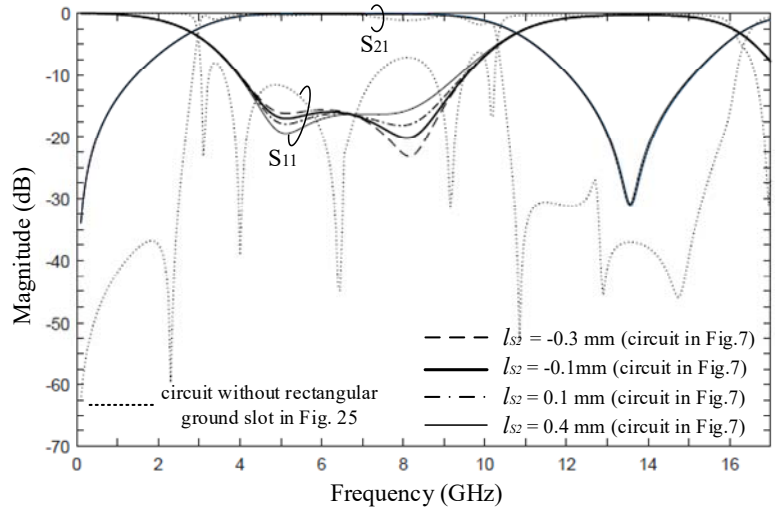

(c)

Fig. 27 Continued.

25 are compared in each figure in Fig. 27. For this simulation of the UWB BPF without the rectangular slot on the ground, the analyzed results in Fig. 23 and Fig. 24 are used as follows: θ_1/θ_2 =0.92, θ_3/θ_2=1.05, θ_4/θ_2 =0.8, K_1=2.87, K_2=0.77, and K_3=0.22 at the center frequency of 6.7GHz. The physical dimensions for these values are as follows: l_1=5.8 mm, l_2=5.39 mm, l_3=4.87 mm, l_4=3.9 mm, w_1=0.1 mm, w_2=1.41 mm, w_3=2.1 mm, and w_4=9.7

mm. In Fig. 27(a), l_{S1} and l_{S2} are set to be 5 mm and −0.1 mm, respectively, where −0.1 mm means the rectangular slots on the ground are shifted to the ports by 0.1 mm. It is found that as the width of the rectangular slots increases, the gap between the mid-lower and the mid-upper resonant frequencies of the passband widens. As a result, the return losses within the mid-lower and the mid-upper passbands are improved, while the return loss within the mid passband becomes worse, as shown in Fig. 27(a). In Fig. 27(b), w_{S1} and l_{S2} are fixed at 1.15 mm and −0.1 mm, respectively. It is noticeable that as the length of the rectangular slots becomes longer from 3 mm to 6 mm, the transmission zero at about 13.5 GHz tends to move to the lower frequency, and the return loss within the mid-lower and the mid-upper passbands is slightly improved. In Fig. 27(c), l_{S1} and w_{S1} are set to be 5 mm and 1.15 mm, respectively.

As the rectangular slot moves toward the port 1 in Fig. 26, the return loss within the mid-upper passband is improved, while the return loss within the mid-lower passband becomes worse. On the contrary, as the rectangular slot moves toward the port 2 in Fig. 26, the return loss within the mid-lower passband is improved, while the return loss within the mid-upper passband becomes worse. The effect of the rectangular slot can be displayed when the resonator and the feed lines with the rectangular slot are used together as shown in Fig. 25.

Fig. 28 shows the simulated frequency responses when the resonator and the feed lines with the rectangular slots are used together, as shown in Fig. 25, with different shifted distances (l_{S2}) of the rectangular slots. The plus sign (+) indicates when the rectangular slots move toward the center of the resonator in Fig. 25, while the minus sign (−) indicates

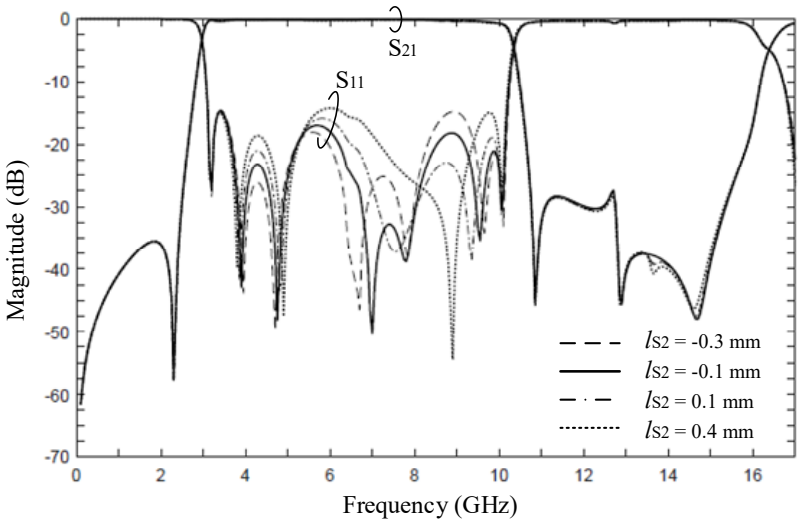

Fig. 28. Simulated frequency responses of UWB BPF in Fig. 25 with different shifted distances of rectangular slots on the ground.

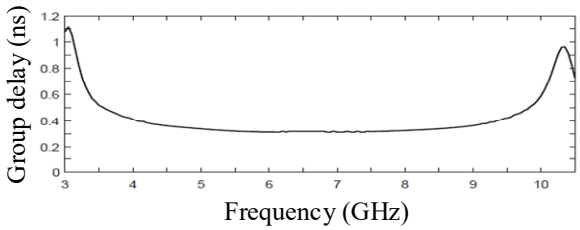

Fig. 29. Group delay for UWB BPF in Fig. 25.

when the rectangular slots move toward each port. For this simulation of the UWB BPF with the rectangular slots on the ground, the results in Fig. 25 except l_{S2} are used as follows: l_1=5.8 mm, l_2=5.39 mm, l_3=4.87 mm, l_4=3.9 mm, l_{S1}=5 mm, w_1=0.1 mm, w_2=1.41 mm, w_3=2.1 mm, w_4=9.7 mm, w_5=0.1 mm, w_{S1}=1.15 mm, and g_1=0.1 mm. It is found that the return loss within the passband is significantly improved and the total number of resonant frequencies is increased from 5 to 7, compared to the BPF without the rectangular slot, as shown in Fig. 27. If the rectangular slot moves toward the center of the resonator,

the return loss within the mid-upper passband is improved, while the return loss within the mid-lower passband becomes worse, as analyzed in Fig. 27(c). Among the results from four values of l_{S2} in Fig. 28, −0.1 mm is chosen to obtain a better return loss and a lower insertion loss within the passband, where −0.1 mm means that the rectangular slots move toward each port by 0.1 mm. The UWB BPF in Fig. 25 provides a 3-dB bandwidth from 3 GHz to 10.3 GHz and a fractional bandwidth (FBW) of about 110 %. The results show that the insertion loss at the center frequency is 0.12 dB and the return loss within the passband is greater than 15 dB. Fig. 29 shows the simulated results of the group delay variation within the passband. The group delay rapidly changes at both edges of the passband, but it is quite flat over the passband with about 0.3 ns.

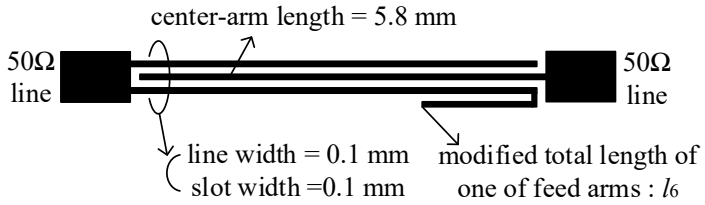

Fig. 30. Modified interdigital coupled feed lines for a notched band.

III.4. UWB bandpass filter with a notched band

To avoid interferences with WLAN signals, it is necessary to introduce a notch characteristic within the UWB passband. The interdigital coupled feed lines are modified to have an asymmetric structure in order to introduce a notched band as shown in Fig. 30. The length difference between two arms of the interdigital coupled feed lines leads to the

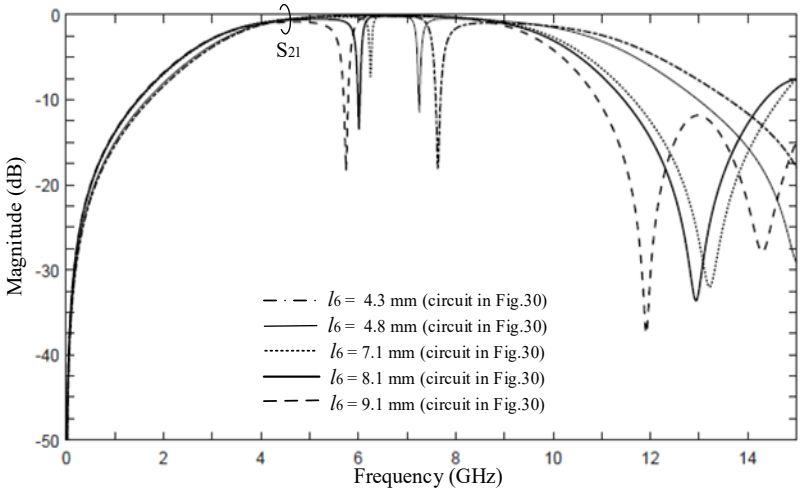

Fig. 31. Simulated frequency responses of the modified interdigital coupled feed lines in Fig. 30 with varying l_6.

phases difference of the signals, resulting in the rejection of the signal at a certain frequency.

Fig. 31 shows the simulated results of the modified interdigital coupled feed line in Fig. 30 according to the variations of l_6. As the length of the extended arm of the interdigital coupled feed lines becomes longer, from 4.3 mm to 9.1 mm, the notched bands can be obtained at 7.6 GHz, 7.2 GHz, 6.2 GHz, 6 GHz, and 5.7 GHz, sequentially. When the asymmetric feed lines as in Fig. 30 excite the resonator in Fig. 21, a notched band is introduced but the return loss within the passband also varies because the couplings between the resonator and the feed lines are changed. To obtain a better return loss in the passband, the dimensions and the shifted distance of the rectangular slot on the ground need to be adjusted based on the analyzed results in Fig. 27.

Fig. 32 shows the configuration of the UWB BPF with a notch band at 6 GHz using the asymmetric feed lines in Fig. 30. Except l_{S1}, l_{S2}, and w_{S1}, the dimensions in Fig. 25 are

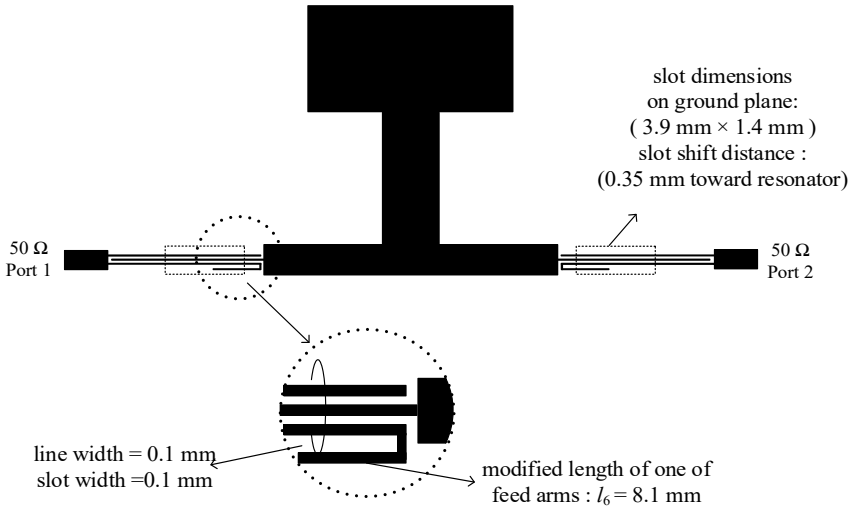

Fig. 32. Proposed UWB bandpass filter with a notch band.

used in Fig. 32. For a better return loss, the dimension of the rectangular slot is chosen to be 3.9 mm by 1.4 mm, and the rectangular slot moves toward the center of the resonator by 0.35 mm by the EM simulations. The length of the extended arm of the interdigital coupled feed lines is chosen to be 8.1 mm to introduce a notched band at 6 GHz.

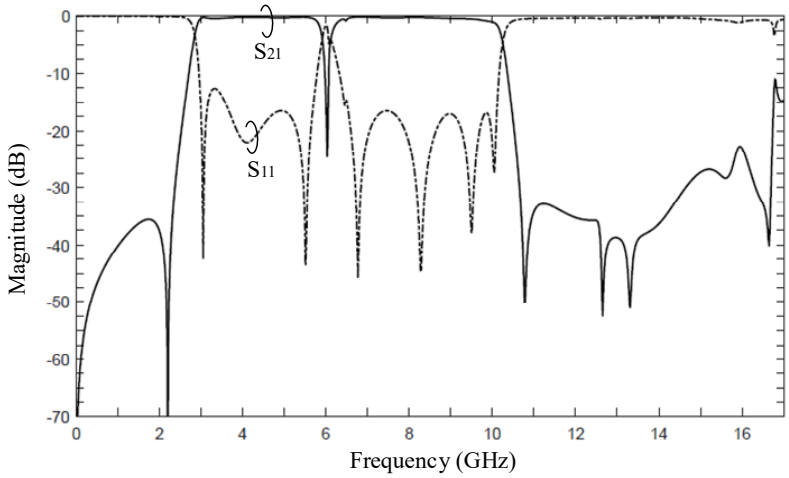

Fig. 33. Simulated frequency responses of UWB bandpass filter with a notched band in Fig. 32.

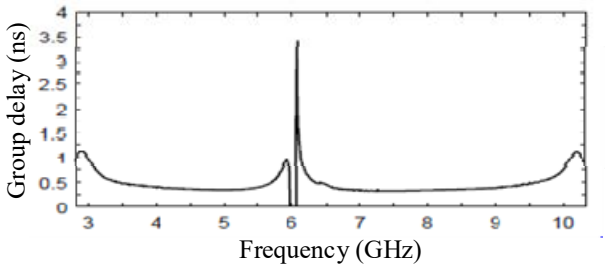

Fig. 34. Group delay for UWB BPF with a notched band in Fig. 32.

The simulated frequency responses and group delay variation of the UWB BPF in Fig. 32 are shown in Fig. 33 and Fig. 34, respectively. The notched band is observed at 6 GHz with the rejection level of 25 dB and the FBW is about 4.3 %. The group delay is flat with about 0.3 ns within the passband except for the region around the notch band but it is increased up to 3.3 ns at the center frequency of the notched band. Generally speaking, the group delay variation increases in quickly changing frequency bands such as the notched band and the edge of the passband.

III.5. Time-domain analysis of UWB BPFs

To investigate the time-domain performance, simulations of the time-domain response are carried out. Figs. 35(a) and (b) show the waveforms of the transmitted and received signals in time-domain before and after filtering with the UWB BPFs in Fig. 25 and Fig. 32, respectively. As a test signal to examine the signal characteristics in time-domain, a unity-amplitude Gaussian RF pulse with a center frequency of 5GHz and a FBW of 30 % is transmitted to port 1 of the UWB BPFs in Fig. 25 and Fig. 32. In Figs. 35(a) and (b), the delay time between the transmitted and received signals is about 0.3 ns, which

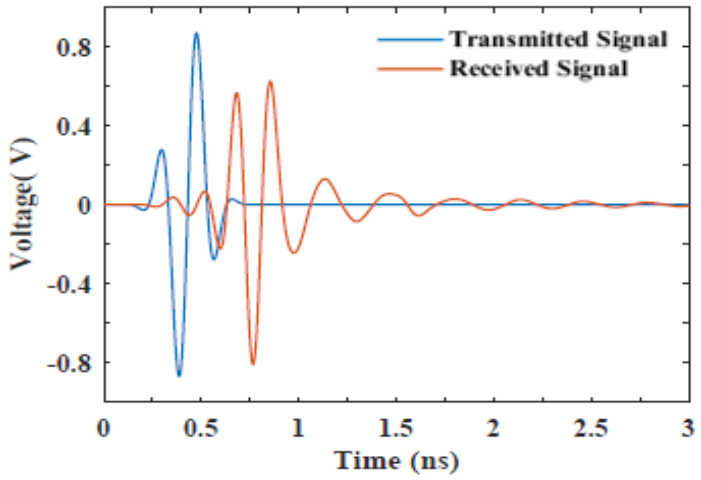

(a)

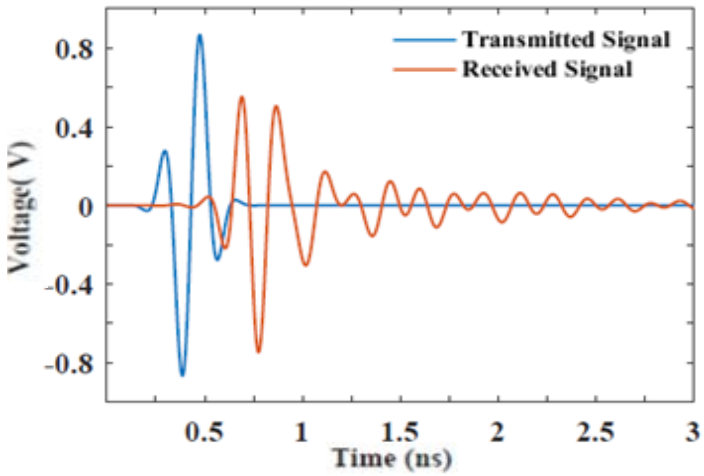

(b)

Fig. 35. Waveforms of the transmitted and received signals of the BPF (a) without and (b) with a notched band in time-domain.

is the same as the group delay discussed in Fig. 29 and Fig 34. In addition, it can be observed that the received signals at port 2 resemble the derivative of the transmitted signal at port 1 with respect to time. In other words, the waveforms of signals passing through the filters, which are either with or without a notched band, become similar to the inverted derivative of the transmitted signals with respect to time. An analogous

phenomenon is observed in UWB antennas. The signal received from the receiving antenna has a waveform of the time derivative of the originally transmitted signal [35]. However, the received waveform has a slight distortion and a ringing effect because of the band-limited signal. It is preferable to minimize the distortion and ringing effect, but this is inevitable in reality. Comparing Figs. 35(a) with (b), the received signal of the UWB BPF with a notched band has a slightly lower maximum and a larger ringing effect than the received signal of the UWB BPF without a notched band. This is because the energy in the main lobes of the signal transmitted through the UWB BPF with a notched band more easily leaks into the ringing effect than the energy in the main lobes of the signal transmitted through the UWB BPF without a notched band, causing the distortion of the signal waveform.

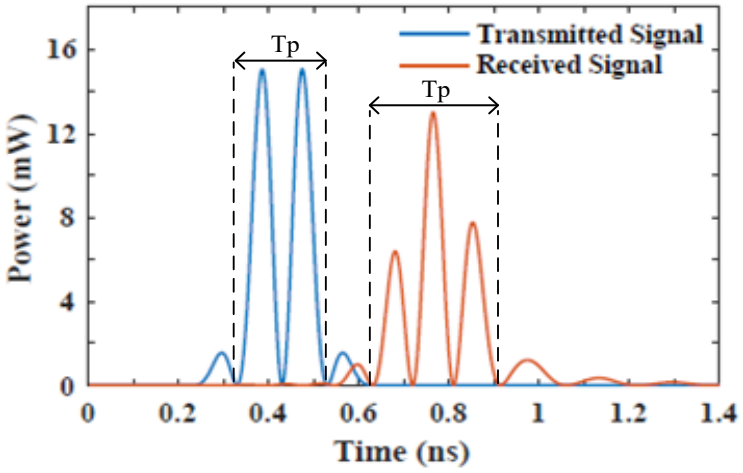

(a)

Fig. 36. Power of the transmitted and received signals of the UWB BPF (a) without and (b) with a notched band.

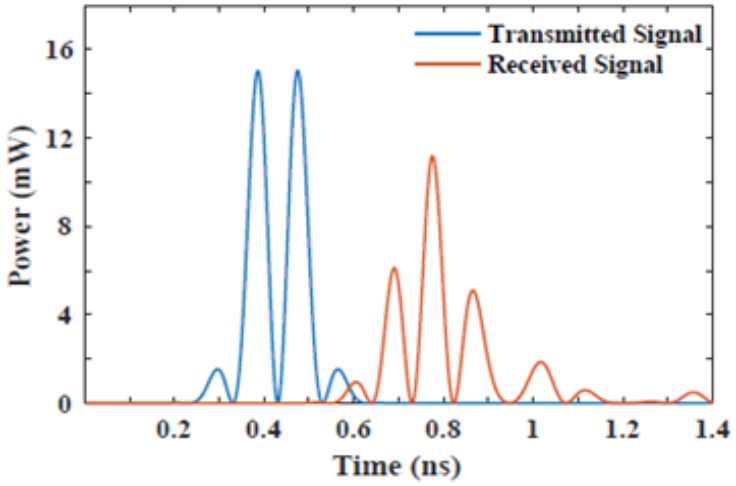

(b)

Fig. 36 Continued.

To investigate the extent of the signal distortion, the powers of the transmitted and received signals of the UWB BPFs in Fig. 25 and Fig. 32 are calculated in Figs. 36(a) and (b), respectively. Here, the Gaussian pulse width (T_p) of the received signal with ringing effect is defined as the summation of the widths of the main lobes of the pulse signal as in Fig. 36. As the energy of the received signal is more concentrated within the main lobes, the signal distortion, due to the ringing effect, decreases. The pulse width of the transmitted signal is 0.2 ns, in which 91.34 % of the pulse energy is contained. The energy within the pulse width is calculated by integrating the signal power with respect to time. However, considering the effect of the time derivative of filtering, the pulse width of the received signal is compared to the pulse width of the time derivative of the transmitted signal. The pulse width of the time derivative of the transmitted signal is about 0.27 ns. In Fig. 36(a), the pulse width of the received signal is 0.28 ns, in which 86.82 % of the pulse energy is contained, while in Fig. 36(b), the pulse width of the received signal is 0.31 ns

with 79.16 % of the pulse energy contained. A comparison of the two results reveals that the pulse width of the received signal of the UWB BPF with a notched band in Fig. 32 is slightly bigger than the pulse width of the received signal of the UWB BPF without a notched band in Fig. 25. However, comparing the pulse widths of the received signals with the pulse width of the derivative of the transmitted signal, the distortions of the pulse widths of the received signals of the UWB BPFs with and without a notched band are negligible.

Figs. 37(a) and (b) show the frequency spectrum of the signals transmitted and received through the UWB BPFs in Fig. 25 and Fig. 32, respectively. The transmitted signal is the same as in Fig. 35. The maximum of the spectrum appears at 5 GHz because the transmitted signal is modulated by a Gaussian pulse with the center frequency of 5

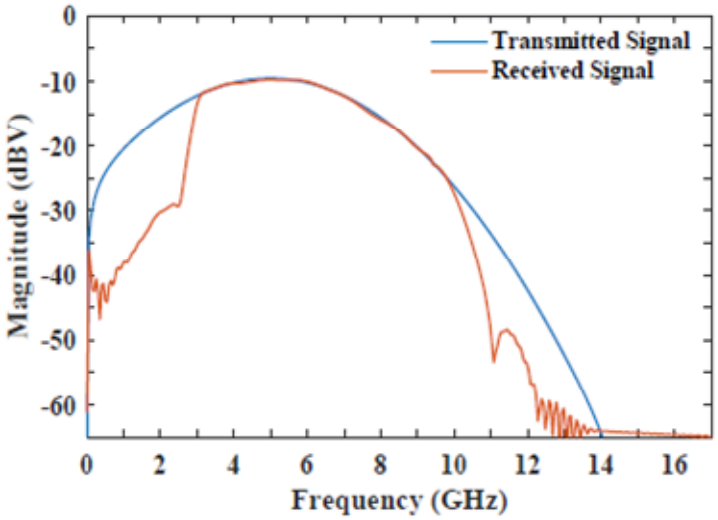

(a)

Fig. 37. Frequency spectrum of the transmitted and received signals of the BPF (a) without and (b) with a notched band.

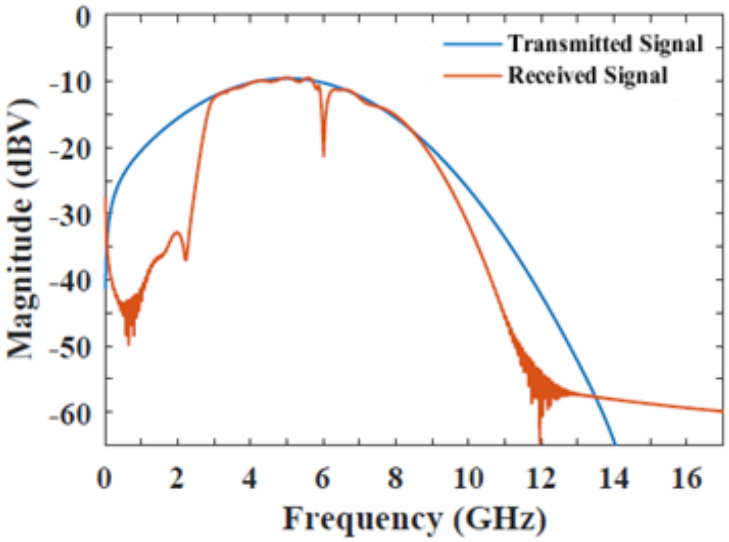

(b)

Fig. 37 Continued.

GHz. In Fig. 37(a), the frequency spectrum of the received signal at port 2 in Fig. 25 is almost the same as the frequency spectrum of the transmitted signal within the frequency band (3 GHz to 10.3 GHz), which is the passband of the proposed UWB BPF in Fig. 25. The comparison reveals that the proposed UWB filter without a notched band allows the frequency elements within the passband and blocks the frequency elements out of the passband as shown in Fig. 28. In the case of UWB BPF with a notched band in Fig. 37(b), it can be observed that there is a notched band at 6 GHz. However, the characteristic of the upper band edge frequency of the received signal is slightly lower than the characteristic of the UWB BPF without a notched band, as shown in Fig. 37(b). This is because the energy of high frequency elements of the signal transmitted through the UWB BPF with a notched band in Fig. 32 more easily leaks in ringing effect. The time-domain performance is summarized in Table 3. Based on the time-domain analysis, it is shown

that the UWB BPF in Fig. 25 exhibits satisfactory performances in the time- and frequency-domains. However, the UWB BPF in Fig. 32 has satisfactory performances in the frequency-domain but a slight distortion for the frequency elements higher than about 9.5 GHz.

Table 3. Time-domain analysis results of Fig. 25 and Fig. 32.

Time-domain analysis	Transmitted signal	Derivative of transmitted signal	UWB BPF without a notched band	UWB BPF with a notched band
Delay time	-	-	0.33 ns	0.34 ns
Pulse width	0.2 ns	0.27 ns	0.28 ns	0.31 ns
Energy percentage within pulse width	91.34 %	96.7%	86.82 %	79.16%
3-dB bandwidth	-	-	2.96 GHz ~ 10.22 GHz	2.8 GHz ~ 9.5 GHz

III.6. Conclusion

UWB bandpass filters using a symmetric stepped impedance resonator with an asymmetric stepped impedance stub have been proposed. Analyzing resonant frequencies and transmission zeros leads to the design of the resonator. The interdigital coupled feed lines with rectangular slots on the ground are designed to obtain a better return loss and a passband symmetry. The UWB bandpass filter with a notched band is designed by using asymmetric feed lines. The notched band can be controlled by changing the length of one arm of interdigital feed lines. Except for a slight distortion at the upper edge of the passband of the UWB BPF with a notched band, the proposed UWB BPFs provide

satisfactory performances in both the time- and frequency-domains. Besides, the proposed UWB BPFs demonstrate advantages such as a low insertion loss within the passband, high attenuation slopes at both cutoff regions and a flat group delay within the passband.

CHAPTER IV

ULTRA-WIDEBAND BANDPASS FILTER WITH A SYMMETRIC STEPPED IMPEDANCE RESONATOR USING SHORT STUBS

IV.1. Introduction

Ultra-wideband (UWB) wireless communications have been attracting much attention with unique features, such as low power consumption, low cost, exceptional multi-path immunity, secure communication, and high data transmission rates. Since the Federal Communications Committee (FCC) allowed UWB frequency bandwidth (3.1 GHz to 10.6 GHz) to be used without permission in 2002, demand for UWB technology has greatly increased. UWB BPFs are one of the most essential components in UWB systems, and there have been rapidly growing research efforts on UWB BPFs. Coplanar waveguide (CPW) structures were used to design an UWB BPF [36]. The BPF has sharp selectivity but a decreased performance of the frequency response in the higher frequency. In [37], a composite structure of HPF and LPF was proposed. The structure size is reduced compared to the cascaded structure of HPF and LPF, but the transition band at the lower edge of the passband is not sharp enough. In addition, a UWB BPF using multi-stub-loaded ring resonator was proposed [38], and a composite right/left handed (CRLH) transmission line is used for an UWB BPF design [39]. In [40] and [41], an UWB BPF based on transversal signal interaction concepts was proposed.

The UWB systems have a high resistance from interference with other existing signals. This is because short pulses used in UWB systems have the low power spectral

density. However, to make sure to avoid even unintentional interference, there have been increasing demands for UWB BPFs with notched bands, and many techniques have been studied. Short-circuited stub resonators are integrated in a multilayer periodical structure to obtain multiple notch bands [42], and a meander line slot is used to make a notched band at 5.5 GHz band [43]. The notched bands operation was implemented by integrating stubs in broadside-coupled conductors [44] and by using radial stub loaded resonator (RSLR) [45].

In this chapter, a stepped impedance resonator and short stubs are used to design UWB BPFs with and without a notched characteristic. Even and odd mode resonant frequencies are analyzed by using even and odd mode equivalent circuits, respectively. The stepped impedance resonator is designed to obtain the UWB frequency bandwidth (3.1 GHz to 10.6 GHz), and the short stubs are developed to achieve the improved return loss over a wide range of operating frequency band and the sharp attenuation slopes at cut-off regions. A very narrow notched band at 5.8 GHz is created by adding stubs and slots into feed lines. The proposed BPFs are designed on an RT/Duroid 6006 substrate with a thickness of 0.635 mm and a relative dielectric constant of 6.15. Electromagnetic (EM) simulations in this chapter are performed by Zeland IE3D based on method of moments.

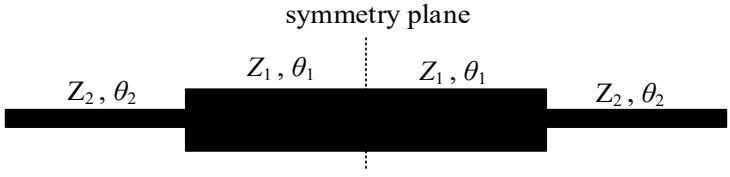

Fig. 38. Symmetric stepped impedance resonator.

IV.2. Analysis of a symmetric stepped impedance resonator

Fig. 38 shows the configuration of a symmetric stepped impedance resonator. The open circuited stepped impedance resonator consists of two parts with low and high characteristic impedances. In Fig. 38, Z_1 and θ_1 are the characteristic impedance and the electrical length for the line section in the middle, respectively. In addition, Z_2 and θ_2 are the characteristic impedance and the electrical length for the line sections at both sides, respectively. Because the resonator is symmetric with respect to the symmetry plane, the even and odd mode analysis method can be applied to the resonator in Fig. 38.

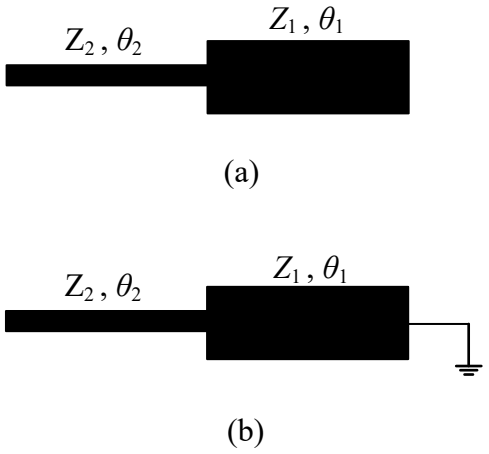

Fig. 39. Equivalent circuits for the resonator in Fig. 38. (a) even mode. (b) odd mode.

To calculate the even and odd mode resonant frequencies, even and odd mode distributed equivalent circuits are used as in Fig. 39(a) and (b), respectively. In Fig. 39(a), for the even mode, the resonator is divided with respect to the symmetry plane, and then an open circuit is placed at the symmetry plane, resulting in the equivalent circuit in Fig. 39(a). Similarly, for the odd mode, the resonator is divided with respect to the symmetry

plane, and then a short circuit is placed at the symmetry plane, resulting in the equivalent circuit in Fig. 39(b). The even and odd mode resonant frequencies of the resonator in Fig. 38 can be obtained under the condition of $Y_{in}=0$, where Y_{in} is the input admittance seen at the one end, and are derived as follows:

$$\frac{K\tan\theta_1+\tan\theta_2}{K\tan\theta_1\tan\theta_2-1}=0 \qquad \text{for even modes (20)}$$

and

$$\frac{K-\tan\theta_1\tan\theta_2}{\tan\theta_1+K\tan\theta_2}=0 \qquad \text{for odd modes (21)}$$

In the case of $\theta_1=\theta_2=\theta$, equation (20) for even modes can be solved when the denominator part of equation (20) is infinite, that is, $\theta=(2n-1)\pi/2$, where n is a positive integer. Thus, the first and second even mode resonant frequencies (f_{E1} and f_{E2}) can be obtained as $\theta(f_{E1})=\pi/2$ and $\theta(f_{E2})=\pi$, respectively. Similarly, in the case of $\theta_1=\theta_2=\theta$, equation (21) for odd mode can be solved when the numerator part of equation (21) is zero, that is, $\theta=\tan^{-1}\sqrt{K}$, where K is defined by Z_2/Z_1. Therefore, the first and second odd mode resonant frequencies (f_{O1} and f_{O2}) can be found as $\theta(f_{O1})=\tan^{-1}\sqrt{K}$ and $\theta(f_{O2})=\pi-\tan^{-1}\sqrt{K}$, respectively.

Fig. 40 plots the first two even mode and the first two odd mode resonant frequencies normalized by the first even mode resonant frequency against the value of K. It is noticeable that when K=1, the resonant frequencies are placed at integer multiples of the first odd mode resonant frequency (f_{O1}). This is because the stepped impedance resonator becomes a strip line without the stepped section when K=1. Also, it is also found

that the three resonant frequencies within the passband are symmetrical around the center frequency.

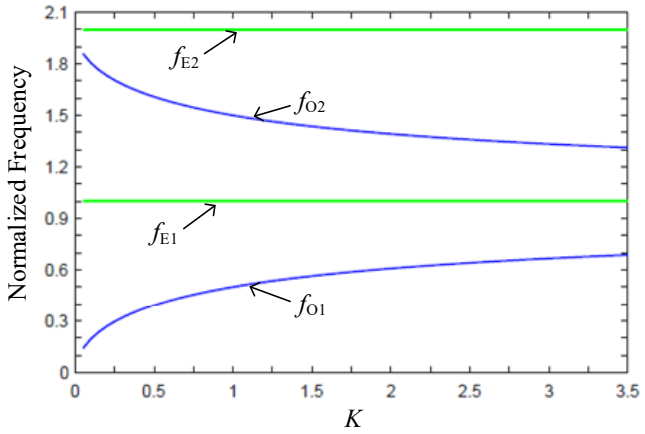

Fig. 40. Resonant frequencies (f_E: even mode, f_O: odd mode) normalized by $\pi/2$ for the stepped impedance resonator in Fig. 39 with respect to K.

In Fig. 40, the first three resonant frequencies of the resonator (f_{O1}, f_{E1}, and f_{O2}) are used to make the ultra-wideband passband (3.1 GHz to 10.6 GHz). f_{E1} is set to be the desired center frequency of the UWB BPF. The passband bandwidth can be approximately estimated by f_{O2} - f_{O1}. As K increases, f_{O1} and f_{O2} approach f_{E1}, resulting in the narrower passband. If K<1, the wide bandwidth can be obtained, but it is difficult to achieve a tight coupling between the resonator and feed lines. Thus, the value of K is chosen to be greater than 1. Assuming K=2, the normalized values of f_{O1}, f_{E1}, and f_{O2} are 0.61, 1, and 1.39, respectively. The center frequency is set to be 6.8 GHz for the UWB application. The physical length and width of the line section in the middle of the resonator in Fig. 38 are calculated as 5.3 mm and 0.7 mm, respectively. The physical length and

width of the line sections at both sides are also calculated as 5.6 mm and 0.1 mm, respectively.

IV.3. Design of UWB bandpass filter using short stubs

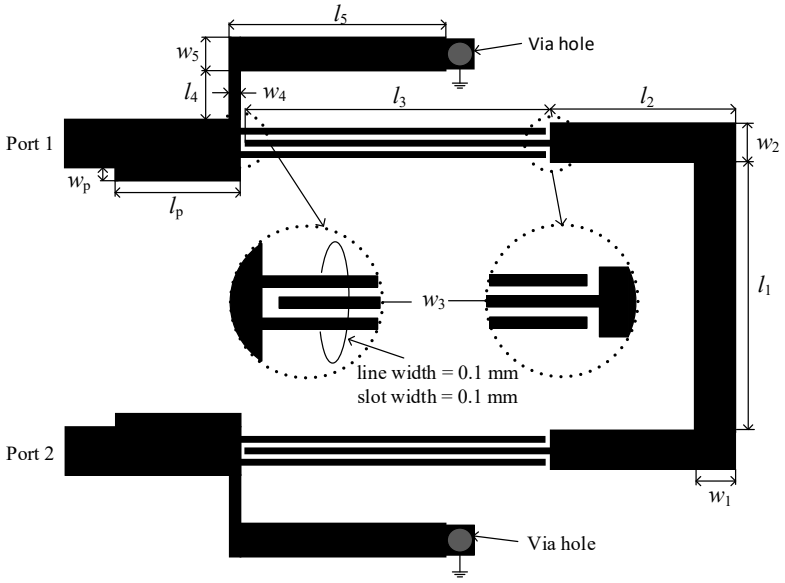

Fig. 41. UWB bandpass filter fed by interdigital coupled feed lines with short stubs.

Fig. 41 shows the configuration of a symmetric stepped impedance resonator fed by interdigital coupled feed lines possessing short stubs. The physical lengths of $l_1/2 + l_2$ and l_3 correspond to the electrical length of θ_1 and θ_2, respectively. The stepped impedance resonator is bent to reduce the circuit size. Considering the bent effect of the resonator, the dimensions of the resonator are designed as follows: l_1=4.73 mm, l_2=3.25 mm, l_3=5.4 mm, w_1=0.7 mm, w_2=0.7 mm, and w_3=0.1 mm. The physical line widths and the slot

widths for the interdigital coupled lines are determined by EM simulations for a better return loss and a low insertion loss in the passband as shown in Fig. 41.

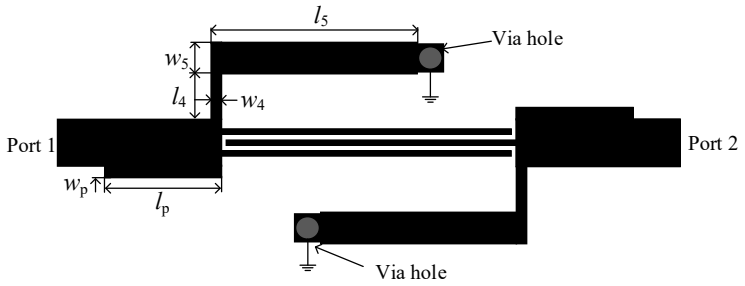

Fig. 42. Interdigital coupled feed lines with the short stubs.

Fig. 42 shows the configuration of the interdigital coupled feed lines with the short stubs to examine the frequency characteristics of only feed lines. The ports and short stubs have stepped impedance sections as in Fig. 42. l_P and w_P denote the length and width of stepped impedance sections of the ports, respectively. In addition, l_4 and l_5 denote the lengths of two different lines of the short stubs, while the widths of the lines are denoted by w_4 and w_5 as in Fig. 42. The short stubs are bent to reduce the circuit size as shown in Fig. 42.

Fig. 43(a) shows the simulated frequency responses of the interdigital coupled feed lines in Fig. 42 according to a variation of l_P from 0 mm to 3.3 mm. For this simulation, the physical line widths and the slot widths of the interdigital coupled lines are fixed at 0.1 mm, and w_P is set to be 0.2 mm. The shorted stub with the stepped impedance section used is as follows: l_4=0.84 mm, l_5=3.86 mm, w_4=0.2 mm, and w_5=0.6 mm. In Fig. 43(a), it is noticeable that the transmission zeros in the upper stopband are barely changed in

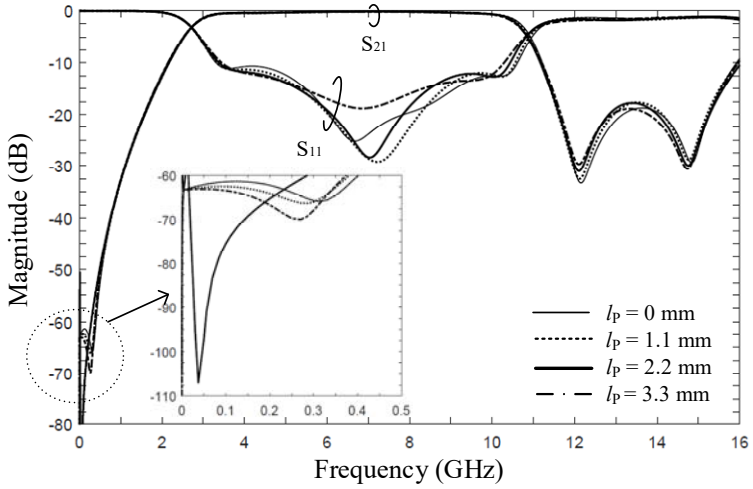

(a)

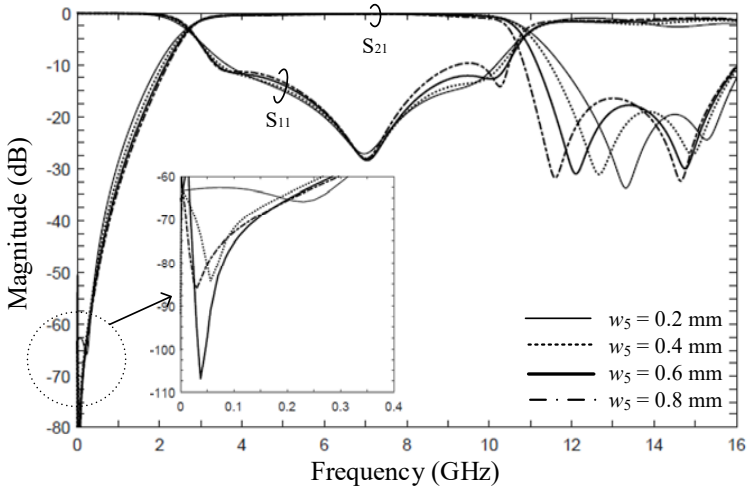

(b)

Fig. 43. Simulated frequency responses of the interdigital coupled feed lines in Fig. 42 with varying (a) l_P and (b) w_5.

relation to varying l_P. As l_P decreases, the return loss in the high frequency of the passband is improved but the return loss in the mid-lower passband becomes worse. Fig. 43(b) shows the simulated frequency responses of the feed lines in Fig. 42 according to a variation of w_5 from 0.2 mm to 0.8 mm. For this simulation, the length and width of the stepped impedance sections of the ports are set to be 2.2 mm and 0.2 mm, respectively. l_4,

l_5, and w_4 are fixed to be 0.84 mm, 3.86 mm, and 0.2 mm, respectively. In Fig. 43(b), w_5 affects the locations of the transmission zeros in the upper stopband. As w_5 increases, the locations of the transmission zeros move to the lower frequencies, resulting in the sharp attenuation slope at the upper edge of the passband. In addition, the return losses in the low and high frequencies of the passband are improved, but the return losses of the mid-lower and the mid-upper passbands become worse. In Fig. 43(a) and (b), it is also noticeable that near DC, a transmission zero is produced. The transmission zero is used to improve the skirt characteristic at the lower edge of the passband and the lower stopband characteristic. The effect of the transmission zero can be displayed when the feed lines with short stubs in Fig. 42 excite the resonator in Fig. 38. Based on the results in Fig. 43 (a) and (b), the interdigital coupled feed lines of the UWB BPF in Fig. 41 are designed by EM simulations as follows: l_4=0.84 mm, l_5=3.86 mm, l_P=2.2 mm, w_4=0.2 mm, w_5=0.6 mm, and w_P=0.2 mm.

Fig. 44 shows the simulated frequency responses of the UWB BPF in Fig. 41. The dimensions of the BPF are as follows: l_1=4.73 mm, l_2=3.25 mm, l_3=5.4 mm, l_4=0.84 mm, l_5=3.86 mm, l_P=2.2 mm, w_1=0.7 mm, w_2=0.7 mm, w_3=0.1 mm, w_4=0.2 mm, w_5=0.6 mm, and w_P=0.2 mm. In the same figure, the result is compared with not only the simulated result of the UWB BPF without the short stubs and the stepped impedance sections of the ports, but also with the simulated result of the only feed lines in Fig. 42. Comparing the UWB BPF in Fig. 41 with the UWB BPF without the short stubs and the stepped impedance section of the ports, it is found that the total number of resonant frequencies within the passband is increased from 3 to 7. The resonant frequencies are symmetrically

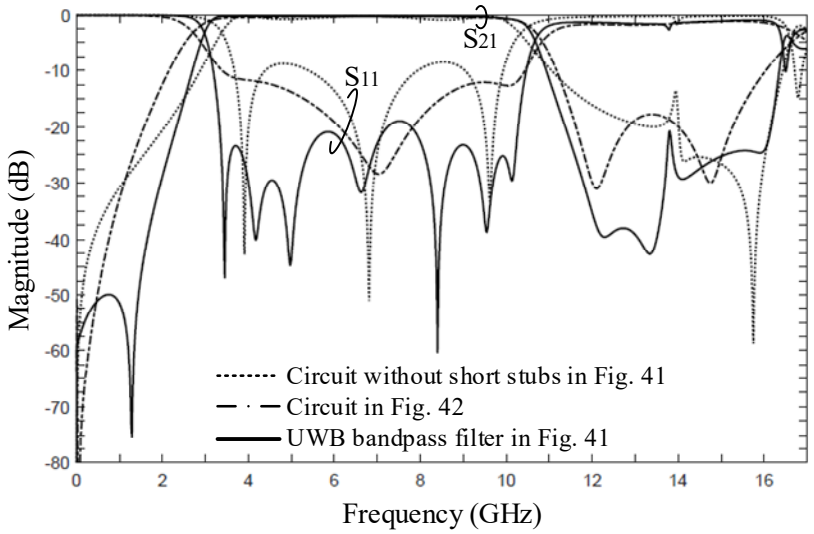

Fig. 44. Simulated frequency responses of the feed lines in Fig. 42, circuit without stubs and impedance sections in UWB bandpass filter in Fig. 41, and UWB bandpass filter in Fig. 41. (l_1=4.73 mm, l_2=3.25 mm, l_3=5.4 mm, l_4=0.84 mm, l_5=3.86 mm, l_P=2.2 mm, w_1=0.7 mm, w_2=0.7 mm, w_3=0.1 mm, w_4=0.2 mm, w_5=0.6 mm, and w_P=0.2 mm)

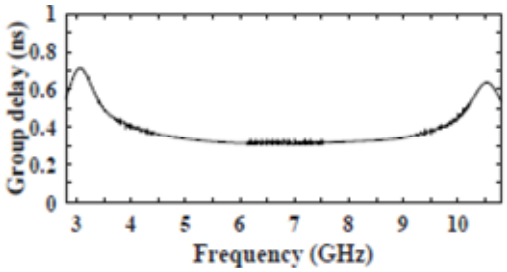

Fig. 45. Group delay for UWB bandpass filter in Fig. 41.

distributed around the center frequency, and the return loss within the passband is significantly improved as shown in Fig. 44. Additionally, it is noticeable that there is a transmission zero near the lower edge of the passband, resulting in the sharper rejection in the lower transition band. This transmission zero comes from the transmission zero near DC as shown in Fig. 43. In addition, the transmission zeros within the higher stopband

improve the upper stopband characteristic and the skirt characteristic at the upper edge of the passband.

The UWB BPF in Fig. 41 shows a 3-dB bandwidth from 3 GHz to 10.6 GHz and a fractional bandwidth (FBW) of about 112 %. The insertion loss at the center frequency is 0.18 dB, and the return loss is greater than 19 dB within the passband. Fig. 45 shows the simulated group delay variation over the passband of the UWB BPF in Fig. 41. The group delay at the lower and higher edges of the passband are about 0.72 ns and 0.64 ns, respectively, while the group delay is quite flat with about 0.3 ns in the passband.

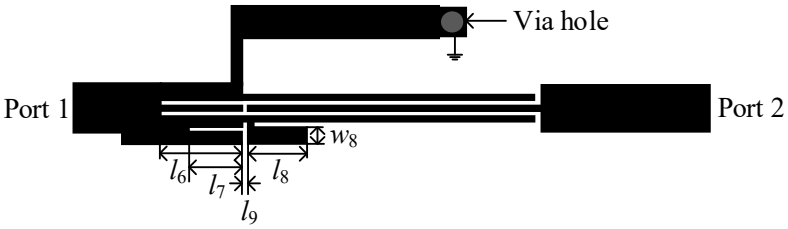

(a)

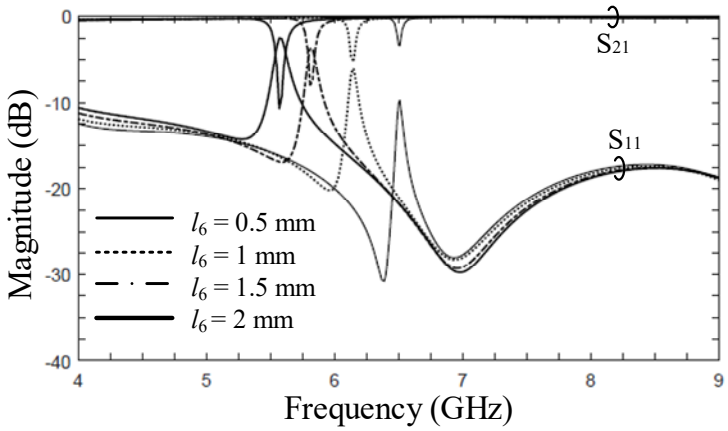

(b)

Fig. 46. (a) Modified interdigital coupled feed line for a notched band characteristic. (b) Simulated frequency responses with varying l_6 when l_6=1.5 mm, l_7=1 mm, l_8=1.1 mm, l_9=0.1 mm, and w_8=0.3 mm.

IV.4. UWB bandpass filter with a notched band

To avoid interferences with WLAN signals, a notched band characteristic becomes essential. The interdigital coupled feed lines are modified as shown in Fig. 46(a). The slots of the interdigital coupled feed lines are extended into port 1, and the length of the slots is used to tune the notch band. A rectangular patch is connected to one of the feed lines to increase the asymmetry of the feed line, and an additional slot is inserted into port 1 to improve the rejection level of the notched band. In Fig. 46(b), the notched bands are introduced at 6.51 GHz, 6.14 GHz, 5.82 GHz, and 5.58 GHz as l_6 increases from 0.5 mm to 2 mm, sequentially. For this simulation, the dimensions of the stepped impedance section of port 1 and the short stubs are used as shown in Fig. 44. The dimensions of the modified interdigital coupled feed line are as follows: l_6=1.5 mm, l_7=1 mm, l_8=1.1 mm, l_9=0.1 mm, and w_8=0.3 mm.

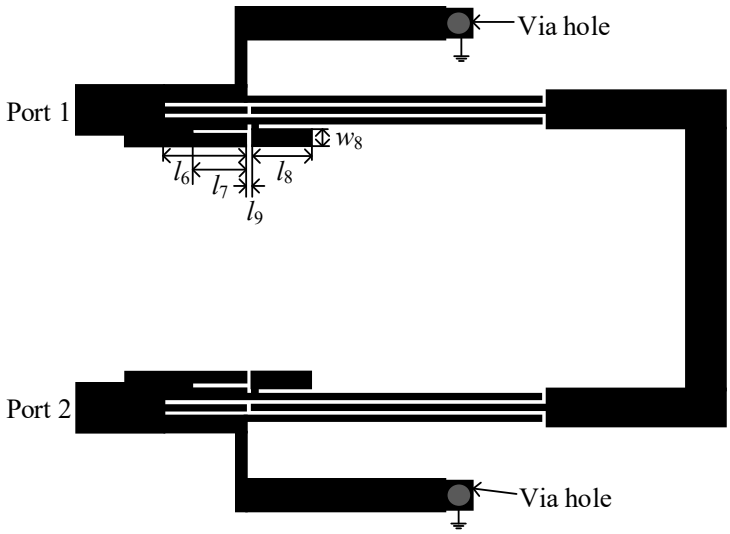

Fig. 47. UWB bandpass filter with a notched band.

Fig. 47 shows the configuration of the UWB BPF with a notch band at 5.8 GHz. All the dimensions of the resonator, the stepped impedance sections of the ports, and the short stubs are the same as in Fig. 44. The modified interdigital coupled feed lines are the same as in Fig. 46.

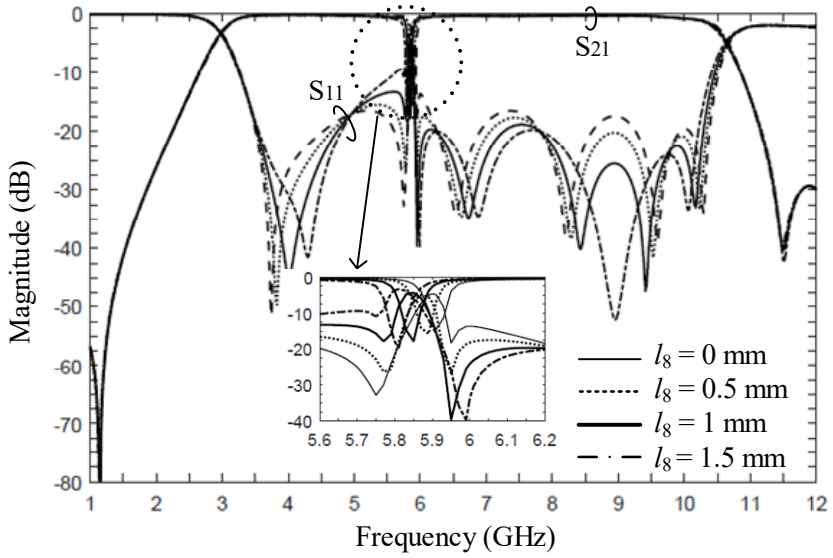

Fig. 48. Simulated frequency responses of UWB BPF with a notch band in Fig. 47 with varying l_8 from 0 mm to 1.5 mm.

Fig. 48 shows the simulated frequency responses of the UWB BPF with a notched band in Fig. 47 according to a variation of l_8. As l_8 increases, the return loss of the mid-upper passband is improved, but the return loss of the mid-lower passband becomes worse. It is also noticeable that the notched band is slightly shifted to the lower frequency. Thus, l_8 is determined by considering the characteristics of the mid-lower and the mid-upper passbands, and the slightly shifted center frequency of the notched band can be

compensated by adjusting l_6. The resonant frequencies placed on both sides of the notched band significantly improve the selectivity and symmetry of the notched band.

The simulated frequency responses and group delay variation of the UWB BPF with a notched band in Fig. 47 are shown in Fig. 49(a) and (b), respectively. The notched

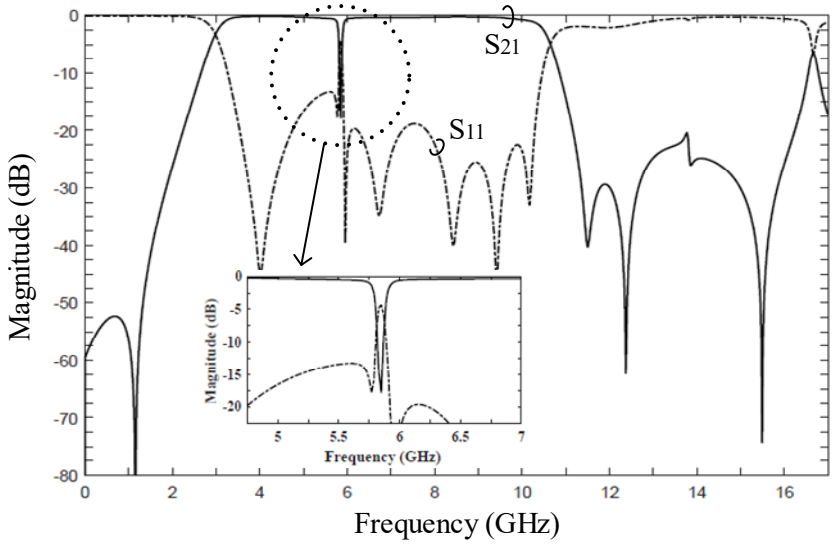

(a)

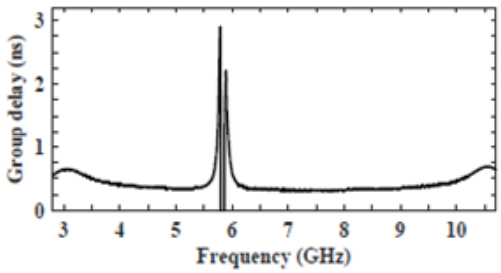

(b)

Fig. 49. (a) Simulated frequency responses of UWB BPF with a notched band in Fig. 47. (l_1=4.73 mm, l_2=3.25 mm, l_3=5.4 mm, l_4=0.84 mm, l_5=3.86 mm, l_6=1.5 mm, l_7=1 mm, l_8=1.1 mm, l_9=0.1 mm, l_P=2.2 mm, w_1=0.7 mm, w_2=0.7 mm, w_3=0.1 mm, w_4=0.2 mm, w_5=0.6 mm, w_8=0.3 mm, and w_P=0.2 mm) (b) Group delay for UWB bandpass filter with a notched band in Fig. 47.

band is observed at 5.8 GHz with the rejection level of 18 dB while the FBW is about 1.77 %. The notched band shows considerably high selectivity and symmetry due to the resonant frequencies at both sides of the notched band. The FBW of the UWB BPF in Fig. 47 is about 111 %, and the group delay within the passband is flat with about 0.3 ns.

IV.5. Time-domain characteristics of UWB BPFs

To investigate the pulse distortion of the signal received through the UWB BPFs in Fig. 41 and Fig. 47, it is necessary to do an experiment on the time-domain performance of the proposed UWB filters. Fig. 50(a) and (b) show the received signal waveform in time-domain after the transmitted signal at port 1 is received at port 2 of the UWB BPFs both without and with a notched band, respectively. As a test signal, a transmitted signal

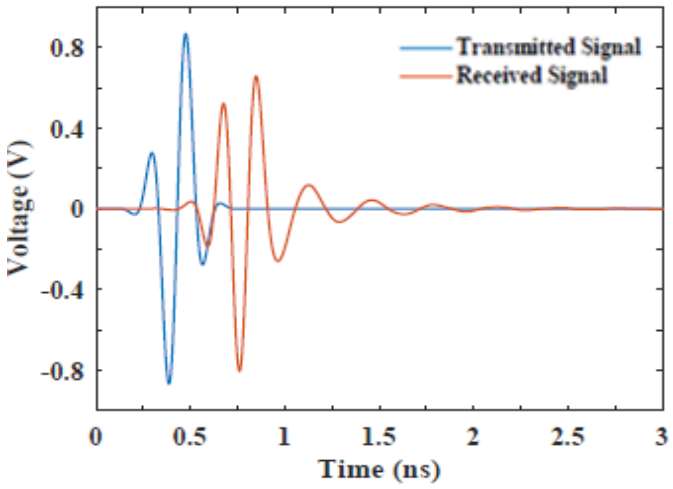

(a)

Fig. 50. The signals waveform transmitted and received through the UWB BPF (a) without and (b) with a notched band.

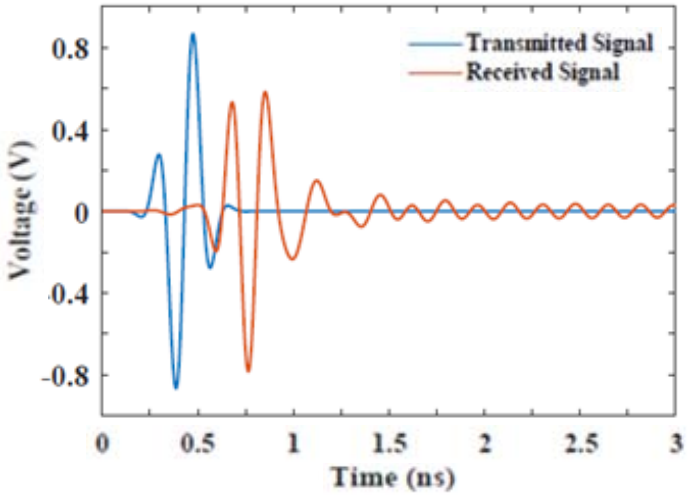

(b)

Fig. 50 Continued.

is modulated to be a unity-amplitude Gaussian RF pulse, which has a FBW of 30 % at the center frequency of 5 GHz. In Fig. 50(a) and (b), it takes about 0.3 ns for the amplitude of the envelope of the transmitted signal to be transferred through the proposed UWB BPFs. The results of the delay time in Fig. 50(a) and (b) are the same as the results of the group delay in Fig. 45 and Fig. 49(b), respectively. In addition, the received waveform at port 2 is similar to the time derivative of the transmitted signal at port 1 due to the filtering characteristic. In other words, the output of the filter can be modeled by the inverted derivative of the transmitted Gaussian pulse [46]. There is a slight distortion and ringing effect, which are unavoidable in reality, in the received signals at port 2 because of the band-limited signal. Comparing the received signals in Fig. 50(a) with (b), the maximum values of the received signals are almost same, but the ringing effect is larger in the case of the UWB BPF with a notched band. The ringing effect causes the leakage of the pulse energy of the transmitted signal, resulting in signal distortion.

Fig. 51(a) and (b) show the power of the transmitted and received signals in time-domain to measure the signal distortion. With the definition of Gaussian pulse width (T_p), discussed in chapter III, as the energy within the pulse width of the transmitted signal is more transferred, the received signal has less pulse distortions. In Fig. 51(a) and (b), the

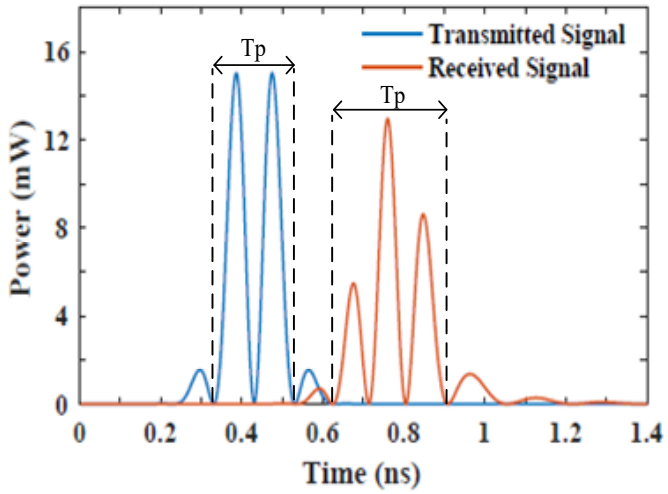

(a)

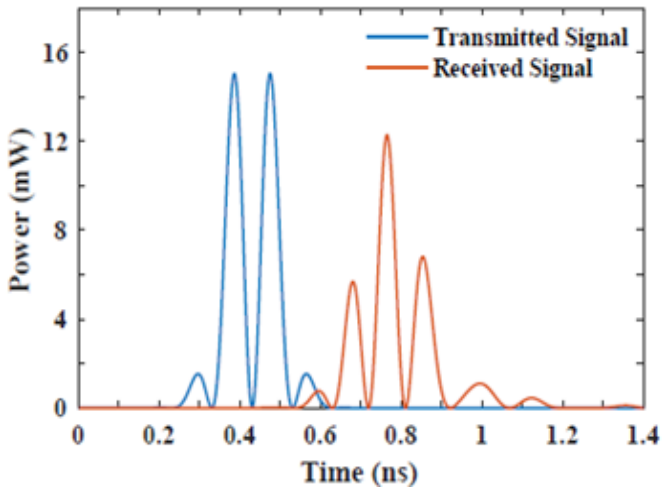

(b)

Fig. 51. Power of the signals transmitted and received through the UWB BPF (a) without and (b) with a notched band.

pulse width of the transmitted signal is 0.2 ns, in which 91.34 % of the pulse energy is contained. The energy within the pulse width is calculated by integrating signal power with respect to time. However, considering the effect of the time derivative of filtering, the pulse width of the received signal is compared to the pulse width of the time derivative of the transmitted signal. The pulse width of the time derivative of the transmitted signal in Fig. 50(a) and (b) is 0.27 ns. In Fig. 51 (a) and (b), the pulse width of the received signal of the UWB BPF without a notched band in Fig. 41 is 0.285 ns with 88.48 % of the pulse energy, while the pulse width of the received signal of the UWB BPF with a notched band in Fig. 47 is 0.29 ns with 85.56 % of the pulse energy. The pulse width of the signal received through the UWB BPF with a notched band is almost the same as the pulse width of the signal received through the UWB BPF without a notched band. When comparing the two results to the pulse width of the derivative of the transmitted signal, it is shown that the distortion of the pulse width of the received signals of the UWB BPFs either with or without a notched band is negligible.

Fig. 52(a) and (b) show the frequency spectrum of the signals transmitted and received through UWB BPF without and with a notch band, respectively. The transmitted signal is the same as in Fig. 50. The maximum value of the signals is at 5 GHz because the transmitted pulse is modulated by the Gaussian pulse with a center frequency of 5 GHz. In Fig. 52(a), the frequency spectrum of the signal received through UWB BPF without a notched band is almost the same as the frequency spectrum of the transmitted signal within the frequency band (3 GHz to 10.5 GHz), which is the passband bandwidth of the proposed UWB filter in Fig. 41. Hence, it is proven that the frequency elements

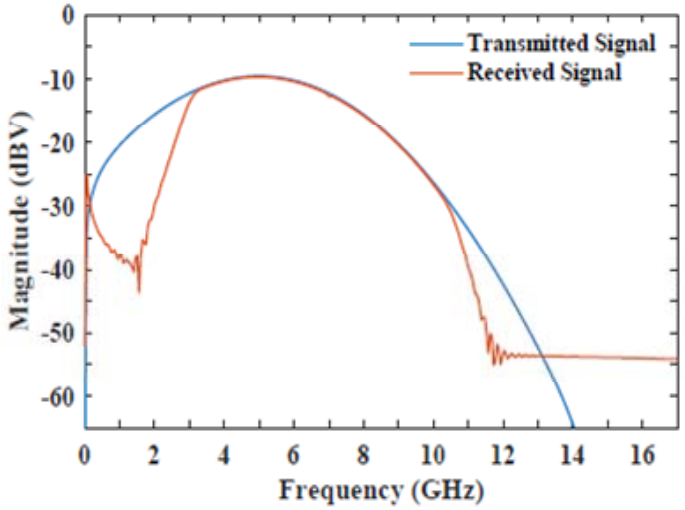

(a)

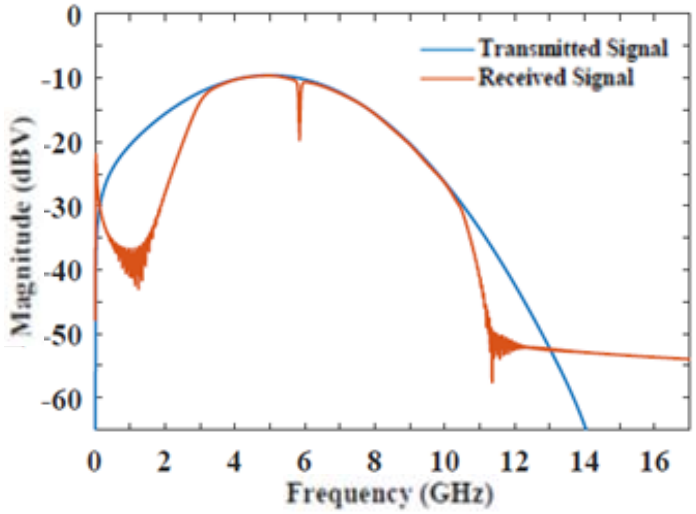

(b)

Fig. 52. Frequency spectrum of the transmitted and received signals of the UWB BPF (a) without and (b) with a notched band.

between 3 GHz and 10.5 GHz are passed through the UWB BPF in Fig. 41, while the frequency elements out of the passband are stopped. On the other hand, in Fig. 52(b), it is found that there is a notched band at 5.8 GHz in the frequency spectrum of the signal received through UWB BPF with a notched band. The notched band is the same as in Fig.

49. Thus, it is proven that the notched frequency elements of the signal are rejected through the UWB BPF in Fig. 47. Comparing Fig. 52(a) with (b), the frequency spectrum of the signal received through the UWB BPF without a notched band is almost the same as the frequency spectrum of the signal received through the UWB BPF with a notched band within the passband (3 GHz to 10.5 GHz), except a notched band at 5.8 GHz. The time-domain performance is summarized in Table 4. Based on the time-domain analysis, it is shown that the proposed UWB filters with and without a notched band have satisfactory performances in both the time- and frequency-domains.

Table 4. Time-domain analysis results of Fig. 41 and Fig. 47.

Time-domain analysis	Transmitted signal	Derivative of transmitted signal	UWB BPF without a notched band	UWB BPF with a notched band
Time delay	-	-	0.33 ns	0.33 ns
Pulse width	0.2 ns	0.27 ns	0.28 ns	0.29 ns
Energy percentage within pulse width	91.34 %	96.7 %	88.48 %	85.56 %
3-dB bandwidth	-	-	2.86 GHz ~ 10.73 GHz	2.8 GHz ~ 10.67 GHz

IV.6. Conclusion

UWB bandpass filters using a symmetric stepped impedance resonator and short stubs have been proposed. The stepped impedance resonator is designed based on the analyzed resonant frequencies to obtain a wide bandwidth. The interdigital coupled feed lines with the short stubs are designed to achieve a better return loss and a low insertion

loss. The UWB BPF with short stubs provides 7 resonant frequencies within the passband with the desirable passband characteristic and stopband characteristic. A notched band is introduced by adding open stubs and slots in the feed lines. The notched band can be adjusted according to the length of the slots. A time-domain analysis is made to verify the performances in a frequency-domain. The proposed UWB BPF shows the satisfactory performances in a time-domain as well as a frequency-domain. The proposed UWB filters have useful features such as a low insertion loss, sharp skirt characteristics in both transition bands, and a flat group delay within the passband.

CHAPTER V

WIDEBAND BANDPASS FILTER WITH A HIGH SELECTIVITY USING AN INVERTED T-SHAPED RESONATOR AND SHORT STUBS

V.1. Introduction

Today's wireless communication and radar systems require microwave bandpass filters (BPFs) to have higher performances such as compactness, a wide stopband, and high selectivity. Since the Federal Communications Commission (FCC) defines Ultra-wideband (UWB) as a technology with a fractional bandwidth (FBW) more than 20% or with bandwidth more than 500MHz, there have been many studies on wideband structures using many techniques to achieve a specified FBW. In [47], [48], and [49], parallel coupled lines were used to produce the FBW of 50 %, 64 %, and 85 %, respectively, and a defected ground structure (DGS) on the ground plane was used for the design of a low pass filter (LPF) cascaded to UWB BPF [50]. In addition, the ring resonators were used to produce multiple resonances for wideband applications [51], [52], and wideband BPFs were proposed based on the transversal signal-interference concept [53-56].

In this chapter, wideband BPFs with an inverted T-shaped resonator, excited by either parallel coupled feed lines with or without short stubs, are proposed. The resonant frequencies of the resonator are analyzed using the equivalent circuits, and the design formulas for the resonator are derived. The design of parallel coupled feed lines is made by investigating the effect of varying even and odd impedances on frequency responses to obtain a flat and wide passband. Also, the effects of the length and width of the short stubs

on frequency responses are studied in detail to design a wideband BPF with a very high selectivity and a wide stopband. The proposed BPFs use an RT/Duroid 5880 substrate with a thickness of 0.7874 mm and a relative dielectric constant of 2.2. Electromagnetic (EM) simulations in this chapter are performed by Zeland IE3D based on method of moments.

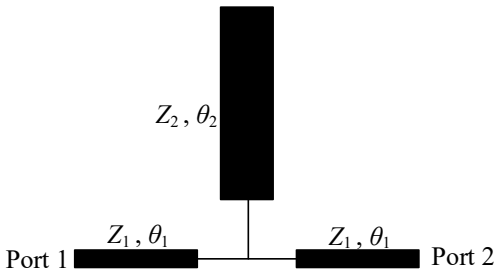

Fig. 53. The inverted T-shaped resonator.

V.2. Bandpass filter fed by parallel coupled feed lines

V.2.A. Analysis of inverted T-shaped resonator

Fig. 53 shows the configuration of the inverted T-shaped resonator. The resonator is a simple structure, in which an open circuited stub is located at the center of a strip line. Z_1 and θ_1 are the characteristic impedance and the electrical length for a half of the strip line, respectively, while Z_2 and θ_2 denote the characteristic impedance and the electrical length of the open circuited stub, respectively. The characteristic impedance and the electrical length correspond to the physical width and length, respectively. Due to the symmetry of the resonator, the even and odd analysis methodology can be applied to analyze resonant frequencies.

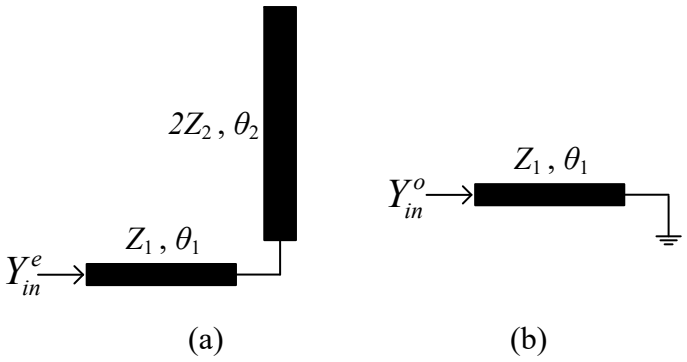

Fig. 54. Equivalent circuits of the inverted T-shaped resonator in Fig. 53. (a) even modes. (b) odd modes.

Fig. 54(a) and (b) show the equivalent circuits of the inverted T-shaped resonator for the even and odd modes, respectively. For the even modes, the characteristic impedance of the open stub become double because the width of the stub is cut in half as shown in Fig. 54(a). For the odd modes, the equivalent circuit has nothing to do with the open stub because one end is short-circuited, as shown in Fig. 54(b). The even and odd mode resonance responses can be calculated under the condition of $Z_{in}=\infty$ (or $Y_{in}=0$), which are obtained as follows:

$$Y_{in}^e = \frac{2K\tan\theta_1 + \tan\theta_2}{\tan\theta_1\tan\theta_2 - 2K} = 0 \qquad \text{for even modes (22)}$$

and

$$Y_{in}^o = \tan^{-1}\theta_1 = 0 \qquad \text{for odd modes (23)}$$

where $K= Z_2/Z_1$.

Fig. 55(a) and (b) show the even and odd mode resonant frequencies normalized by $\pi/2$ with respect to Z_2/Z_1 and θ_2/θ_1, respectively. In Fig. 55(a), θ_2/θ_1 is fixed to be 1.66, while Z_2/Z_1 is fixed to be 0.13 in Fig. 55(b). The first odd mode resonant frequency and

the first and second even mode resonant frequencies (f_{O1}, f_{E1}, and f_{E2}) are used to make the passband, and the difference between the first and second even mode resonant frequencies (f_{E2} - f_{E1}) is used to estimate a passband bandwidth. To include f_{O1}, f_{E1}, and f_{E2} within the passband, θ_2/θ_1 should be greater than 1 and less than 3 as shown in Fig. 55(b). In Fig. 55

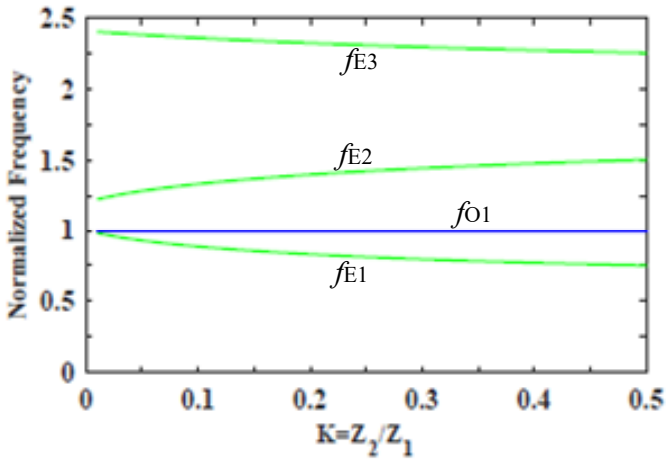

(a)

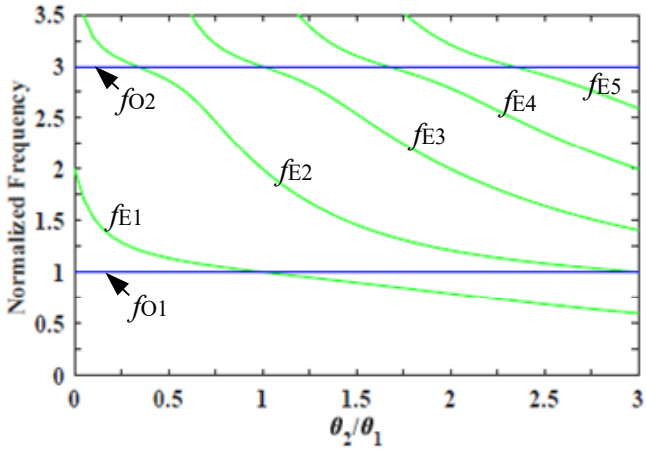

(b)

Fig. 55. Resonant frequencies (f_E: even mode, f_O: odd mode) normalized by $\pi/2$ for the resonator in Fig. 53 with respect to (a) $K=Z_2/Z_1$ when $\theta_2/\theta_1=1.66$ and (b) θ_2/θ_1 when $Z_2/Z_1=0.13$.

(a) and (b), the effect of varying Z_2/Z_1 and θ_2/θ_1 on the passband can be estimated. As Z_2/Z_1 increases, the passband bandwidth becomes wider as shown in Fig. 55(a). In Fig. 55(b), for θ_2/θ_1 greater than 1.5 and less than 3, the passband bandwidth is barely changed in relation to varying θ_2/θ_1, but the passband is shifted to the lower frequency band as θ_2/θ_1 increases. Thus, the passband bandwidth is mainly controlled by Z_2/Z_1, while θ_2/θ_1 is mainly used to adjust the passband location. In other words, Z_2/Z_1 is calculated by a specified bandwidth and θ_2/θ_1 is used to tune the passband locations. It is also noticeable that spurious frequencies are periodically occurred at integer multiples of the fundamental frequency when $\theta_2/\theta_1=0$.

Based on the analysis of the resonant frequencies in Fig. 55, the values of Z_2/Z_1 and θ_2/θ_1 of the T-shaped resonator are obtained so that the resonant frequencies are located within the specified bandwidth. The corresponding lower and upper edge frequencies of the desired passband are calculated by:

$$f_1 = \frac{2 f_C f_{E1}}{f_{E1} + f_{E2}} \quad \text{for the lower edge of the passband} \tag{24}$$

and

$$f_2 = \frac{2 f_C f_{E2}}{f_{E1} + f_{E2}} \quad \text{for the upper edge of the passband} \tag{25}$$

where f_{E1} and f_{E2} are the normalized first and second even mode resonant frequencies, respectively, and f_C is the desired center frequency. However, the calculated resonant frequencies can be slightly different from the actual resonant frequencies because the circuit actually implemented as in Fig. 56 is different from the ideal T-shaped resonator in Fig. 53 at the T junction. Thus, based on the resonant frequencies estimated in Fig. 55(a)

and (b), the T-shaped resonator is slightly modified by EM simulations so that the resonant frequencies are placed at the desired locations.

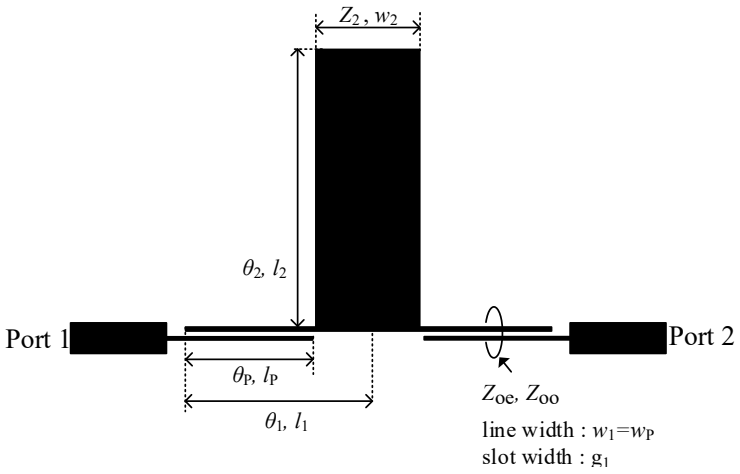

Fig. 56. Inverted T-shaped resonator fed by parallel coupled feed lines.

V.2.B. Parallel coupled feed lines

On the basis of the derived formulas for even and odd mode resonant frequencies, a BPF with a FBW of about 50 % at a center frequency of 5 GHz is designed to verify the analysis results in Fig. 55. Fig. 56 shows the configuration of the inverted T-shaped resonator fed by parallel coupled feed lines. The widths of the parallel coupled lines are the same as w_1, which corresponds to Z_1, for the symmetric parallel coupling. θ_p is the coupled electrical length between the resonator and feed lines, and the corresponding physical length is l_p. Also, Z_{oe} and Z_{oo} are the even and odd mode characteristic impedances of the coupled lines, respectively.

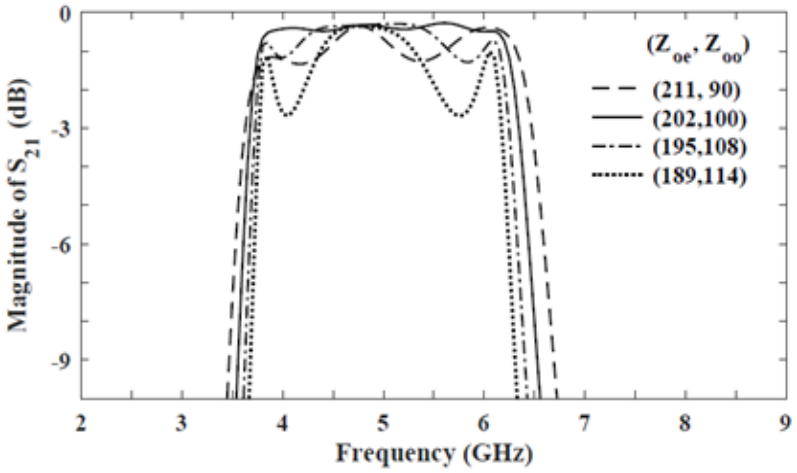

(a)

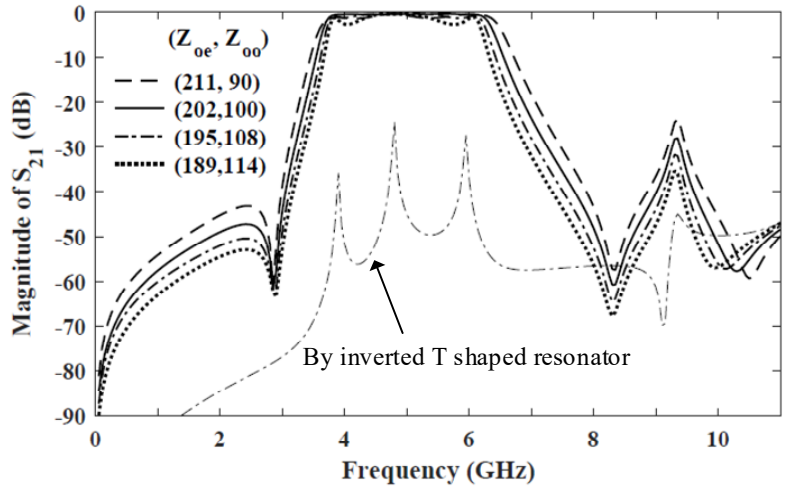

(b)

Fig. 57. Simulated results of BPF with parallel coupled feed lines in Fig. 56 for S_{21} when θ_1=111 °, θ_2=185 °, Z_1=150 Ω, Z_2=20 Ω, Z_{oe}=202 Ω, and Z_{oo}=100 Ω. (a) Zoom-in for tunable bandwidth. (b) Entire frequency range.

Fig. 57 shows the simulated S_{21} of the inverted T-shaped resonator fed by the parallel coupled feed lines with different pairs of (Z_{oe}, Z_{oo}). The dimensions of the resonator in Fig. 56 are obtained from the results analyzed in Fig. 55(a) and (b) as follows: θ_1=111 °, θ_2=185 °, Z_1=150 Ω, Z_2=20 Ω. θ_1=111 °, and θ_2=185 ° correspond to the physical

lengths of l_1=14.25 mm and l_2=21.7 mm, respectively, while Z_1=150 Ω and Z_2=20 Ω correspond to the physical widths of w_1=0.23 mm and w_2=8 mm, respectively.

To investigate the effect of different coupling gaps on the frequency responses, (Z_{oe}, Z_{oo}) is chosen to be (211, 90), (202, 100), (195, 108), and (189, 114), which correspond to the coupling gap (g_1) of 0.2, 0.3, 0.4, and 0.5, respectively. It is found that the estimated FBWs are 56.2 %, 53 %, 50.6 %, and 48.5 %, when (Z_{oe}, Z_{oo}) is (211, 90), (202, 100), (195, 108), and (189, 114), respectively, as shown in Fig. 57(a). In other words, the FBW of the BPF in Fig. 56 decreases as the coupling gap increases. However, there are some fluctuations within the passband for each different (Z_{oe}, Z_{oo}) as shown in Fig. 57(a). To minimize the fluctuation, (Z_{oe}, Z_{oo}) is selected to be (202, 100), which corresponds to g_1=0.3 mm and w_1= w_p=0.23 mm. If the FBW of the BPF is unacceptably different from the specified FBW, which is either wide or narrow, the inverted T-shaped resonator should be redesigned according to the analysis in Fig. 55 so that the resonant frequencies in Fig. 57(b) are located to achieve the specified bandwidth. The BPF is designed so that the center frequency is the same as the center frequency of the desired BPF from (23) and (24). Thus, the bandwidth is only adjusted by properly locating the resonant frequencies at both sides of the passband. The difference between the specified bandwidth and the initially designed bandwidth is used to appropriately select the normalized even mode resonant frequencies of f'_{E1} and f'_{E2} as follows:

$$\Delta BW = BW_{specified} - BW_{initial} = \frac{f_C}{1.125}\left\{\left(f'_{E2} - f'_{E1}\right) - \left(f_{E2} - f_{E1}\right)\right\}$$

$$= \frac{2f_C}{1.125}\left(f'_{E2} - f_{E2}\right) = \frac{2f_C}{1.125}\left(f_{E1} - f'_{E1}\right) \tag{26}$$

where f'_{E1}, f'_{E2} are the adjusted values of the normalized even mode resonant frequencies, and f_{E1}, f_{E2} are the initially selected values of the normalized even mode resonant frequencies. If the initial bandwidth of the BPF is narrower than the specified bandwidth, ΔBW becomes positive, f'_{E1} is selected to be less than f_{E1}, and f'_{E2} is selected to be larger than f_{E2}. On the other hand, if the initial bandwidth of the BPF is wider than the specified bandwidth, ΔBW becomes negative, f'_{E1} is selected to be larger than f_{E1}, and f'_{E2} is selected to be less than f_{E2}. After f'_{E1}, f'_{E2} are calculated from (25), the corresponding θ_2/θ_1 and Z_2/Z_1 are found, and then the inverted T-shaped resonator with the specified bandwidth is designed. The parallel coupled feed lines are designed by the even and odd mode characteristic impedance analysis as in Fig. 57.

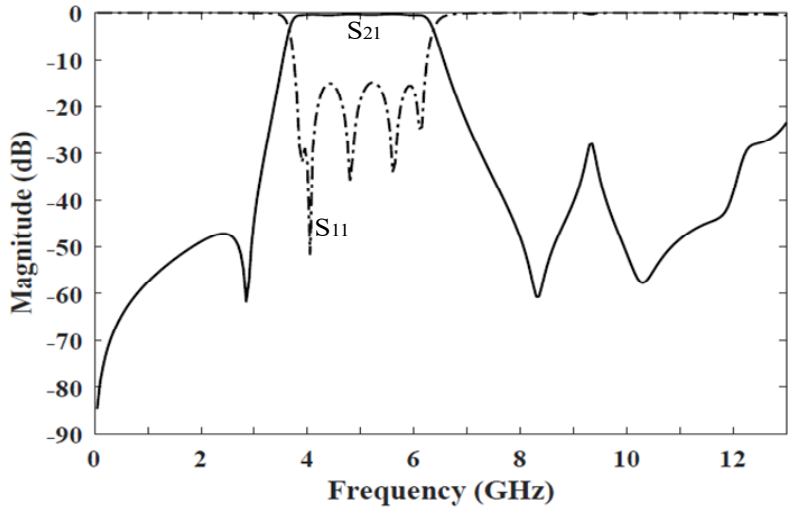

Fig. 58. Simulated frequency responses of the BPF using parallel coupled feed lines in Fig. 56 when l_1=14.25 mm, l_2=21.7 mm, l_P=10 mm, w_1=0.23 mm, w_2=8 mm, w_P=0.23 mm, and g_1=0.3 mm.

Fig. 58 shows the simulated frequency responses of the inverted T-shaped resonator fed by parallel coupled feed lines as in Fig. 56. All the dimensions of the resonator and the parallel coupled feed lines are as follows: l_1=14.25 mm, l_2=21.7 mm, l_P=10 mm, w_1=0.23 mm, w_2=8 mm, w_P=0.23 mm, and g_1=0.3 mm. The length of the coupled feed lines (θ_P) is set to be 78 °, which corresponds to l_P=10 mm. The simulated result in Fig. 58 shows a 3-dB FBW of 53 % at the center frequency of 5GHz. The insertion loss is less than 0.37 dB at the center frequency, and the return loss is better than 15 dB within the passband. Although it shows the desired wide bandwidth, the attenuation rates at both sides of the passband are not high enough, resulting in the poor selectivity, as shown in Fig. 58. Thus, transmission zeros need to be to be created near both sides of the passband to improve the passband selectivity.

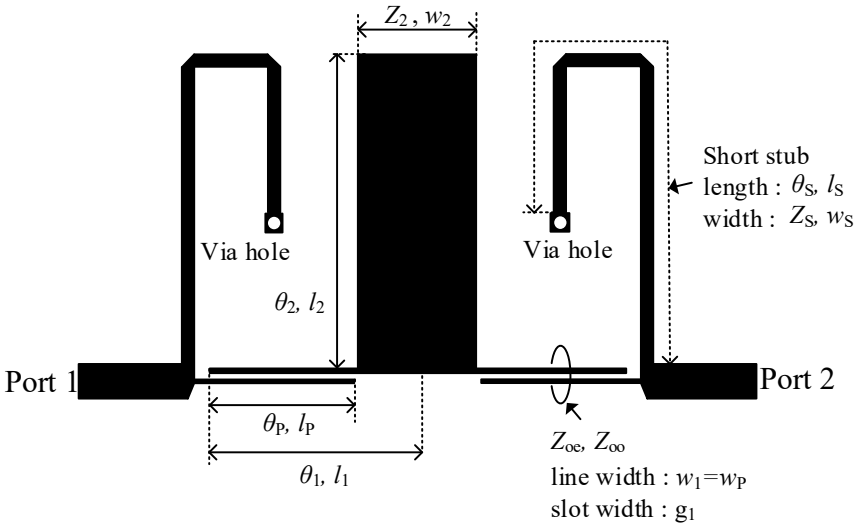

Fig. 59. Inverted T-shaped resonator fed by parallel coupled feed lines with short stubs.

V.3. Design of the wideband BPF using the short stubs

The short stubs are introduced to improve the passband edge skirt and stopband characteristics. Fig. 59 shows the configuration of the wideband BPF with the inverted T-shaped resonator fed by the parallel coupled feed lines possessing short stubs. All the dimensions of the resonator are used as in Fig. 58. The short stubs have the total electrical length (θ_S) and the characteristic impedance (Z_S) corresponding to the physical length l_S and the physical width w_S, respectively. The effect of the parameters of the short stubs on the passband characteristics is analyzed in following sections.

V.3.A. Effect of the electrical length of short stubs(θ_S) on frequency responses

Fig. 60(a) and (b) show the simulated S_{21} and S_{11} responses of the inverted T-shaped resonator fed by parallel coupled feed lines possessing short stubs according to different electrical lengths of stubs. All the dimensions of the resonator and the length of the coupled feed lines (θ_P) are the same as in Fig. 56. Z_{oe} and Z_{oo} are calculated to be 195 Ω and 108 Ω, respectively, for minimized fluctuations and better return losses within the passband. The physical dimensions of the parallel coupled lines corresponding to (Z_{oe}=195 Ω, Z_{oo}=108 Ω) are follows as: w_1=w_P=0.23 mm and g_1=0.4 mm. Also, the characteristic impedance of the short stubs (Z_S) is fixed to be 89 Ω, corresponding to the physical width of 0.9 mm. In Fig. 60(a), when θ_S/θ_1 is 2.34, corresponding to the total physical length of short stubs l_S=32.5 mm, the mid-lower passband bandwidth is decreased, while the return loss decreases in the low frequency band as shown in Fig. 60(b). In the case where θ_S/θ_1 is 2.56, corresponding to the total physical length of short stubs l_S=35.5 mm, the mid-

upper passband bandwidth is decreased as in Fig. 60(a), while the return loss decreases in the high frequency band as shown in Fig. 60(b). By properly selecting θ_S/θ_1 as 2.45, the passband bandwidth at either edge of the passband is not decreased, and consequently the specified passband bandwidth is achieved with the center frequency of 5 GHz. Moreover, with the proper θ_S/θ_1, the attenuation rates at both passband edges can be increased.

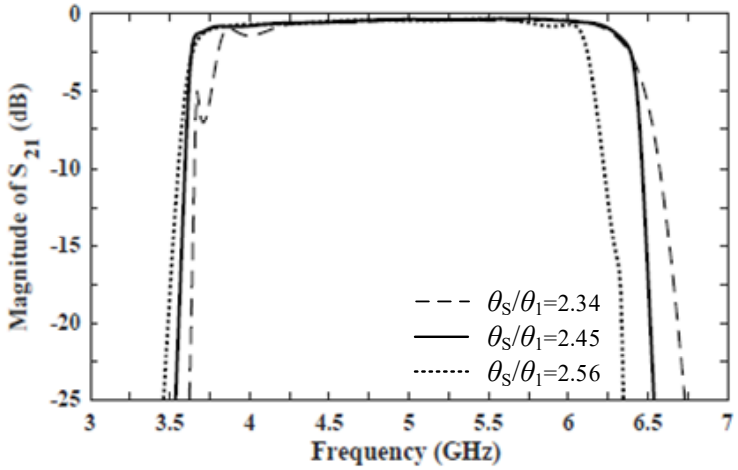

(a)

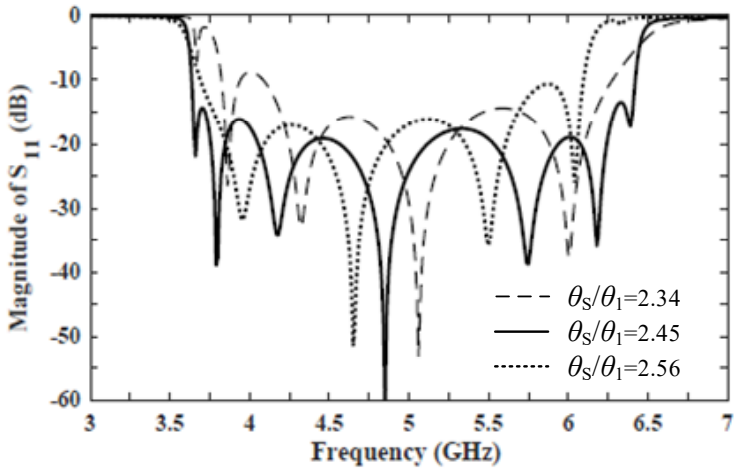

(b)

Fig. 60. Simulated frequency responses of BPF using parallel coupled feed lines with short stubs with varying θ_S/θ_1 when Z_S=89 Ω. (a) S_{21}. (b) S_{11}.

V.3.B. Effect of the characteristic impedance of short stubs (Z_S) on frequency responses

In order to examine the effect of the characteristic impedances of short stubs on frequency responses, the S_{21} and S_{11} responses are simulated for the BPF in Fig. 59 with different characteristic impedances of short stubs as shown in Fig. 61(a) and (b). All the dimensions of the resonator and the coupled feed lines are the same as in Fig. 60. Also, the electrical length of stubs (θ_S/θ_1) is fixed to be 2.45. When Z_S is 67 Ω, corresponding to the physical width of 1.5 mm, both edges of the passband slightly shrink as shown as in Fig. 61(a), while the return loss decreases in both the low and high frequency band as in Fig. 61(b). In the case where Z_S is 138 Ω, corresponding to the physical width of 0.3 mm, both edges of the passband are slightly extended as shown in Fig. 61(a), while the return loss in the low frequency band decreases, and the number of resonant frequencies within the passband decreases as shown in Fig. 61(b). By properly selecting Z_S as 89 Ω,

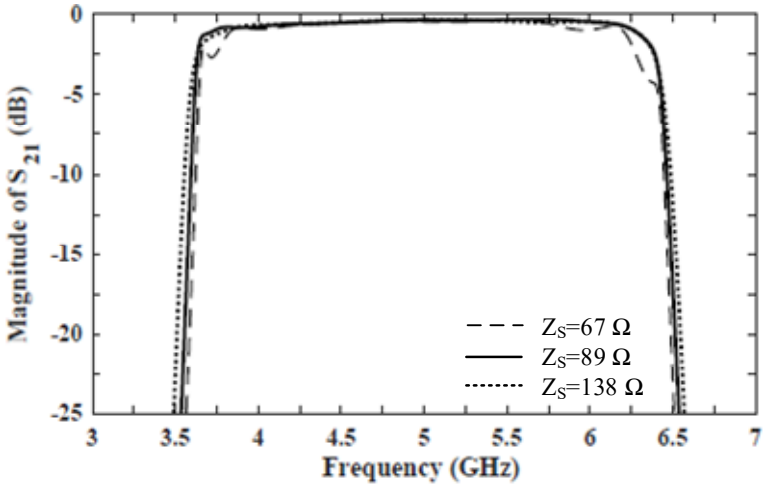

(a)

Fig. 61. Simulated frequency responses of BPF using parallel coupled feed lines with short stubs with varying Z_S when θ_S/θ_1=2.45. (a) S_{21}. (b) S_{11}.

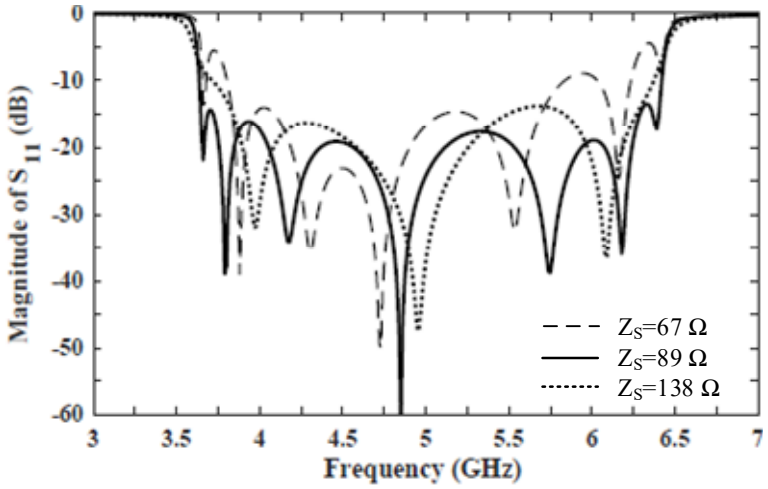

(b)

Fig. 61 Continued.

the seven resonant frequencies are evenly distributed over the passband as in Fig. 61(b), resulting in the passband symmetry. The return loss within the passband is evenly high over the passband, causing a low insertion loss. In addition, the high selectivity at both edges of the passband is achieved as in Fig. 61(a). Based on the analysis in Fig. 60 and Fig. 61, the electrical length (θ_S/θ_1) and characteristic impedance (Z_S) of short stubs are chosen to be 2.45 and 89 Ω, respectively, in order to make the sharp attenuation slopes at both edges of the passband and achieve a better return loss within the passband.

Fig. 62 shows the simulated frequency responses of the BPF with short stubs as in Fig. 59, and the simulated frequency responses of the BPF without short stubs in Fig. 56 are compared in the same figure. The dimensions in Fig. 58 are used to simulate the BPF without short stubs. The line lengths are as follows: θ_1=111 °, θ_2=185 °, θ_P=78 °, and θ_S=272 °, that is, l_1=14.25 mm, l_2=21.7 mm, l_P=10 mm, and l_S=34 mm. Also, the line widths and slot width are used

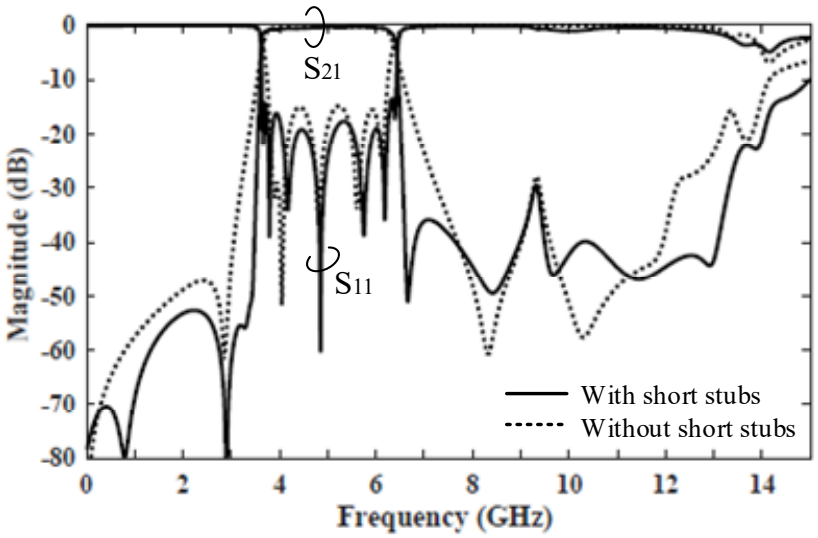

Fig. 62. Simulated frequency responses of BPF using parallel coupled feed lines with and without short stubs when l_1=14.25 mm, l_2=21.7 mm, l_P=10 mm, l_S=34 mm, w_1=0.23 mm, w_2=8 mm, w_P=0.23 mm, w_S=0.9 mm, and g_1=0.4 mm.

as follows: Z_1=150 Ω, Z_2=20 Ω, Z_{oe}=195 Ω, Z_{oo} =108 Ω, and Z_S=89 Ω, that is, w_1=0.23 mm, w_2=8 mm, w_P=0.23 mm, w_S=0.9 mm, and g_1=0.4 mm. Compared to the inverted T-shaped resonator fed by parallel coupled feed lines without short stubs, the T-shaped resonator with short stubs has an increased number of resonant frequencies within the passband of 7, as opposed to 5 without short stubs. Additionally, the attenuation slopes of both passband edges are much improved. The result indicates a very high selectivity and a passband symmetry with attenuation slopes of 278 dB/GHz and 263 dB/GHz for the lower and upper passband edges, respectively. The FBW is about 55 % at the center frequency of 5 GHz. Also, it is found that the stopband is extended up to 14 GHz at a suppression level of 20 dB. The transmission zeros produced by the short stubs improve the stopband characteristics as well as the attenuation rate at both sides of the passband as shown in Fig. 62.

V.4. Conclusion

A novel wideband BPF with the inverted T-shaped resonator using parallel coupled feed lines with short stubs has been developed. The design of the inverted T-shaped resonator is made by analyzing the resonant frequencies from the equivalent circuits. The parallel coupled feed lines with short stubs produce the transmission zeros near both sides of the passband, causing the significantly improved attenuation rate. Additionally, with the feed lines with short stubs, the transmission zeros are produced within the stopband, resulting in improved stopband characteristics compared to the BPF with parallel coupled feed lines without short stubs. Furthermore, the number of the resonant frequencies within the passband is increased, and the return loss within the passband is significantly improved. The effects of the length and width of the short stubs on frequency responses are studied to obtain optimized design of the short stubs. The proposed wideband BPF with short stubs provides a FBW of about 55 % with a very high selectivity, a passband symmetry, and a wide stopband characteristic.

CHAPTER VI

SUMMARY

In this dissertation, microwave bandpass filters to achieve today's filter requirements, such as spurious harmonic suppressions, a wide stopband, multi-passband, reconfigurable capability, wide or ultra-wide passband, and high selectivity at both passband edges have been studied.

In Chapter II, novel single- and dual-band bandpass filters with stepped impedance stubs have been studied. The design of the resonator with the stepped impedance stub is made by analyzing the even and odd mode resonant frequencies, which can be obtained from the even and odd mode equivalent circuits. The resonator is excited by novel S-shaped coupled feed lines to suppress spurious harmonic responses. The S-shaped coupled feed lines produce multiple transmission zeros within stopband. The design of the feed lines is made so that the transmission zeros due to the feed lines are placed at unwanted harmonic responses for harmonic suppressions, resulting in wide stopband characteristics. The frequency responses of the S-shaped coupled feed lines are compared with conventional parallel coupled feed lines and interdigital coupled feed lines. A dual-band bandpass filter using stepped impedance stubs is proposed. The resonator is redesigned to have dual-band characteristics at both 2.4 GHz and 5.2GHz, which are unlicensed frequency bands. Based on the analysis of the resonator, it is found that each band of the dual-band BPF can be independently controlled by the parameters of the resonator. The dual-band BPF is fed by S-shaped coupled feed lines to achieve a wide stopband. Using

the characteristics of the resonator, BPF with independently controllable dual-band is developed using PIN diodes. It is found that each passband can be switched by the induced bias voltage of PIN diodes.

In Chapter III, a Ultra-wideband (UWB) bandpass filter using a symmetric stepped impedance resonator with an asymmetric stepped impedance stub is developed. The resonator is designed by analyzing resonant frequencies and transmission zeros to achieve a very wide passband, and the design formulas are derived from equivalent circuits of the resonator. The resonator is excited by the interdigital coupled feed lines with rectangular slots on the ground for a better return loss and a passband symmetry. The effects of the dimensions and locations of the rectangular slot on frequency responses of BPFs are studied. Asymmetric interdigital coupled feed lines are introduced to make a UWB BPF with a notched band to avoid the existing interferences with signals at certain frequencies. It is shown that the notched band can be changed with varying differences between two interdigital coupled feed lines. The proposed UWB BPFs are also analyzed in the time-domain. A Gaussian modulated pulse is used as a transmitted signal, and analysis results in the time-domain are provided. It is found that the UWB BPF without a notched band shows satisfactory performances in both the time- and frequency-domains. The UWB BPF with a notched band has satisfactory performances in the frequency-domain but slight distortions for the frequency range upper than 9.5 GHz based on the time-domain analysis.

In Chapter IV, different types of UWB BPFs with and without a notched band using symmetric stepped impedance have been proposed. The resonator is designed based on the analysis of resonant frequencies to obtain a passband bandwidth between 3.1 GHz

and 10.6 GHz. The design equations of the resonator are provided from its equivalent circuits. The resonator is excited by interdigital coupled feed lines with the short stubs, and the feed lines are designed to achieve a better return loss. The feed lines with short stubs increase the number of resonances within the passband, improving passband characteristics, and produce transmission zeros near both sides of the passband, causing improved skirt characteristics at both passband edges. The modified interdigital coupled feed lines with short stubs are introduced to make a notched band within the passband to avoid the interferences with certain wireless services. By changing the length of inserted slots of the feed lines, the notched band can be adjusted to avoid various frequency bands. The UWB BPFs are analyzed in the time-domain as well as the frequency-domain to verify the performances. A Gaussian modulated pulse is used to test the performance in the time-domain. It is found that the distortion of the received signals of the UWB BPFs is negligible. Thus, it can be concluded that the proposed UWB BPFs provide satisfactory performances in both the time- and frequency-domains.

In Chapter V, a novel wideband BPF with high selectivity using an inverted T-shaped resonator has been studied. The even and odd mode resonant frequencies are analyzed by the even and odd mode equivalent circuits, respectively. Based on the resonant frequencies, the design formulas of the inverted T-shaped resonator are provided. The resonator is excited by parallel coupled feed lines with short stubs, and it is compared to the resonator fed by parallel coupled feed lines without short stubs. The feed lines with short subs additionally produce the transmission zeros not only within the stopband, improving stopband characteristics, but also near both sides of the passband, causing

significantly sharp skirt characteristics at both passband edges. In addition, the short stubs increase the number of resonant frequencies within the passband, resulting in improved passband responses. The effects of the parameters of the short stubs on frequency responses of BPF are investigated to optimize the design of the short stubs. The proposed wideband BPF provides a fractional bandwidth (FBW) of about 55 % with very high selectivity, passband symmetry, and wide stopband characteristic.

REFERENCES

[1] L. Yang and G. B. Giannakis, "Ultra-wideband communications: an idea whose time has come," *IEEE Signal Processing Magazine*, vol. 21, no. 6, pp. 26-54, Nov. 2004.

[2] C. Nguyen and M. Miao, *Design of CMOS RFIC Ultra-Wideband Impulse Transmitters and Receivers*. Cham, Switzerland: Springer, 2017.

[3] M. Makimoto and S. Yamashita, "Bandpass filters using parallel coupled stripline stepped impedance resonators," *IEEE Transactions on Microwave Theory and Techniques*, vol. 28, no. 12, pp. 1413–1417, Dec. 1980.

[4] C. H. Kim and K. Chang, "Wideband ring resonator bandpass filter with dual stepped impedance stubs," *IEEE MTT-S International Microwave Symposium Digest*, 2010, pp. 229–232.

[5] L. Zhu, S. Sun, and W. Menzel, "Ultra-wideband (UWB) bandpass filters using multiple-mode resonator," *IEEE Microwave and Wireless Components Letters*, vol. 15, no. 11, pp. 796–798, Nov. 2005.

[6] Y.-C. Chiou, J.-T. Kuo, and E. Cheng, "Broadband quasi-chebyshev bandpass filters with multimode stepped impedance resonators (SIRs)," *IEEE Transactions on Microwave Theory and Techniques*, vol. 54, no. 8, pp. 3352–3358, Aug. 2006.

[7] J. T. Kuo and C.-Y. Tsai, "Periodic stepped impedance ring resonator (PSIRR) bandpass filter with a miniaturized area and desirable upper stopband

characteristics," *IEEE Transactions on Microwave Theory and Techniques*, vol. 54, no. 3, pp. 1107–1112, Mar. 2006.

[8] I. J. Bahl, "Capacitively compensated high performance parallel coupled microstrip filters," *IEEE MTT-S International Microwave Symposium Digest,* 1989, pp. 679–682.

[9] J.-T. Kuo, W.-H. Hsu, and W.-T. Huang, "Parallel coupled microstrip filters with suppression of harmonic response," *IEEE Microwave and Wireless Components Letters*, vol. 12, no. 10, pp. 383–385, Oct. 2002.

[10] C.-W. Tang and Y.-K. Hsu, "A microstrip bandpass filter with ultrawide stopband," *IEEE Transactions on Microwave Theory and Techniques*, vol. 56, no. 6, pp. 1468–1472, Jun. 2008.

[11] S. Luo, L. Zhu, and S. Sun, "Stopband-expanded low-pass filters using microstrip coupled-line hairpin units," *IEEE Microwave and Wireless Components Letters*, vol. 18, no. 8, pp. 506-508, Aug. 2008.

[12] A. Torabi and K. Forooraghi, "Miniature harmonic-suppressed microstrip bandpass filter using a triple-mode stub-loaded resonator and spur lines," *IEEE Microwave and Wireless Components Letters*, vol. 21, no. 5, pp. 255-257, May 2011.

[13] J.-T. Kuo, T.-H. Yeh, and C.-C. Yeh, "Design of microstrip bandpass filters with a dual-passband response," *IEEE Transactions on Microwave Theory and Techniques*, vol. 53, no. 4, pp. 1331–1337, Apr. 2005.

[14] C. H. Kim and K. Chang, "Independently controllable dual-band bandpass filters using asymmetric stepped impedance resonators," *IEEE Transactions on Microwave Theory and Techniques*, vol. 59, no. 12, pp. 3037-3047, Dec. 2011.

[15] S. Luo, L. Zhu, and S. Sun, "A dual-band ring-resonator bandpass filter based on two pairs of degenerate modes," *IEEE Transactions on Microwave Theory and Techniques*, vol. 58, no. 12, pp. 3427–3432, Dec. 2010.

[16] M. H. Weng, H. W. Wu, and Y. K. Su, "Compact and low loss dual-band bandpass filter using pseudo-interdigital stepped impedance resonators for WLANs," *IEEE Microwave and Wireless Components Letters*, vol. 17, no. 3, pp. 187-189, Mar. 2007.

[17] J. X. Chen, T. Y. Yum, J. L. Li, and Q. Xue, "Dual-mode dual-band bandpass filter using stacked-loop structure," *IEEE Microwave and Wireless Components Letters*, vol. 16, no. 9, pp. 502-504, Sep. 2006.

[18] Y. H. Chun and J. S. Hong, "Electronically reconfigurable dual-mode microstrip open-loop resonator filter," *IEEE Microwave and Wireless Components Letters*, vol. 18, no. 7, pp. 449-451, July 2008.

[19] C. Lugo, G. Wang, J. Papapolymerou, Z. Zhao, X. Wang, and A. T. Hunt, "Frequency and bandwidth agile millimeter-wave filter using ferroelectric capacitors and MEMS cantilevers," *IEEE Transactions on Microwave Theory and Techniques*, vol. 55, no. 2, pp. 376-382, Feb. 2007.

[20] C. H. Kim and K. Chang, "Ring resonator bandpass filter with switchable bandwidth using stepped impedance stubs," *IEEE Transactions on Microwave Theory and Techniques*, vol. 58, no. 12, pp. 3936-3944, Dec. 2010.

[21] T.-Y. Yun and K. Chang, "Piezoelectric-transducer-controlled tunable microwave circuits," *IEEE Transactions on Microwave Theory and Techniques*, vol. 50, no. 5, pp. 1303–1310, May 2002.

[22] S.-F. Chao, C.-H. Wu, Z.-M. Tsai, H. Wang, and C. H. Chen, "Electronically switchable bandpass filters using loaded stepped impedance resonators," *IEEE Transactions on Microwave Theory and Techniques*, vol. 54, no. 12, pp. 4193–4201, Dec. 2006.

[23] C. Palego, A. Pothier, A. Crunteanu, M. Chatras, P. Blondy, C. Champeaux, P. Tristant, and A. Catherinot, "A two-port lumped-element programmable filter with MEMS pseudo-digital capacitor banks," *IEEE Transactions on Microwave Theory and Techniques*, vol. 56, no. 3, pp. 729–735, Mar. 2008.

[24] G. L. Matthaei, L. Young, and E. M. T. Jones, *Microwave Filters, Impedance-Matching Networks, and Coupling Structures*. Dedham, MA: Artech House, 1980

[25] Federal Communications Commission, "Revision of part 15 of the commission's rules regarding ultra-wideband transmission systems," FCC, Washington, DC, Tech. Rep. ET-Docket 98-153, FCC02-48, Apr. 2002.

[26] L. Zhu, S. Sun, and W. Menzel, "Ultra-wideband (UWB) bandpass filters using multiple-mode resonator," *IEEE Microwave and Wireless Components Letters*, vol. 15, no. 11, pp. 796-798, Nov. 2005.

[27] H. Wang, Q. X. Chu, and J. Q. Gong, "A compact wideband microstrip filter using folded multiple-mode resonator," *IEEE Microwave and Wireless Components Letters*, vol. 19, no. 5, pp. 287-289, May 2009.

[28] R. Li and L. Zhu, "Compact UWB bandpass filter using stub-loaded multiple mode resonator," *IEEE Microwave and Wireless Components Letters*, vol. 17, no. 1, pp. 40–42, Jan. 2007.

[29] Z.-C. Hao and J.-S. Hong, "Compact wide stopband ultra-wideband bandpass filter using multilayer liquid crystal polymer technology," *IEEE Microwave and Wireless Components Letters*, vol. 19, no. 5, pp. 290–292, May 2009.

[30] A. M. Abbosh, "Planar bandpass filters for ultra-wideband applications," *IEEE Transactions on Microwave Theory and Techniques*, vol. 55, no. 10, pp. 2262-2269, Oct. 2007.

[31] H. Shaman and J.-S. Hong, "Ultra-wideband (UWB) bandpass filter with embedded band notch structures," *IEEE Microwave and Wireless Components Letters*, vol. 17, no. 3, pp. 193–195, Mar. 2007.

[32] S. W. Wong and L. Zhu, "Implementation of compact UWB bandpass filter with a notch-band," *IEEE Microwave and Wireless Components Letters*, vol. 18, no. 1, pp. 10–12, Jan. 2008.

[33] C. H. Kim and K. Chang, "Ultra-wideband (UWB) ring resonator bandpass filter with a notched band," *IEEE Microwave and Wireless Components Letters*, vol. 21, no. 4, pp. 206-208, April 2011.

[34] C. Su and T. Jiang, "Novel ultra-wideband (UWB) bandpass filter with a notched band using defected ground structure," *Proceedings of 2014 3rd Asia-Pacific Conference on Antennas and Propagation*, Harbin, 2014, pp. 1194-1197.

[35] Q. Ye, "Transient signal analysis of butterfly-shaped monopole UWB antenna," *International Workshop on Antenna Technology*, Lisbon, 2010, pp. 1-4.

[36] N. W. Chen and K. Z. Fang, "An ultra-broadband coplanar-waveguide bandpass filter with sharp skirt selectivity," *IEEE Microwave and Wireless Components Letters*, vol. 17, no. 2, pp. 124-126, Feb. 2007.

[37] Ching-Luh Hsu, Fu-Chieh Hsu, and J. K. Kuo, "Microstrip bandpass filters for ultra-wideband (UWB) wireless communications," *IEEE MTT-S International Microwave Symposium Digest*, 2005, pp. 679-682.

[38] L. Lin, S. Yang, S. J. Sun, B. Wu, and C. H. Liang, "Ultra-wideband bandpass filter using multi-stub-loaded ring resonator," *Electronics Letters*, vol. 50, no. 17, pp. 1218-1220, Aug. 2014.

[39] S. Lan, L. Jin, and L. Zhou, "A novel UWB bandpass filter with selectivity improved by modified resonant-type composite right/left-handed structure," *International Workshop on Microwave and Millimeter Wave Circuits and System Technology*, Chengdu, 2013, pp. 292-295.

[40] W. J. Feng, W. Q. Che, and T. F. Eibert, "Ultra-wideband bandpass filter based on transversal signal-interaction concepts," *Electronics Letters*, vol. 47, no. 24, pp. 1330-1331, Nov. 2011.

[41] W. Feng and W. Che, "Novel ultra-wideband bandpass filter using shorted coupled lines and transversal transmission line," *IEEE Microwave and Wireless Components Letters*, vol. 20, no. 10, pp. 548-550, Oct. 2010.

[42] Z.-C. Hao, J.-S. Hong, J. P. Parry, and D. P. Hand, "Ultra-wideband bandpass filter with multiple notch bands using nonuniform periodical slotted ground structure," *IEEE Transactions on Microwave Theory and Techniques*, vol. 57, no. 12, pp. 3080–3088, Dec. 2009.

[43] G.-M. Yang, R. Jin, C. Vittoria, V. G. Harris, and N. X. Sun, "Small ultra-wideband (UWB) bandpass filter with notched band," *IEEE Microwave and Wireless Components Letters*, vol. 18, no. 3, pp. 176–178, Mar. 2008.

[44] K. Li, D. Kurita and T. Matsui, "UWB bandpass filters with multi notched bands," *European Microwave Conference*, Manchester, 2006, pp. 591-594.

[45] J. Xu, W. Wu, W. Kang, and C. Miao, "Compact UWB bandpass filter with a notched band using radial stub loaded resonator," *IEEE Microwave and Wireless Components Letters*, vol. 22, no. 7, pp. 351-353, July 2012.

[46] M.-G. Di Benedetto and L. De Nardis, "Tuning UWB signals by pulse shaping: Towards context-aware wireless networks," *Signal Processing*, vol. 86, no. 9, pp. 2172-2184, Sep. 2006.

[47] K. S. Chin, L. Y. Lin, and J. T. Kuo, "New formulas for synthesizing microstrip bandpass filters with relatively wide bandwidths," *IEEE Microwave and Wireless Components Letters*, vol. 14, no. 5, pp. 231–233, May 2004.

[48] C. C. Chen, J. T. Kuo, M. Jiang, and A. Chin, "Study of parallel coupled-line microstrip filter in broadband," *Microwave and Optical Technology Letters*, vol. 48, no. 2, pp. 373–375, Feb. 2006.

[49] C. Y. Hung, M. H. Weng, R. Y. Yang, and Y. K. Su, "Design of the compact parallel coupled wideband bandpass filter with very high selectivity and wide stopband," *IEEE Microwave and Wireless Components Letters*, vol. 17, no. 7, pp. 510-512, July 2007.

[50] J. An, G.-M. Wang, W.-D. Zeng, and L.-X. Ma, "UWB filter using defected ground structure of Von Koch fractal shape slot," *Progress In Electromagnetics Research Letters*, vol. 6, pp. 61–66, 2009.

[51] S. Sun and L. Zhu, "Wideband microstrip ring resonator bandpass filters under multiple resonances," *IEEE Transactions on Microwave Theory and Techniques*, vol. 55, no. 10, pp. 2176–2182, Oct. 2007.

[52] L.-H. Hsieh and K. Chang, "Compact, low insertion-loss, sharp-rejection, and wide-band microstrip bandpass filters," *IEEE Transactions on Microwave Theory and Techniques*, vol. 51, no. 4, pp. 1241-1246, Apr 2003.

[53] S. Y. Shi, W. J. Feng, W. Q. Che, and Q. Xue, "Novel miniaturization method for wideband filter design with enhanced upper stopband," *IEEE Transactions on Microwave Theory and Techniques*, vol. 61, no. 2, pp. 817-826, Feb. 2013.

[54] W. Feng, W. Che, T. F. Eibert, and Q. Xue, "Compact differential ultra-wideband bandpass filter based on transversal filter concepts," *European Microwave Conference*, Manchester, 2011, pp. 456-459.

[55] W. J. Feng, W. Q. Che, Y. M. Chang, S. Y. Shi, and Q. Xue, "High selectivity fifth-order wideband bandpass filters with multiple transmission zeros based on transversal signal-interaction concepts," *IEEE Transactions on Microwave Theory and Techniques*, vol. 61, no. 1, pp. 89-97, Jan. 2013.

[56] S. Xue, W. Feng, H. Zhu, and W. Che, "Microstrip wideband bandpass filter with six transmission zeros using transversal signal-interaction concepts," *Progress In Electromagnetics Research C*, vol. 34, pp. 1-12, 2013.